# THE DYNAMICS OF MEAN CIRCULATION ON THE CONTINENTAL SHELF

by

PING-TUNG PETER SHAW

B.S., National Taiwan University (1972)

M.S., University of Rhode Island (1977)

SUBMITTED IN PARTIAL FULFILLMENT OF THE
REQUIREMENTS FOR THE DEGREE OF

DOCTOR OF PHILOSOPHY

at the

MASSACHUSETTS INSTITUTE OF TECHNOLOGY

and the

WOODS HOLE OCEANOGRAPHIC INSTITUTION

February, 1982

Signature of Author _____
Joint Program in Oceanography, Massachusetts Institute of Technology-Woods Hole Oceanographic Institution, and Department of Meteorology and Physical Oceanography, Massachusetts Institute of Technology, November 6, 1981.

Certified by _____
Thesis Supervisor

Accepted by _____
Chairman, Joint Oceanography Committee in Earth Sciences, Massachusetts Institute of Technology - Woods Hole Oceanographic Institution.

WITHDRAWN
FROM
MIT LIBRARIES
MASSACHUSETTS INSTITUTE OF TECHNOLOGY
MAR 22 1982
LIBRARIES

# THE DYNAMICS OF MEAN CIRCULATION ON THE CONTINENTAL SHELF

by

PING-TUNG PETER SHAW

Submitted to the Massachusetts Institute of Technology - Woods Hole Oceanographic Institution Joint Program in Oceanography on November 6, 1981, in partial fulfillment of the requirements for the degree of Doctor of Philosophy

## ABSTRACT

Mean long-isobath drift of the order 5 cm/sec has been observed on several continental shelves, e.g. in the Middle Atlantic Bight and in the Weddell Sea. A theoretical model is developed to explore the driving mechanism of this mean circulation. In the model, the velocity field is decomposed into a depth-independent bottom geostrophic component and a thermohaline component relative to the bottom. The latter can be calculated from the density field, and the former is described by a parabolic equation which expresses the tendency to balance vorticity between bottom stress curl and vortex stretching. The near-bottom flow field is studied both analytically and numerically under forcing by wind, deep ocean flow, and long-isobath density differences.

Model solutions are derived for circulations over a shelf/slope topography driven by wind stress, wind stress curl, and deep ocean currents. The resulting flow patterns show strong dependence on the topography. Over the continental slope, large bottom depth variation suppresses the flow driven by local forcing and insulates the slope region from circulations on the shelf and in the deep-ocean. Geochemical observations on the continental shelf and slope support the argument that the flow on the upper slope below the thermocline is weak.

Under the condition of a vertically homogeneous layer below the thermocline, near-bottom density advection is mainly caused by the bottom geostrophic velocity field. Using the parabolic vorticity equation together with a density equation, circulations driven by coastal buoyancy flux and surface cooling are investigated. In the mid-shelf region, away from the coast and the shelf break, the density field is governed by Burgers' equation, which shows longshore self-advection of density perturbations and the formation of front with strong density gradient in the longshore direction. A dense water blob moves in the direction of Kelvin wave propagation. The direction is reversed for the movement of a light water blob. In the near-shore region, the light river water at the bottom is also self-advected in the direction of Kelvin wave

propagation. For a heavy density anomaly at the coast, the initial movement is offshore, and the accumulation of dense water in the mid-shelf region leads to long-isobath propagation of density perturbations, similar to the case of a dense water blob. This theory sheds light on the bottom water movements in the Adriatic Sea, the Antarctic Continent, and the Middle Atlantic Bight.

The model solutions are applied to the flow on the western North Atlantic shelf. Southwestward flow is produced near the coast by the self-advection of river water in winter and spring. The southwestward long-isobath propagation of thermal fronts caused by winter cooling contributes significantly to the mean circulation over the mid-shelf. It is suggested that density-driven current is an important component of the near-bottom mean circulation in the Middle Atlantic Bight in spring and summer.

Thesis Supervisor: Dr. Gabriel T. Csanady

Title: Senior Scientist
Woods Hole Oceanographic Institution

## ACKNOWLEDGEMENTS

The most sincere gratitude goes to my thesis advisor Dr. Gabriel T. Csanady for his guidance, support, and encouragement during my years in Woods Hole Oceanographic Institution. Also, I have to express my deepest appreciation of his enormous patience in reading and correcting the many drafts of my thesis. His illuminating comments on the presentation of this work greatly improved its readability.

I thank the members of my thesis committee, Professor Glenn Flierl of M.I.T., Drs. Robert Beardsley and Joseph Pedlosky of W.H.O.I., for their advices, reading the thesis, and providing helpful comments. I am also grateful to Dr. Dale Haidvogel for the enlightenment of numerical techniques used in this work.

I thank Mrs. Mabel Reese for her warm assistance in many aspects.

I owe a special debt of gratitude to my wife Ching-ju Chen for her sacrifice in helping me during my years as a graduate student, especially the period of thesis writing.

This work was supported by the Department of Energy through contract entitled Coastal-Shelf Transport and Diffusion.

TABLE OF CONTENTS

Abstract..... 2

Acknowledgements..... 4

Table of contents..... 5

List of figures..... 8

List of tables..... 12

Chapter 1 Introduction

1.1 A prototype shelf: the Middle Atlantic Bight..... 14

1.2 Driving mechanism: earlier theories..... 16

1.3 Models of nonuniform longshore flow over topography... 20

1.4 Summary..... 25

Chapter 2 Dynamic Equations

2.1 The momentum equations..... 28

2.2 Decomposition of velocity field..... 34

2.3 Discussion..... 40

2.4 The density equation..... 42

Chapter 3 The Effect of Steep Slope on the Bottom Pressure Field

3.1 Formulation of the problem..... 49

3.2 Local wind forcing..... 51

3.2.1 Longshore wind stress forcing..... 52

3.2.2 Wind stress curl forcing..... 54

3.3 Numerical solutions..... 60
3.3.1 Longshore wind stress forcing..... 61
3.3.2 Wind stress curl forcing..... 64
3.4 The insulating effect of a steep slope on a western boundary current..... 65
3.4.1 Introduction..... 65
3.4.2 Model of slope/deep-ocean interaction..... 70
3.4.3 Flow driven by a longshore thermohaline current over the slope..... 74
3.4.4 Forcing from deep ocean currents..... 75
3.5 Application of the slope model..... 77
3.6 Summary..... 79

Chapter 4 Density-Driven Flow and the Dispersion of Density Perturbations
4.1 Introduction..... 100
4.2 Formulation of the problem..... 103
4.2.1 The velocity field..... 103
4.2.2 Case of vertically homogeneous water column..... 105
4.3 Dispersion of an initial density perturbation along isobaths..... 109
4.4 Numerical solutions..... 118
4.4.1 The density and velocity scales..... 118
4.4.2 Coastal density flux forcing..... 120
4.4.3 Flow forced by surface density flux..... 127

4.4.4 Discussion..... 130

4.5 Evidence of bottom water movement on continental shelves..... 132

4.5.1 Winter circulation in the Adriatic Sea..... 132

4.5.2 Bottom water movement in the Antarctic Continent..... 134

4.5.3 Cold water pool in the Middle Atlantic Bight..... 135

4.6 Summary..... 139

Chapter 5 Mean circulation on the Western North Atlantic Shelf

5.1 Wind-driven mean circulation..... 208

5.2 Dispersion of river water..... 212

5.3 The movement of winter water in the Middle Atlantic Bight..... 214

5.4 Conclusion..... 220

References..... 221

Biographical note..... 226

LIST OF FIGURES

Chapter 2 .....pages 47-48

Figure 2.1 Schematic diagram showing the coordinate system.

Chapter 3 .....pages 80-99

Figure 3.1 Bottom profile used in numerical computations. The distance and the depth are scaled by 100 km and 100 m respectively. The shelf shown is a "wide" shelf.

Figure 3.2 Distribution of bottom pressure $\phi$ over a "wide" shelf, forced by a positive longshore stress from y = -2.5 to y = 0 (Case I). The nondimensional contour interval is 0.1.

Figure 3.3 Distribution of bottom pressure $\phi$ forced by a positive longshore stress from y = -2.5 to y = 0 with a coastal wall placed at x = 0.75 (Case II). The nondimensional contour interval is 0.1.

Figure 3.4 Distribution of bottom pressure $\phi$ over a "narrow" shelf, forced by a positive longshore stress from y = -2.5 to y = 0 (Case III). The nondimensional contour interval is 0.1.

Figure 3.5 Distribution of bottom pressure $\phi$ forced by a positive wind stress curl from y = -2.5 to y = 0, which is uniform in x (Case IV). The nondimensional contour interval is 0.1.

Figure 3.6 x-component bottom geostrophic velocity distribution calculated from the bottom pressure field in Figure 3.5. Dashed lines represent negative values.

Figure 3.7 y-component bottom geostrophic velocity distribution calculated from the bottom pressure field in Figure 3.5. Dashed lines represent negative values.

Figure 3.8 Transport of longshore bottom velocity shown in Figure 3.7.

Figure 3.9 Bottom pressure field produced by deep ocean forcing with $\varepsilon = 0.05$ and $\beta = 0.01$.

Figure 3.10 Long-isobath bottom velocity calculated from the pressure field in Figure 3.9.

Chapter 4 .....pages 141 - 206

Figure 4.1 Schematic diagram demonstrating the solution of Burgers' equation. The density distribution at t = 0 is a delta function located at y = 0.

Figure 4.2 Schematic diagram showing solutions of Burgers' equation at different values of time with an initial (t = 0) delta function disturbance located at y = 0. A positive disturbance is shown by solid lines, and a negative one by dashed lines.

Figure 4.3a Distributions of density (left) and bottom velocity (right) at t = 1 produced by buoyancy flux located at $-1 < y < 0$. The parameters are $R_0/\gamma = 2.5$ and $\gamma = 0.025$. The density field is contoured with an interval of 0.25.

Figure 4.3b Distributions of density (left) and bottom velocity (right) at t = 5 produced by buoyancy flux located at $-1 < y < 0$. The parameters are $R_0/\gamma = 2.5$ and $\gamma = 0.025$. The density field is contoured with an interval of 0.25.

Figure 4.3c Distributions of density (left) and bottom velocity (right) at t = 10 produced by buoyancy flux located at $-1 < y < 0$. The parameters are $R_0/\gamma = 2.5$ and $\gamma = 0.025$. The density field is contoured with an interval of 0.25.

Figure 4.4 Evolution of the density distribution at y = -1 as a function of time.

Figure 4.5 Longshore density distribution along the x = 0.3 isobath at different values of time.

Figure 4.6 Longshore density distribution along the x = 0.3 isobath at t = 10 for different values of $\gamma$

Figure 4.7 Longshore density distribution along the x = 0.3 isobath at t = 10 for different values of $R_0/\gamma$ with $\gamma = 0.025$. The density is scaled by $R_0/\gamma$.

Figure 4.8a Distributions of density (left) and bottom velocity (right) at t = 1 with forcing from a coastal density source locasted at $-1 < y < 0$.

Figure 4.8b Distributions of density (left) and bottom velocity (right) at t = 5 with forcing from a coastal density source located at $-1 < y < 0$.

Figure 4.8c Distributions of density (left) and bottom velocity (right) at t = 10 with forcing from a coastal density source located at $-1 < y < 0$.

Figure 4.8d Distributions of density (left) and bottom velocity (right) at t = 15 with forcing from a coastal density source located at $-1 < y < 0$.

Figure 4.9 Contour plot of longshore density distribution along the x = 2.5 isobath on the y-t plane. The forcing is a coastal density source at $-1.0 < y < 0$. Dashed line shows the location of density maximum along the isobath.

Figure 4.10a Contour plot of density field at t = 1 produced by surface cooling. The forcing is applied at $-1.0 < y < 0$ from t = 0 to t = 2.

Figure 4.10b Contour plot of density field at t = 2 produced by surface cooling. The forcing is applied at $-1.0 < y < 0$ from t = 0 to t = 2.

Figure 4.10c Contour plot of density field at t = 5 produced by surface cooling. The forcing is applied at $-1.0 < y < 0$ from t = 0 to t = 2.

Figure 4.11a Magnitude of the longshore bottom velocity at t = 1, corresponding to the density field in Figure 4.10a.

Figure 4.11b Magnitude of the longshore bottom velocity at t = 2, corresponding to the density field in Figure 4.10b.

Figure 4.11c Magnitude of the longshore bottom velocity at t = 5, corresponding to the density field in Figure 4.10c.

Figure 4.12a Magnitude of the offshore bottom velocity at t = 1, corresponding to the density field in Figure 4.10a.

Figure 4.12b Magnitude of the offshore bottom velocity at t = 2, corresponding to the density field in Figure 4.10b.

Figure 4.12c Magnitude of the offshore bottom velocity at t = 5, corresponding to the density field in Figure 4.10c.

Figure 4.13 Distribution of density along the x = 1.0 isobath for cooling with parameters T = 2, $L_y = 1$, and $\gamma = 0.05$.

Figure 4.14 Contour plot of longshore density distribution along the x = 1.0 isobath on the y-t plane. Surface cooling is applied between y = -1 and 0 from t = 0 to 2. The parameter $\gamma$ is 0.1. Dashed line shows the location of temperature minimum along this isobath.

Figure 4.15 Longhsore density distribution along the x = 1.0 isobath for cooling with parameters T = 2, $L_y = 1$, and $\gamma = 0.1$.

Figure 4.16 Longhsore density distribution along the x = 1.0 isobath for cooling with parameters T = 3, $L_y$ = 1, and $\gamma$ = 0.05.

Figure 4.17 Longhsore density distribution along the x = 1.0 isobath for cooling with parameters T = 2, $L_y$ = 2, and $\gamma$ = 0.05.

Figure 4.18a Distribution of bottom temperature in the Middle Atlantic Bight in February 1929 (from Bigelow, 1933).

Figure 4.18b Distribution of bottom temperature in the Middle Atlantic Bight in April 1929 (from Bigelow, 1933).

Figure 4.18c Distribution of bottom temperature in the Middle Atlantic Bight in July 1929 (from Bigelow, 1933).

Figure 4.19 Evolution of bottom temperature between the coast and the shelf break along 71°W, from Chamberlin (1978) and Crist and Chamberlin (1979).

Figure 4.20 Distribution of bottom temperature on Georges Bank in May 1979. Data from EG & G (1979).

# LIST OF TABLES


| | | Page |
|---|---|---|
| Table 2.1 | Scaling parameters and nondimensional numbers independent of forcing. | 32 |
| Table 3.1 | Scales and nondimensional parameters in the wind-driven case. | 53 |
| Table 3.2 | Summary of numerical solutions under longshore wind stress forcing. | 62 |
| Table 3.3 | Summary of numerical solutions under wind stress curl forcing. | 66 |
| Table 4.1 | Scales and nondimensional parameters for flow driven by coastal buoyancy flux. | 122 |
| Table 4.2 | Scales and nondimensional parameters for flow driven by surface density flux. | 123 |

# CHAPTER 1

# INTRODUCTION

Circulation over the continental shelf is dominated by high frequency oscillations produced by tides and winds with periods shorter than the synoptic time scale of a few days. However, when currents are averaged over a month or a longer period, a consistent mean drift along isobaths is sometimes detected in the near-bottom circulation above the bottom Ekman layer. In the Middle Atlantic Bight, a subsurface mean flow of the order 5 cm/sec has been observed by moored instrument measurements (Beardsley et al., 1976). Over the Weddell Sea shelf in the Antarctic Continent, the long-isobath drift is shown by a westward movement of the dense bottom water (Gill, 1973). In a semi-enclosed basin like the northern Adriatic Sea in winter, the long-isobath density dispersion is associated with a cyclonic circulation gyre (Hendershott and Rizzoli, 1976).

Throughout this work, the term "mean circulation" is meant to describe the pattern of currents averaged over a chosen period. By this definition, the "mean" flow does not have to be steady. It can be non-periodic transient flow with a time scale longer than the period of averaging. Mean circulation is important in the dispersion of water properties, nutrients, and pollutants on the shelf. Without the mean flow, the distribution of materials is determined by the short-period chaotic first order flow, which acts as an effective eddy diffusion process in both horizontal directions. However, advection by even a

moderately intense mean flow is generally more effective than eddy diffusion in dispersing materials in the downstream direction. In particular, the near-bottom mean flow is important to the distribution of pollutants near a dump site and the movement of cold bottom water from the north, two phenomena which play key roles in benthic ecology and fisheries.

The objective of this study is to understand the driving mechanisms of mean circulation on the continental shelf. Bottom flow may be generated in the ocean by wind and by the interaction between topography and near-bottom density variations (Holland, 1973). Typically, the time scale of wind is shorter than a month, and that of density forcing is about a season. Therefore, it is possible to examine the wind-driven shelf circulation diagnostically with an assumed density structure. Under density forcing, the density field itself is dynamically important. The bottom velocity field must be found prognostically. In this work, a genaral prognostic model of shelf circulation with time scale longer than a month is developed. This model is solved diagnostically under forcing by wind over the shelf, the slope, and the deep ocean regions. Analytical and numerical solutions of the prognostic model are derived to understand the dynamics of density-driven flow. These results on the flow forced by wind and density fields are then compared with observed mean flow on the continental shelf to identify the driving mechanisms.

## 1.1 A Prototype Shelf: the Middle Atlantic Bight

Compared to other shelves, the Middle Atlantic Bight is a relatively

well explored region. An examination of the density structure and the mean bottom flow in this region can provide insights into the dynamics of shelf circulation in general. The hydrography over the continental shelf in the Middle Atlantic Bight is characterized by seasonal variations. In winter, the water column is vertically homogeneous with small horizontal density differences over most of the shelf. A density front exists near the shelf break with strong temperature and salinity gradients. Minimum bottom temperature occurs in late March each year. The salinity reaches a maximum during late January to early February, and remains relatively constant until the river runoff reduces the near-shore salinity in spring. In summer, a thermocline is present at the depth of 15 - 20 m, and the bottom temperature is cold offshore beyond a line about 30 km from the coast. The cold water below the thermocline is known as the "cold pool" (Bigelow, 1933).

Comprehensive reviews of the circulation in the Middle Atlantic Bight can be found in articles by Bumpus (1973), Beardsley et al. (1976), and Beardsley and Boicourt (1981). Characteristics of the subsurface mean flow in the Middle Atlantic Bight, averaged over a month or longer from long-term current measurements, are summarized as follows:

(1) The longshore current has a southwestward component thoughout the water column (Beardsley and Boicourt, 1981). The longshore mean velocity is from 3 to 10 cm/sec. It increases noticeably with increasing distance from the shore and decreases with increasing depth in the water column (Beardsley et al., 1976).

(2) The cross-isobath bottom flow shows a divergence at about the

60 m isobath. The flow is onshore in shallow water and offshore in deep water (Bumpus, 1973).

(3) During infrequent periods of strong and persistent wind, a component driven by wind is detectable in the monthly-mean current over most of the Middle Atlantic Bight (Beardsley and Boicourt, 1981).

(4) In summer, the velocity of longshore current in the cold water pool equals or exceeds the mean southwestward movement of the surrounding warmer water (Beardsley et al., 1976).

It is clear that the wind-driven flow dominates the mean circulation under strong wind conditions. In less severe weather, the wind-driven flow may still contribute to part of the mean flow. Because of the existence of a line of divergence and the flow is stronger at the shelf break than in the near-shore region, the principal driving forces are probably located on the outer shelf or on the slope. Furthermore, the flow inside the cold pool is stronger than the surrounding flow. Dynamically the cold pool may be more important than a simple translative motion associated with a mean flow. This is an indication that the density-driven flow plays an important role in the mean circulation.

1.2 Driving Mechanism: Earlier Theories

Suggested possible driving mechanisms of the mean circulation include: (i) wind forcing, (ii) forcing from the influx of river water, (iii) forcing from the density variations caused by surface cooling, and (iv) deep ocean forcing, represented by a sea level gradient on the shelf. Earlier theoretical models of near-shore circulation were generally two-dimensional, assuming uniformity in the longshore

direction, including uniformity of pressure, i.e. absence of a longshore pressure gradient. Basically, these two-dimensional models originated from that of Ekman (1905). A principal assumption was that the total cross-shelf transport vanished in the coastal region. A longshore interior flow had to exist in the downwind direction, generating bottom stress large enough to balance the offshore wind-driven surface Ekman transport through an onshore bottom Ekman transport (Jeffreys, 1923). However, the observed line of divergence over the outer shelf revealed that the simple Ekman model could not be used to explain the mean shelf circulation, at least over the outer shelf.

Iselin (1955) suggested that the mean surface drift in the Middle Atlantic Bight could be thermohaline flow associated with the offshore density gradient by the thermal wind relation. However, it is not clear how that relationship should be applied in shallow water of variable depth. Another idea was that the flow was driven by a deep-ocean imposed sea level elevation along the coast. Sverdrup et al. (1942) inferred the existence of a massive cyclonic gyre between the Gulf Stream and the east coast of North America from the longshore rise of sea level between Cape Hatteras and Nova Scotia, indicated by geodetic leveling. This cyclonic gyre appeared as a southwestward drift in the Middle Atlantic Bight region. However, this idea was in doubt, after the geodetic result was disputed by Sturges (1968) and Montgomery (1969).

The paper by Stommel and Leetmaa (1972) was the first attempt to construct a quantitative model for the winter mean shelf circulation in the Middle Atlantic Bight. With the assumption that the cross-shelf

transport vanished everywhere, the steady circulation under forcing by longshore uniform wind stress and freshwater influx was solved over a flat bottom shelf without coastal and seaward boundaries. It was concluded that the flow driven by longshore wind stress would be opposite to the observed mean drift. The effect of river efflux in this constant depth model was much as described by Iselin (1955). However, the magnitude of thermohaline component was found to be too weak to reverse the wind-driven flow so that the density structure could not explain the observed southwestward drift either. The discrepancy between the predicted flow and the observed one lead Stommel and Leetmaa (1972) to postulate the existence of a longshore pressure gradient of unspecified physical origin. With a properly chosen longshore pressure gradient, the observed flow could be simulated and the effects of bottom friction assessed realistically.

Circulation over a sloping bottom was treated by Csanady (1976), using a basically similar approach with some modifications. In this model, the mean circulation was taken to be the residue of chaotic first-order flow events created by wind, tides, and river flow. It was argued that the statistical effects of variable first-order events on the mean flow could be parameterized by linear internal and bottom friction laws, and by an effective diffusivity for the salt transport determined by first order flow events. A linear problem resulted, with circulation viewed as a superposition of components caused by wind stress, freshwater inflow, and a longshore pressure gradient. The last one was of unspecified physical origin as in Stommel and Leetmaa's (1972) model.

With no other longshore nonuniformity allowed, the longshore thermohaline component was again found from the thermal wind relation, modified by friction, with vanishing bottom longshore velocity. From the vorticity tendency balance, it was shown that the assumption of vanishing cross-shore transport at all distances from the coast implied a constant longshore pressure gradient. The magnitude of this gradient was viewed as a parameter expressing the influence of the rest of the ocean on the shelf region considered, and was determined from the analysis of observational evidence (Scott and Csanady, 1976). Key features of the observations, such as the presence of a "line of divergence" in the cross-shelf flow or the offshore increase in the magnitude of the longshore velocity, were reproduced by his model.

These earlier models provided some understanding of shelf dynamics, at least in the sense of elucidating possible driving forces. They also yielded useful parameters such as the frictional coefficient, the effective vertical and horizontal eddy diffusivities. Direct wind forcing and the cross-shelf density gradient were ruled out as the proximate driving mechanisms of the mean drift. Furthermore, the unknown "remote" driving force in the Middle Atlantic Bight, parameterized as a longshore pressure gradient on the shelf, could be quantified from the observed mean drift.

Similar two-dimensional models were used by Barcilon (1966) to model the effect of river momentum flux and by Killworth (1973a) in studying the bottom water formation in the Antarctic Continent. Killworth (1973a) concluded that the offshore transport in his two-dimensional model was

too small to account for the observed rate of bottom water formation. Killworth (1974) also studied the Antarctic Bottom Water formation forced by surface density flux in a two-layer model over a flat shelf. By allowing horizontal density variation in each layer, he found that the density increase was caused mainly by upwelling at the western side of the Weddell Sea. Also, the observed east-west density gradient (Gill, 1973) could be simulated by the model. The northward flux was found to be too small to give the observed rate of bottom water formation. It also took a long time (about 30 years) for the density perturbations to span the whole basin from the western boundary. Obviously, the shelf topography and the longshore nonuniformity of the flow must play essential roles in the shelf dynamics.

1.3 Models of Nonuniform Longshore Flow over Topography

The need for a local pressure gradient to drive the mean flow is actually a manifestation of the fact that some forcing effect on the shelf, slope, or deep ocean was either not considered or not quantified properly. For further understanding of the pressure field, it is necessary to generalize the theoretical model.

Birchfield (1967) used a parabolic vorticity equation to study the wind-driven circulation in a circular homogeneous lake with a parabolic bottom profile. Solutions were obtained for the flow with finite coastal wall and with vanishing coastal depth. The results showed that the flow driven by wind stress was concentrated on the left- and the right-hand sides of the lake. Long-isobath circulation was produced by wind stress curl. A weak flow driven by the divergence of wind was found. The

coastal wall had only minor effect on the flow under wind stress forcing. However, a counter current was detected in the flow driven by wind stress curl, when the water depth shoaled to zero at the coast. The same parabolic equation emerged in Birchfield's (1972) analysis of wind-driven circulation in a homogeneous lake with arbitrary topography. This equation, which governed the near-shore circulation, represented the balance between vortex stretching and the curl of bottom stress.

Pedlosky (1974) studied the steady circulation over shelf-like topography, which was limited by finite-depth boundary walls at coastal and oceanic boundaries. A parabolic vorticity equation similar to that of Birchfield (1972) was derived for a stratified fluid, governing the flow in a coastal topographic boundary layer. Besides wind forcing, the flow driven by surface heat flux was studied through the use of a linearized, steady density equation, in which the advection of the basic vertical density stratification was balanced by horizontal diffusion. It was shown that, because of the coastal constraint, a poleward undercurrent in the upwelling region of the Oregon shelf could be generated within the topographic boundary layer by wind stress, its curl, or differences in surface heating.

Beardsley and Hart (1978) used a similar parabolic formulation in their linear two-layer model to examine the river-induced steady flow over a sloping bottom. The river effect was considered to be a source in the surface layer and a sink in the bottom layer. The vorticity generated by river stream flux was dissipated through the friction at the interface and the bottom. A steady flow was found in the vicinity of the

source region with a length scale of some tens of kilometers.

In a series of papers by Csanady (1978, 1980, 1981), the parabolic formulation was used to investigate the driving forces of the mean shelf circulation in the Middle Atlantic Bight. It was found that a coastally trapped pressure field could be set up by direct wind stress forcing. The pressure field further offshore was affected by the wind stress curl. Some observations on coastal sea level elevation were presented by Csanady (1981) as evidence for the existence of such a pressure field. Csanady (1978, 1981) also studied the pressure gradient produced by river outflow, which was modelled as a steady distribution of sea surface elevation in the source region. A southwestward longshore flow on the western North Atlantic shelf could be generated by a large river source to the north, e.g. the St. Lawrence River (Csanady, 1978, 1981). The influence from the deep ocean was parameterized by Csanady (1978) as a longshore pressure gradient at the shelf break. It was found that this parameterization could reproduce most of the known features of the pressure field on the shelf.

The studies of Csanady (1978, 1980, 1981) give a fairly good description of the pressure field set up by wind stress forcing inside a coastal boundary layer about 30 km wide. An important consequence of the parabolic equation was that forcing with limited longshore extent could influence the flow only in the "forward" direction, which was defined by signs of the terms in the parabolic equation. In the outer shelf region, Csanady's solutions suggest that flow was generated by forcing in the backward portion of the shelf, such as river inflow, wind stress curl,

and/or a deep ocean imposed pressure gradient at the shelf break. However, the problem was not resolved in favor of any particular forcing. The bottom topography in his models was a shelf with constant slope of order $10^{-3}$ extending to very large distances from the coast. The continental slope, with its one to two order of magnitude greater depth variation than that of the shelf, may have a significant dynamic influence on the circulation of the outer shelf. To understand the dynamics of the outer shelf circulation, it is necessary to investigate these forcing mechanisms in detail, especially the topographic effect on the flow.

One could imagine that the existing theories of deep ocean gyres would give some guidance as to what "deep ocean influence" could be expected on a shelf. However, models of deep ocean circulation with western boundary topography do not give a clear and definite conclusion on how much of the deep ocean flow will intrude onto the shelf. Schulman and Niiler's (1970) solution in a homogeneous ocean seemed to suggest the presence of a pressure gradient on the shelf due to deep ocean circulation. However, a similar model by Killworth (1973b) did not reveal such an influence. Recent multi-layer numerical solutions of Semtner and Mintz (1977) on the circulation in the western North Atlantic Ocean showed that a pressure gradient existed on the shelf from Cape Hatteras to Grand Bank. It was argued by Beardsley and Winant (1979) that this might be taken as evidence of deep ocean influence. Csanady (1979) calculated the steric set-up of sea level on the western margin of the North Atlantic Ocean. No significant long-isobath sea level gradient

over the slope region was found. To resolve the controversy over this deep ocean forcing problem, a study of the near-bottom circulation in the slope and rise regions is necessary.

One important mechanism, which was not studied in Csanady's models, is the forcing from long-isobath density variations. Evidence of such long-isobath density variations on the shelf has been found on several occasions. In the calculation of sea level set-up along the western margin of the North Atlantic Ocean, Csanady (1979) found a sea level rise on the Scotian shelf produced by the density deficiency of the St. Lawrence River outflow. On the shelves of Antarctic Continent, the accumulation of high salinity water at the western side of the Weddell Sea (Gill, 1973) and the Rose Sea (Jacobs et al., 1970) produces strong long-isobath salinity gradient. It is important to incorporate this density effect into the parabolic formulation. Hendershott and Rizzoli (1976) have shown by numerical model calculations that unsteady long-isobath density advection is important dynamically. In order to examine this question in greater generality, it is desirable to develop analytical models of the interaction between longshore density variations and bottom topography.

According to Csanady's (1978, 1981) model, a "mound" of river water in the north is able to drive a mean southward drift in the western North Atlantic shelf. However, a quantitative relation between the sea level distribution in the "mound" and the amount of river outflow was not given. Beardsley and Hart's (1978) model provides a practical method to relate these two quantities. An application of the latter model shows

that the amount of river outflow is insufficient to drive the mean drift in the Middle Atlantic Bight.

1.4 Summary

From the dynamic consideration in the earlier sections, it may be concluded that to understand the driving mechanisms on the continental shelf, it is essential to solve the folllowing problems:

(1) What is the pressure field over a realistic shelf/slope topography under wind forcing?

(2) Does the deep ocean impose a pressure gradient on the slopes, and if so, how?

(3) What is the role of the slope in "insulating" this pressure gradient from the shelf or "transmitting" it to the shelf?

(4) What is the flow field generated by the density field, when the latter is produced by cooling, river buoyancy flux, or other density effects?

(5) How is the density field itself affected by the density-driven flow?

The principal aim of this work is to develop a prognostic model to answer these questions. The theoretical model used is fairly general and can be applied to different continental shelves. In Chapter 2, the model used by Csanady (1978) is generalized to the case with density stratification. To simplify the problem, the total velocity field is decomposed into a depth-independent bottom geostrophic component and a thermohaline component relative to the bottom. The resulting equations, governing the bottom geostrophic flow forced by long-isobath bottom

density variations and by wind, can be solved diagnostically with a known bottom density distribution. The thermohaline component can be found from the density distribution. The prognostic formulation is achieved by the use of a density equation which includes the nonlinear advection and the time-dependent terms. Under the assumption of vertical homogeneity of the water column, the density equation is expressed in terms of bottom geostrophic velocity. The time evolution of density field and flow under forcing can then be followed.

In Chapter 3, the long-isobath density gradient is neglected to isolate the wind-driven circulation. The model is solved numerically for the flow driven by wind stress and wind stress curl over various shelf topographies. The purpose of this approach is to examine the effect of bottom slope on the mean circulation pattern and to identify the contribution of wind-driven flow under strong and persistent wind conditions. The possible influence of deep ocean currents on the shelf circulation is also analyzed. The insulating effect of the slope on the deep ocean circulation gyres is examined.

To explore the contribution to the mean flow from the long-isobath density differences on the shelf and the upper slope, a model is developed in Chapter 4 for the transient, though long time-scale flow forced both by a coastal buoyancy flux and by a surface density flux. In the vertically homogeneous layer below the seasonal thermocline, it is shown that the thermohaline velocity does not contribute to the density advection and that the bottom velocity component is crucial to the advection process. The model is aimed at elucidating the generation of

bottom velocity and the dispersion of density perturbations. Model results are compared with the observed bottom water distributions over various shelves.

In Chapter 5, contributions from various forcing components are estimated, using the model results in the earlier chapters. The driving mechanism of the mean southwestward drift in the Middle Atlantic Bight is then discussed in relationship to the observational evidence .

# CHAPTER 2

# DYNAMIC EQUATIONS

In this chapter the dynamical equations are formulated, that will be used in later chapters to study the mean circulation over the continental margins. The study will be focused on forcing with periods longer than a month, by wind, deep ocean pressure gradient, river buoyancy flux, and surface cooling.

## 2.1 The Momentum Equations

Consider the motion on a β-plane along a straight and long coast in the north-south direction. The coordinate system is chosen such that the x-axis points to the east, y to the north and z upward (Figure 2.1). The bottom depth is a function of x only and varies from nearly zero at the coast to the depth of deep ocean. We will use variables without superscripts to denote nondimensional quantities. The corresponding dimensional ones are expressed by a superscript "*". The sea surface is assumed to be rigid and the density is a linear function of temperature and salinity. The equations of motion are:

$$\frac{\partial u^*}{\partial t^*} + u^*\frac{\partial u^*}{\partial x^*} + v^*\frac{\partial u^*}{\partial y^*} + w^*\frac{\partial u^*}{\partial z^*} - f^*v^* = -\frac{1}{\rho_o}\frac{\partial p^*}{\partial x^*} + A_H\left(\frac{\partial^2 u^*}{\partial x^{*2}} + \frac{\partial^2 u^*}{\partial y^{*2}}\right) + A_v\frac{\partial^2 u^*}{\partial z^{*2}} \tag{2.1a}$$

$$\frac{\partial v^*}{\partial t^*} + u^*\frac{\partial v^*}{\partial x^*} + v^*\frac{\partial v^*}{\partial y^*} + w^*\frac{\partial v^*}{\partial z^*} + f^*u^* = -\frac{1}{\rho_o}\frac{\partial p^*}{\partial y^*} + A_H\left(\frac{\partial^2 v^*}{\partial x^{*2}} + \frac{\partial^2 v^*}{\partial y^{*2}}\right) + A_v\frac{\partial^2 v^*}{\partial z^{*2}} \tag{2.1b}$$

$$\frac{\partial w^*}{\partial t^*} + u^*\frac{\partial w^*}{\partial x^*} + v^*\frac{\partial w^*}{\partial y^*} + w^*\frac{\partial w^*}{\partial z^*} = -\frac{1}{\rho_o}\frac{\partial p^*}{\partial z^*} - \frac{g\rho^*}{\rho_o} + A_H\left(\frac{\partial^2 w^*}{\partial x^{*2}} + \frac{\partial^2 w^*}{\partial y^{*2}}\right) + A_V\frac{\partial^2 w^*}{\partial z^{*2}} \tag{2.1c}$$

$$\frac{\partial u^*}{\partial x^*} + \frac{\partial v^*}{\partial y^*} + \frac{\partial w^*}{\partial z^*} = 0 \tag{2.1d}$$

where $u^*$, $v^*$ and $w^*$ are the velocity components in the $x^*$, $y^*$ and $z^*$ directions, respectively. $p^*$ is the pressure and $\rho^*$ is the density with a mean value $\rho_o$. $f^* = f_o + \beta^* y^*$ is the Coriolis parameter. $A_H$ and $A_V$ are the horizontal and vertical frictional coefficients.

We will nondimensionize (2.1) by length scale $\tilde{L}$, depth $\tilde{H}$, velocity $\tilde{U}$ and density variation $\Delta\tilde{\rho}$. An advection time scale $\tilde{L}/\tilde{U}$ is used. The nondimensional variables are defined as follows:

$$x^* = \tilde{L}x; \quad y^* = \tilde{L}y; \quad z^* = \tilde{H}z; \quad t^* = (\tilde{L}/\tilde{U})t$$

$$u^* = \tilde{U}u; \quad v^* = \tilde{U}v; \quad w^* = \frac{\tilde{H}}{\tilde{L}}\tilde{U}w$$

$$f^* = f_o f; \quad f = 1 + \beta y; \quad \beta = \beta^*\tilde{L}/f_o$$

$$p^* = -\rho_o g z^* + \rho_o f_o \tilde{U}\tilde{L}\,p$$

$$\rho^* = \rho_o + \Delta\tilde{\rho}\,\rho$$

$\tilde{L}$ can be chosen as the width of topographic variations. $\tilde{H}$ is the depth at the shelf break. The velocity scale $\tilde{U}$ depends on the forcing applied and is different for each problem. The nondimensional equations are

$$\varepsilon_R \left(\frac{\partial u}{\partial t} + u\frac{\partial u}{\partial x} + v\frac{\partial u}{\partial y} + w\frac{\partial u}{\partial z}\right) - fv = -\frac{\partial p}{\partial x} + \frac{E_H}{2}\left(\frac{\partial^2 u}{\partial x^2} + \frac{\partial^2 u}{\partial y^2}\right) + \frac{E_v}{2}\frac{\partial^2 u}{\partial z^2} \qquad (2.2a)$$

$$\varepsilon_R \left(\frac{\partial v}{\partial t} + u\frac{\partial v}{\partial x} + v\frac{\partial v}{\partial y} + w\frac{\partial v}{\partial z}\right) + fu = -\frac{\partial p}{\partial y} + \frac{E_H}{2}\left(\frac{\partial^2 v}{\partial x^2} + \frac{\partial^2 v}{\partial y^2}\right) + \frac{E_v}{2}\frac{\partial^2 v}{\partial z^2} \qquad (2.2b)$$

$$D^2 \varepsilon_R \left(\frac{\partial w}{\partial t} + u\frac{\partial w}{\partial x} + v\frac{\partial w}{\partial y} + w\frac{\partial w}{\partial z}\right) = -\frac{\partial p}{\partial z} - \sigma\rho + D^2\left[\frac{E_H}{2}\left(\frac{\partial^2 v}{\partial x^2} + \frac{\partial^2 v}{\partial y^2}\right) + \frac{E_v}{2}\frac{\partial^2 v}{\partial z^2}\right] \qquad (2.2c)$$

$$\frac{\partial u}{\partial x} + \frac{\partial v}{\partial y} + \frac{\partial w}{\partial z} = 0 \qquad (2.2d)$$

where

$\varepsilon_R = \tilde{U}/(f_o\tilde{L})$ : Rossby Number

$E_H = 2A_H/(f_o\tilde{L}^2)$ : Horizontal Ekman Number

$E_V = 2A_V/(f_o\tilde{H}^2)$ : Vertical Ekman Number

$D = \tilde{H}/\tilde{L}$ : Aspect Ratio

$f_R = f_o^2\,\tilde{L}/(g\Delta\tilde{\rho}/\rho_o)$ : Internal Froude Number

$\sigma = D/(f_R\varepsilon_R)$ : The Relative Importance of Density Stratification.

At the sea surface, $z^*= 0$, the boundary conditions are $A_V \frac{\partial u^*}{\partial z^*} = \tau_x^*/\rho_o$ $A_V \frac{\partial u^*}{\partial z^*} = \tau_y^*/\rho_o$, where $\tau_x^*$ and $\tau_y^*$ are the x- and y-components of wind

stress with magnitude $\tilde{\tau}$. In nondimensional form, they are

$$\frac{E_v}{2}\frac{\partial u}{\partial z} = \tau_0 \tau_x$$
$$\text{at } z = 0 \qquad (2.3)$$
$$\frac{E_v}{2}\frac{\partial v}{\partial z} = \tau_0 \tau_y$$

where $\tau_0 = \tilde{\tau}/(\rho_0 f_0 \tilde{U} \tilde{H})$ determines the relative importance of wind stress to the flow.

At the ocean bottom, we can use the boundary layer analysis to solve the Ekman layer problem on a slope (e.g. Pedlosky, 1979, Section 4.9). However, the applicability of this analysis is ambiguous, when the water shoals to Ekman depth near the coast. An alternate simpler approach is to parameterize the bottom friction via a linear drag law. Let r be the proportional constant, the bottom stress can be written as

$$A_v \frac{\partial u^*}{\partial z^*} = ru^*$$
$$\text{at } z^* = -h^*(x^*)$$
$$A_v \frac{\partial v^*}{\partial z^*} = rv^*$$

In nondimensional form, they are

$$\frac{E_v}{2}\frac{\partial u}{\partial z} = \varepsilon u$$
$$\text{at } z = -h(x) \qquad (2.4)$$
$$\frac{E_v}{2}\frac{\partial v}{\partial z} = \varepsilon v$$

where $\varepsilon = r/(f_0 \tilde{H})$.

Equation (2.4) is physically more realistic, when the water depth is of the same order as Ekman depth. It has been used frequently in shelf

circulation problems (e.g. Csanady, 1976, 1978). Scott and Csanady (1976) found r to be 0.1 cm/sec from the data taken off the Long Island coast. It is probably on the high side. The recently accepted values are between 0.05 cm/sec to 0.1 cm/sec (Winant and Beardsley, 1979; Pettigrew, 1981). Equation (2.4) is equivalent to the bottom Ekman layer solution, if the geostrophic approximation on the bottom velocity is made. The correspondence between them is $\epsilon = E_V^{1/2}/2$. The values for $\epsilon$ and $E_V$ corresponding to r = 0.05 cm/sec and H = 100 m are 0.05 and 0.01, respectively. The equivalent $A_V$ is found to be 50 $cm^2$/sec, which agrees with the values in common use for $A_V$. Table 2.1 lists the values of nondimensional parameters pertaining to the western North Atlantic shelf.

TABLE 2.1

Scaling Parameters and Nondimensional Numbers Independent of Forcing

| | | |
|---|---|---|
| $\tilde{L}$ | Horizontal Length | 100 km |
| $\tilde{H}$ | Depth at Shelf Break | 100 m |
| D | Aspect Ratio | $10^{-3}$ |
| $f_o$ | Mean Coriolis Parameter | $10^{-4}$ $sec^{-1}$ |
| $A_H$ | Horizontal Eddy Viscosity | $10^6$ $cm^2$/sec |
| $E_H$ | Horizontal Ekman Number | $2 \times 10^{-4}$ |
| r | Frictional Coefficient | 0.05 cm/sec |
| $\epsilon$ | Nondimensional Frictional Coefficient | 0.05 |

Using Equations (2.3) and (2.4), we can integrate (2.2a) and (2.2b) from the bottom of the ocean to the surface. These equations lead to

$$\varepsilon_R \int_{-h}^{0} \left(\frac{\partial u}{\partial t} + u\frac{\partial u}{\partial x} + v\frac{\partial u}{\partial y} + w\frac{\partial u}{\partial z}\right) dz - \int_{-h}^{0} fv\, dz = -\int_{-h}^{0} \frac{\partial p}{\partial x} dz + \frac{E_H}{2} \int_{-h}^{0} \left(\frac{\partial^2 u}{\partial x^2} + \frac{\partial^2 u}{\partial y^2}\right) dz + \tau_0 \tau_x - \varepsilon u_h \quad (2.5a)$$

$$\varepsilon_R \int_{-h}^{0} \left(\frac{\partial v}{\partial t} + u\frac{\partial v}{\partial x} + v\frac{\partial v}{\partial y} + w\frac{\partial v}{\partial z}\right) dz + \int_{-h}^{0} fu\, dz = -\int_{-h}^{0} \frac{\partial p}{\partial y} dz + \frac{E_H}{2} \int_{-h}^{0} \left(\frac{\partial^2 v}{\partial x^2} + \frac{\partial^2 v}{\partial y^2}\right) dz + \tau_0 \tau_y - \varepsilon v_h \quad (2.5b)$$

where $u_h$ and $v_h$ are the velocity components at the bottom.

Mean longshore velocity over a period longer than one month is about 5 cm/sec on the continental shelf. In this case, the Rossby number is 0.005, which is an order of magnitude smaller than $\varepsilon$. $E_H$ is much smaller than $\varepsilon$ (Table 2.1). We expect that the lateral friction and nonlinear advection terms in (2.5) are negligible. We will show in the next section that the cross-shelf momentum balance is approximately geostrophic to the leading order both in the interior region and inside the boundary layer, and the term $\varepsilon u_h$ in (2.5a) is small to the order $\varepsilon$. Therefore, we replace $v_h$ by its geostrophic counterpart and neglect the $\varepsilon u_h$ term. These assumptions have been shown to be approximately true by the near-shore current measurements south of Long Island (Pettigrew, 1981).

Typically, $D \ll 1$ on the shelf. Equation (2.2c) is, in a good approximation, the same as the hydrostatic equation. The depth-integrated continuity equation is the conservation of total transport. With the above approximations, (2.5a, b) and (2.2c, d) become

$$-fV = -\int_{-h}^{0} \frac{\partial p}{\partial x}\, dz + \tau_o \tau_x \tag{2.6a}$$

$$fU = -\int_{-h}^{0} \frac{\partial p}{\partial y}\, dz + \tau_o \tau_y - \varepsilon v_b \tag{2.6b}$$

$$0 = -\frac{\partial p}{\partial z} - \sigma\rho \tag{2.6c}$$

$$\frac{\partial U}{\partial x} + \frac{\partial V}{\partial y} = 0 \tag{2.6d}$$

where the capital letters U and V represent the components of total transport in the x and y directions. The boundary condition at the coast is the no normal flow condition, i.e.:

$$U = 0 \qquad \text{at } x = 0 \tag{2.7}$$

The other boundary conditions will depend on each problem considered. For localized forcing, we expect the disturbances to die out far away from the forcing region. For deep-ocean/shelf interaction, we need a boundary condition at the seaward boundary of the shelf.

2.2 Decomposition of Velocity Field

Because of the large variations in bottom topography on the shelf, the usual decomposition of velocity components into normal modes is not possible. In this section, an alternate way of decomposition is used, and the equations are thus simplified. Conventionally, the geostrophic velocity is separated into a barotropic mode which contains all the

horizontal transports, and several baroclinic modes which have zero net transports. Throughout this work, they are defined differently.

The decomposition is achieved through the hydrostatic relation (2.6c). The pressure at a depth z can be found from the surface pressure and the internal density distribution by integrating (2.6c):

$$p = p_s + \sigma\int_z^0 \rho \, dz \tag{2.8}$$

The x-derivative of p is

$$\frac{\partial p}{\partial x} = \frac{\partial p_s}{\partial x} + \sigma\int_z^0 \frac{\partial \rho}{\partial x} dz = \left(\frac{\partial p_s}{\partial x} + \sigma\int_{-h}^0 \frac{\partial \rho}{\partial x} dz\right) - \sigma\int_{-h}^z \frac{\partial \rho}{\partial x} dz \tag{2.9}$$

Because $\frac{1}{f}\frac{\partial p}{\partial x}$ equals the y-geostrophic velocity, (2.9) suggests that it can be written in terms of two components. The bottom geostrophic velocity $v_b$ is given by

$$v_b = \frac{1}{f}\left(\frac{\partial p_s}{\partial x} + \sigma\int_{-h}^0 \frac{\partial \rho}{\partial x} dz\right) \tag{2.10}$$

which is the geostrophic velocity evaluated at the bottom and is depth-independent. The thermohaline velocity $v_c$ is the geostrophic velocity evaluated with the bottom as a reference:

$$v_c = -\frac{\sigma}{f}\int_{-h}^z \frac{\partial \rho}{\partial x} dz \tag{2.11}$$

Obviously, $v_c$ satisfies the thermal wind relation. Similar equations for x-bottom geostrophic velocity are

$$u_b = -\frac{1}{f}\left(\frac{\partial p_s}{\partial y} + \sigma\int_{-h}^{0}\frac{\partial \rho}{\partial y}\,dz\right) \tag{2.12}$$

$$u_c = \frac{\sigma}{f}\int_{-h}^{z}\frac{\partial \rho}{\partial y}\,dz \tag{2.13}$$

The transports associated with these components are given by

$$V_b = hv_b \tag{2.14}$$

$$V_c = \int_{-h}^{0} v_c dz = \frac{\sigma}{f}\int_{-h}^{0} z\,\frac{\partial \rho}{\partial x}\,dz \tag{2.15}$$

$$U_b = hu_b \tag{2.16}$$

$$U_c = \int_{-h}^{0} u_c\,dz = -\frac{\sigma}{f}\int_{-h}^{0} z\,\frac{\partial \rho}{\partial y}\,dz \tag{2.17}$$

Equations (2.10) and (2.12) can be used to eliminate $p_s$. The resulting equation is

$$\frac{\partial}{\partial x}(\,fu_b\,) + \frac{\partial}{\partial y}(\,fv_b\,) = -\sigma\alpha(x)\,\frac{\partial \rho_b}{\partial y} \tag{2.18}$$

where $\alpha(x)$ is the bottom slope and $\rho_b$ is the density at $z = -h(x)$. In general, when $\beta v_b \neq 0$, or when the constant density lines at the bottom cross isobaths, the bottom geostrophic velocity is divergent. Equation (2.6d) can be used to eliminate U and V from (2.6a) and (2.6b), resulting in the relation

$$\varepsilon \frac{\partial v_b}{\partial x} - f\alpha u_b + \beta h v_b = \frac{\tau_0}{f} F - \frac{\beta\sigma}{f}\int_{-h}^{0} z \frac{\partial \rho}{\partial x}\, dz \qquad (2.19)$$

where the definitions of $u_b$ and $v_b$ have been used, and F is given by

$$F = f^2\left[\frac{\partial}{\partial x}\left(\frac{\tau_y}{f}\right) - \frac{\partial}{\partial y}\left(\frac{\tau_x}{f}\right)\right]$$

The coastal boundary condition (2.7) can be written in terms of $u_b$ and $v_b$ as

$$\varepsilon v_b = f h u_b - \sigma \int_{-h}^{0} z \frac{\partial \rho}{\partial y}\, dz + \tau_0 \tau_y \qquad \text{at } x = 0 \qquad (2.20)$$

Equations (2.18) to (2.20), with other appropriate boundary conditions, can be solved for $u_b$ and $v_b$ diagnostically. The thermohaline components are readily found from the density distribution, and the velocity field is obtained. In the next section, a density equation is derived in terms of $u_b$ and $v_b$. It is possible to solve the problem prognostically. We will discuss the characteristics of Equations (2.18) and (2.19) in the rest of this section. The order of magnitude of the flow contributed by the wind and density forcing components will be estimated.

Over the continental shelves, $\beta$ is small. Equations (2.18) and (2.19) can be combined into a single equation for $u_b$. It is

$$\varepsilon \frac{\partial^2 u_b}{\partial x^2} + f\alpha \frac{\partial u_b}{\partial y} = -\frac{\varepsilon\sigma}{f}\frac{\partial}{\partial x}\left(\alpha \frac{\partial \rho_b}{\partial y}\right) - \frac{\tau_0}{f}\frac{\partial F}{\partial y} \qquad (2.21)$$

Here f may be chosen to be +1 to represent the Northern Hemisphere.

Equation (2.21) is interpreted as a heat equation with -y as the time-like coordinate. Assuming that the forcing is zero in the region $y > y_0$, then both $u_b$ and $v_b$ vanish there. At the coast, a topographic boundary layer of width $(\varepsilon L_y/\alpha_0)^{1/2}$ exists, where $L_y$ is a nondimensional longshore length scale and $\alpha_0$ is the mean slope in the nondimensional coordinate system. We will use the superscripts "I" and "B" to represent the interior and boundary layer solutions respectively. The interior solution is found by letting $\varepsilon = 0$ in (2.19). We have

$$u_b^I = -\frac{\tau_0 F}{\alpha} \tag{2.22}$$

From (2.18), $v_b^I$ is expressed as

$$v_b^I = -\alpha\sigma(\rho_b - \bar{\rho}_b) + \tau_0 \int_{y_0}^{y} \frac{\partial}{\partial x}\left(\frac{F}{\alpha}\right) dy \tag{2.23}$$

where $v_b^I = 0$ at $y = y_0$ has been used and $\bar{\rho}_b(x, y_0)$ is the bottom density at $y = y_0$. Let $v_b^B = v_b - v_b^I$ and $u_b^B = u_b - u_b^I$.
The equations in terms of boundary layer variables derived from (2.18) and (2.19) are:

$$\varepsilon \frac{\partial v_b^B}{\partial x} - \alpha u_b^B = O(\varepsilon) \tag{2.24}$$

$$\frac{\partial u_b^B}{\partial x} + \frac{\partial v_b^B}{\partial y} = 0 \tag{2.25}$$

From (2.25), we can express $u_b^B$ and $v_b^B$ by a stream function $\phi^B$ such

that

$$u_b^B = -\frac{\partial \phi^B}{\partial y} \tag{2.26}$$

$$v_b^B = \frac{\partial \phi^B}{\partial x} \tag{2.27}$$

To the leading order, Equation (2.24) can be rewritten as

$$\epsilon \frac{\partial^2 \phi^B}{\partial x^2} + \alpha \frac{\partial \phi^B}{\partial y} = 0 \tag{2.28}$$

If the water depth is zero at the coast, the leading order balance in (2.20) is

$$\epsilon \frac{\partial \phi^B}{\partial x} = \tau_o \tau_y - \epsilon v_b^I \qquad \text{at } x = 0 \tag{2.29}$$

For simplicity, we assume that $\alpha$ is of order one and the forcing is over a unit longshore distance. Equations (2.22) and (2.23) show that the interior flow driven by wind stress curl is of the order $\tau_o$ in both the x and y directions. The interior density-driven flow is of different characteristics from the wind-driven one. The magnitude of the interior flow produced by an order one density disturbance is estimated to be $\sigma$ from (2.23). However, the cross-shelf interior flow, given by (2.19), is at most of the order $\epsilon$. In both wind- and density-driven cases, the bottom friction terms are of the order $\epsilon$ in the interior region. Inside the coastal boundary layer, (2.28) demonstrates

that the cross-shelf length scale is $\varepsilon^{1/2}$ for a unit longshore forcing scale. The order of magnitude for the flow in a boundary layer can be estimated from (2.29). For the flow forced by a longshore wind stress, $\phi^B$ is of the order $\tau_0\varepsilon^{-1/2}$. The corresponding $u_b^B$ and $v_b^B$ are of magnitudes $\tau_0\varepsilon^{-1/2}$ and $\tau_0/\varepsilon$ respectively. In the density-driven case, (2.29) shows that $\phi^B$ is of the order $\sigma\varepsilon^{1/2}$ with a boundary layer flow of the order $\sigma\varepsilon^{1/2}$ and $\sigma$ in the x and y directions respectively. Therefore, the coastal boundary layers in the density-driven circulation are less important than in the wind-driven case. The above estimation of the order of magnitude clearly shows that the relation $\varepsilon u_b^B << \tau_0 << v_b^B$ is always satisfied if $\varepsilon << 1$. Therefore, the use of the quasi-geostrophic approximation and the neglect of $\varepsilon u_h$ term in deriving equations (2.6a,b) from (2.5a,b) are justified.

2.3 Discussion

The decomposition of velocity field into a bottom velocity and a thermohaline velocity is not new. A similar decomposition was used by Fofonoff (1962) and later by several others in diagnostic ocean circulation models (e.g. Sarkisyan, 1977). There is a crucial difference between Fofonoff's decomposition and the presented one. Fofonoff's expression for the "barotropic" transport is the same as (2.14). However, the "baroclinic" component is different from that given by (2.15) because of his neglect of the specific volume anomaly at the bottom. With the notation of Section 2.2, Fofonoff's "baroclinic" transport may be written as

$$\frac{\sigma}{f}\frac{\partial}{\partial x}\int_{-h}^{0} z\rho\, dz = \frac{\sigma}{f}\int_{-h}^{0} z\frac{\partial\rho}{\partial x}\, dz - \frac{\sigma h}{f}\alpha\rho_b$$

No such approximation is made in (2.11). The difference is presumably unimportant in the deep ocean circulation, because the horizontal density variation is nearly zero at the bottom. When the shelf circulation is concerned, horizontal density differences at the bottom become so important that they are the main driving force of the depth-independent component of the flow. Unlike Fofonoff's decomposition, the presented one is more general and valid even when the bottom reaches the level with large horizontal density variations. Pedlosky (1974) also applied this decomposition implicitly. The topographic boundary layer in Section 2.2 is the same as that in his model. Equation (2.23) is similar to his solution for the interior velocity at the bottom, which includes the effect of longshore bottom density variations. In a homogeneous fluid, Equation (2.28) is equivalent to the one in Csanady's (1978) arrested topographic wave model, where the thermohaline component vanishes.

The idea of decomposition was also used by Csanady (1979) in studying the steric set-up along the continental margins of the western North Atlantic Ocean. Csanady (1979) expressed the sea level elevation by a contour integral on the density field. The integral can be interpreted as the sum of two constituents: (1) the integral of the bottom velocity outside the coastal boundary layer, defined by (2.23), along an integration path at the ocean bottom from a reference isobath (4000 m in his calculation) to the location where the sea level is to be calculated; (2) the integral of the thermohaline velocity at the sea surface, given by (2.11) with $z = 0$, along an integration path in the water column from the bottom to the surface. This representation of sea level elevation is

possible if the bottom geostrophic velocity is nondivergent. However, when the bottom density varies along isobaths, Equation (2.18) shows that the bottom geostrophic velocity becomes divergent and Csanady's method of integration can not be used.

Equations (2.18) and (2.19) thus provide a general method for the diagnostic calculation of ocean circulation with the presence of density variations at the bottom. In a special case of no long-isobath density differences, Csanady's (1979) method suggests the integration of (2.11) and (2.24) from a deep reference level to the surface for calculating the dynamic height along the continental margins. This dynamic height calculation provides a theoretical base for the classical method used by Montgomery (1941) and readily has practical applications.

## 2.4 The Density Equation

Horizontal density advection will be taken into account in a simplified way because, in its general form, the three-dimensional density equation is intractable. The problem is simpler when the water column is nearly homogeneous vertically. Under this condition, the density equation may be depth-integrated and the dependence on the z-coordinate is eliminated. It is possible to extend this depth-integration to the vertically stratified case, if the horizontal density gradient is approximately independent of depth. The density equation in the dimensional form is

$$\frac{\partial \rho^*}{\partial t^*} + u^* \frac{\partial \rho^*}{\partial x^*} + v^* \frac{\partial \rho^*}{\partial y^*} + w^* \frac{\partial \rho^*}{\partial z^*} = K_H \left( \frac{\partial^2 \rho^*}{\partial x^{*2}} + \frac{\partial^2 \rho^*}{\partial y^{*2}} \right) + K_V \frac{\partial^2 \rho^*}{\partial z^{*2}} \qquad (2.30)$$

where $K_H$ and $K_V$ are the horizontal and vertical diffusion coefficients. Other variables are the same as those in the earlier sections.

The ratio of the vertical advection term to the longshore advection term is estimated by approximating w* and v* with $u_b^* \alpha^*$ and $v_b^*$, where $\alpha^*$ is the actual bottom slope. The result is

$$\frac{\left| w^* \frac{\partial \rho^*}{\partial z^*} \right|}{\left| v^* \frac{\partial \rho^*}{\partial y^*} \right|} \sim \frac{\alpha^* u_b^*}{v_b^*} \frac{\left| \frac{\partial \rho^*}{\partial z^*} \right|}{\left| \frac{\partial \rho^*}{\partial y^*} \right|} \tag{2.31}$$

In the density-driven case, (2.18) and (2.19) show that $u_b^*/v_b^* \sim \varepsilon$ outside the topographic boundary layer. The vertical advection is negligible, if

$$\left| \alpha^* \frac{\partial \rho^*}{\partial z^*} \right| \ll \frac{1}{\varepsilon} \left| \frac{\partial \rho^*}{\partial y^*} \right| \tag{2.32}$$

For a density difference of $0.3 \times 10^{-3}$ gm/cm$^3$ in a longshore distance of 100 km, $\varepsilon = 0.05$ and $\alpha^* = 10^{-3}$, we require $\frac{\partial \rho^*}{\partial z^*} \ll 6 \times 10^{-7}$ gm/cm$^4$ or a density difference of $6 \times 10^{-3}$ gm/cm$^3$ in 100 m of water. Inside the topographic boundary layer, $u_b^*/v_b^* \sim \varepsilon^{1/2}$. Equation (2.32) is satisfied, if $\Delta\rho^* \ll 3 \times 10^{-4}$ gm/cm$^3$ in a water depth of 20 m. Subsequently, we will neglect the vertical advection term when considering the density-driven flow over the continental shelf in winter.

At the surface, the density flux condition is given by

$$K_v \frac{\partial \rho^*}{\partial z^*} = Q^* \qquad \text{at } z^* = 0 \tag{2.33}$$

where Q* is the surface densty flux caused by atmospheric influences (heating, cooling, evaporation, etc.). The bottom condition is the one with no normal diffusion flux:

$$K_H \frac{\partial \rho^*}{\partial x^*} \frac{dh^*}{dx^*} + K_v \frac{\partial \rho^*}{\partial z^*} = 0 \qquad \text{at } z^* = -h^*(x^*) \tag{2.34}$$

At the coast, the river outflow is modelled as a density sink of strength R*:

$$K_H \int_{-h}^{0} \frac{\partial \rho^*}{\partial x^*} dz^* = R^* \qquad \text{at } x^* = 0 \tag{2.35}$$

For other horizontal boundaries, we require $\rho^* = 0$ away from the density sinks or sources. Equation (2.30) is integrated from the bottom to the surface. Making use of (2.33) and (2.34), we have

$$\frac{\partial}{\partial t^*}\int_{-h^*}^{0} \rho^* dz^* + \int_{-h^*}^{0} \left(u^* \frac{\partial \rho^*}{\partial x^*} + v^* \frac{\partial \rho^*}{\partial y^*}\right) dz^* = K_H \frac{\partial}{\partial x^*}\int_{-h^*}^{0} \frac{\partial \rho^*}{\partial x^*} dz^* + K_H \frac{\partial}{\partial y^*}\int_{-h^*}^{0} \frac{\partial \rho^*}{\partial y^*} dz^* + Q^* \tag{2.36}$$

Equation (2.36) is the conservation of density in a vertical column. The nondimensional form of (2.36) is

$$\frac{\partial}{\partial t}\int_{-h}^{0} \rho\, dz + \int_{-h}^{0} \left(u \frac{\partial \rho}{\partial x} + v \frac{\partial \rho}{\partial y}\right) dz = \gamma \frac{\partial}{\partial x}\int_{-h}^{0} \frac{\partial \rho}{\partial x} dz + \gamma \frac{\partial}{\partial y}\int_{-h}^{0} \frac{\partial \rho}{\partial y} dz + Q_0 Q \tag{2.37}$$

where $\gamma = K_H/(\epsilon_R f_0 \tilde{L}^2)$ is the nondimensional diffusivity, and $Q_0 = \tilde{Q}/(f_0 \epsilon_R \tilde{H} \Delta\tilde{\rho})$ is the nondimensional surface density flux. The coastal boundary condition for a river density flux with scale $\tilde{R}$ is given by

$$\gamma \int_{-h}^{0} \frac{\partial \rho}{\partial x}\, dz = R_0 R \qquad \text{at } x = 0 \tag{2.38}$$

where $R_0 = \tilde{R}/(\epsilon_R f_0 \tilde{H}\tilde{L}\Delta\tilde{\rho})$ is the nondimensional coastal buoyancy flux.

Simplification of (2.29) is made by assuming $\frac{\partial \rho}{\partial x}$ and $\frac{\partial \rho}{\partial y}$ independent of depth. We also require that the vertical stratification varies in a time much longer than the advection time. The density advection term becomes

$$\int_{-h}^{0} (u \frac{\partial \rho}{\partial x} + v \frac{\partial \rho}{\partial y})\, dz = U \frac{\partial \rho}{\partial x} + V \frac{\partial \rho}{\partial y} \tag{2.39}$$

where U and V are the total transports given by (2.6a) and (2.6b). Only the transports associated with the bottom geostrophic velocity and the bottom frictional velocity can effectively advect the density field under the assumption of vertical homogeneity of the horizontal density gradient, since

$$\begin{aligned} U_c \frac{\partial \rho}{\partial x} + V_c \frac{\partial \rho}{\partial y} &= -\frac{\sigma}{f}\left(\int_{-h}^{0} z \frac{\partial \rho}{\partial y}\, dz\right)\frac{\partial \rho}{\partial x} + \frac{\sigma}{f}\left(\int_{-h}^{0} z \frac{\partial \rho}{\partial x}\, dz\right)\frac{\partial \rho}{\partial y} \\ &= \frac{\sigma}{f} h^2 \left(\frac{\partial \rho}{\partial y}\frac{\partial \rho}{\partial x} - \frac{\partial \rho}{\partial x}\frac{\partial \rho}{\partial y}\right) \\ &= 0 \end{aligned}$$

It follows that (2.37) can be rewritten as

$$h \frac{\partial \bar{\rho}}{\partial t} + (h u_b - \varepsilon v_b)\frac{\partial \rho}{\partial x} + (h v_b + \varepsilon u_b)\frac{\partial \rho}{\partial y} = \gamma \frac{\partial}{\partial x}\left(h \frac{\partial \rho}{\partial x}\right) + \gamma \frac{\partial}{\partial y}\left(h \frac{\partial \rho}{\partial y}\right) + Q_0 Q$$

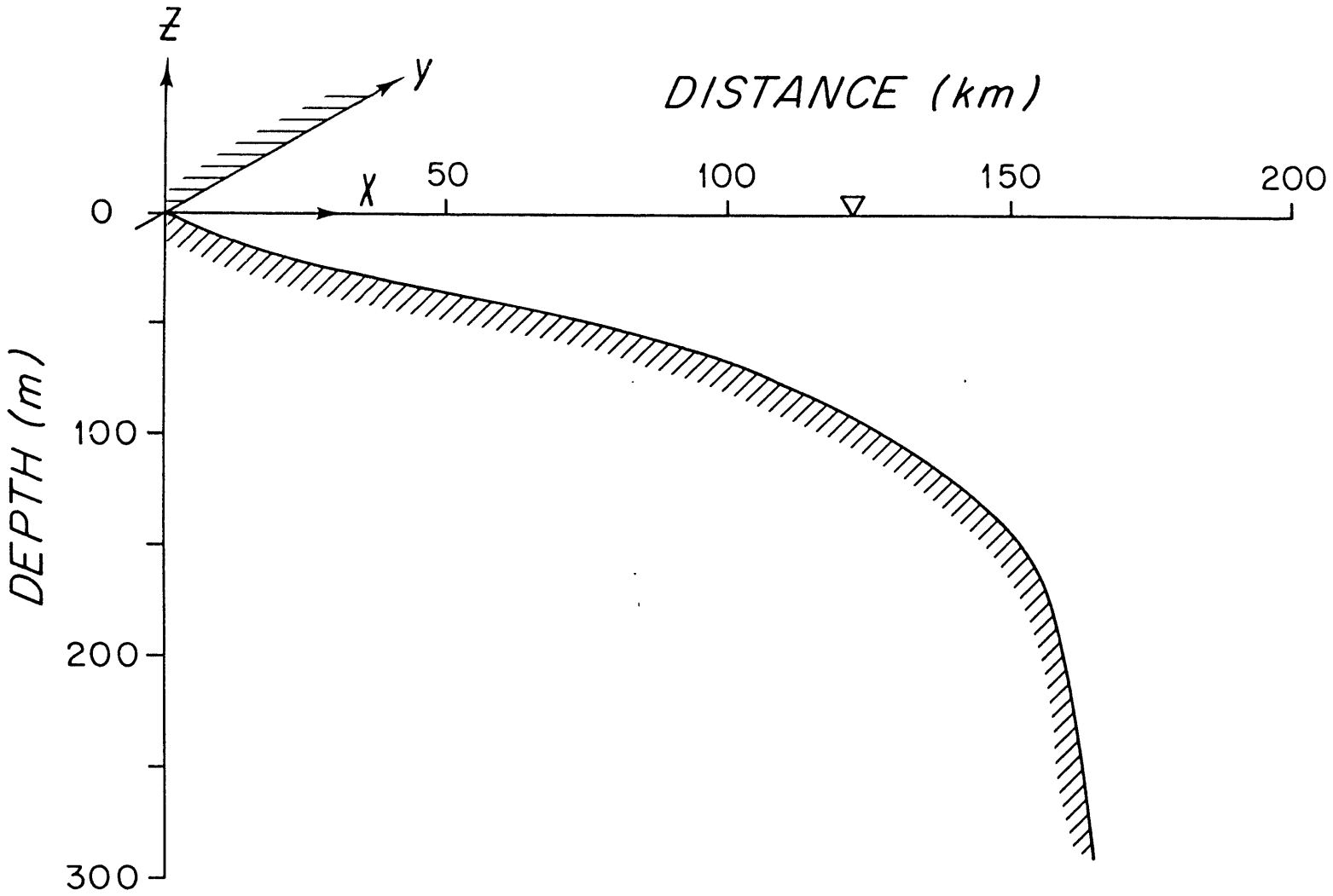
where $\bar{\rho}$ is the mean density in a water column. Under winter vertically

homogeneous condition, $\rho$ and $\bar{\rho}$ are the same as $\rho_b$. We have

$$h\frac{\partial \rho_b}{\partial t}+(hu_b-\varepsilon v_b)\frac{\partial \rho_b}{\partial x}+(hv_b+\varepsilon u_b)\frac{\partial \rho_b}{\partial y}=\gamma\frac{\partial}{\partial x}(h\frac{\partial \rho_b}{\partial x})+\gamma\frac{\partial}{\partial y}(h\frac{\partial \rho_b}{\partial y})+Q_o Q \tag{2.40}$$

Equation (2.40) and the momentum equations (2.18) and (2.19) form a complete set. In the following chapters they will be applied to the mean shelf circulation under various forcing conditions.

Figure 2.1 Schematic diagram showing the coordinate system.


Z
y
X
DISTANCE (km)
0
50
100
150
200
DEPTH (m)
100
200
300

# CHAPTER 3

# THE EFFECT OF STEEP SLOPE ON THE BOTTOM PRESSURE FIELD

The formulation in the previous chapter shows that bottom geostrophic flow can be generated on continental shelves by wind and long-isobath density variations. In this chapter, we will neglect the long-isobath density variations and concentrate on the analysis of the wind-driven flow. The flow forced by wind stress at the coast and by wind stress curl on the outer shelf and slope will be considered with emphasis on the topographic effects. We will also examine the possible influence of a deep-ocean circulation gyre on the shelf circulation.

## 3.1 Formulation of the Problem

Because of the large offshore topographic variations at continental margins, the forced bottom geostrophic flow at various offshore locations should be different. In order to study the effect of topography on the mean circulation, the bottom topography is idealized as a long and straight coast with bottom depth as a function of the offshore coordinate. The steepness of bottom slope is preserved by choosing a cross-shelf bottom topography representing that in the Middle Atlantic Bight. Figure 3.1 is a plot of the topography which will be used in the subsequent numerical computations. In this figure the depth and the offshore distance are nondimensionalized by scales of 100 m and 100 km respectively.

The nondimensional equations derived in Chapter 2 will be used here. The coordinates are the same as those in Figure 2.1, with x in the

offshore direction and y in the longshore direction. Without the long-isobath density variations, Equation (2.18) shows that the bottom geostrophic velocity is nondivergent and can be written in terms of a stream function $\phi$, which is also a measure of bottom pressure:

$$u_b = -\frac{1}{f}\frac{\partial \phi}{\partial y} \tag{3.1a}$$

$$v_b = \frac{1}{f}\frac{\partial \phi}{\partial x} \tag{3.1b}$$

In a homogeneous fluid, $\phi$ equals g times sea surface elevation. Substituting (3.1a, b) for $u_b$ and $v_b$ in (2.19), the vorticity equation governing the motion becomes

$$-f\alpha \frac{\partial \phi}{\partial y} = \varepsilon \frac{\partial^2 \phi}{\partial x^2} + \beta h \frac{\partial \phi}{\partial x} + \beta \sigma \int_{-h}^{0} z \frac{\partial \rho}{\partial x}\, dz - \tau_0 F \tag{3.2}$$

where $\alpha(x) = dh/dx$ is the bottom slope and $F = f^2[\frac{\partial}{\partial x}(\frac{\tau_y}{f}) - \frac{\partial}{\partial y}(\frac{\tau_x}{f})]$ is f times the curl of wind stress. Equation (3.2) is a parabolic equation, in which the signal propagates to the -y (+y) direction in the Northern (Southern) Hemisphere. In this chapter, we will discuss the case in the Northern Hemisphere (f = +1), and specify -y as the forward direction.

Suppose that the forcing acts only in the region y < 0. The boundary condition at y = 0 is then similar to an initial condition and can be specified as $\phi = 0$. Since the second derivative in y has been neglected, boundary conditions are not needed at the forward side (y < 0). The boundary condition at the coast is obtained by substituting (3.1) into (2.20). The resulting equation is

$$\varepsilon \frac{\partial \phi}{\partial x} + h \frac{\partial \phi}{\partial y} = \tau_0 \tau_y - \sigma \int_{-h}^{0} z \frac{\partial \rho}{\partial y} dz \qquad \text{at } x = 0 \qquad (3.3)$$

where $\tau_y$ is the longshore wind stress. For wind forcing over the shelf and the upper slope, the motion away from the forcing region is small and we have

$$\phi = 0 \qquad \text{at } x \to \infty \qquad (3.4)$$

This seaward boundary condition in the case of deep ocean forcing will be discussed in Section 3.4.

Following Csanady (1978), one may interpret (3.2) as a heat equation, in which $\phi$ is "temperature" and $-y$ is "time". Furthermore, $\varepsilon$ is the thermal conductivity and $\alpha f$ is the heat capacity which is variable for non-constant slope. Two other terms, $\beta h \partial\phi/\partial x$ and $-\tau_0 F + \beta\sigma \int_{-h}^{0} z \frac{\partial \rho}{\partial x} dz$, correspond to the heat advection and the heat source terms respectively. Using this formulation, the effects of coastal wall and steep bottom slope on the mean circulation will be studied in the following sections.

3.2 Local Wind Forcing

Equation (3.2) with the boundary conditions (3.3) and (3.4) are used to estimate the order of magnitude of the flow driven by wind stress and its curl over the shelf and the upper slope. The shelf topography in Figure 3.1 is approximated by a linearly decreasing bottom with slope $\alpha_0$ joined by a much steeper slope of constant magnitude $\alpha_1$ at the shelf break ($x = x_b$). We assume $\alpha_1 >> \alpha_0$. Over the shelf and

upper slope, the terms containing $\beta$ are small, being proportional to the depth, and will be neglected.

3.2.1 Longshore Wind Stress Forcing

Assume that the longshore wind stress is uniform from $y = -L_y$ to $y = 0$. The wind stress curl term in (3.2) vanishes, and the flow is driven by the forcing term in the coastal boundary condition (3.3). We rescale y by $L_y$ such that $y = -L_y\eta$. Equation (3.2) suggests an offshore length scale $\delta = (\varepsilon L_y/\alpha_0)^{1/2}$ near the coast. Let $x = \delta\xi$. In terms of $\xi$ and $\eta$, (3.2) and (3.3) become

$$\frac{\partial \phi}{\partial \eta} = \frac{\partial^2 \phi}{\partial \xi^2} \tag{3.5}$$

$$\frac{\partial \phi}{\partial \xi} - \lambda \frac{\partial \phi}{\partial \eta} = \left(\frac{L_y}{\alpha_0 \varepsilon}\right)^{1/2} \left(\tau_0 \tau_y - \sigma \int_{-h_0}^{0} z \frac{\partial \rho}{\partial y}\, dz\right) \quad \text{at } x = 0 \tag{3.6}$$

where $\lambda = h_0(\varepsilon \alpha_0 L_y)^{-1/2}$ and $h_0$ is the bottom depth at the coast. Equation (3.5) shows that the width of the coastal boundary layer develops as $\eta^{1/2}$ in the $+\eta$ direction. In the case of vanishing bottom depth at the coast, the order of magnitude of $\phi$ is

$$\phi \sim O[\tau_0(\varepsilon \alpha_0 / L_y)^{-1/2}] \tag{3.7a}$$

The corresponding offshore and longshore components of velocity are

$$u_b \sim O[\tau_0(\varepsilon \alpha_0 L_y)^{-1/2}] \tag{3.7b}$$

and

$$v_b \sim O(\tau_0/\varepsilon) \qquad (3.7c)$$

Typical values under a 1 dyne/cm$^2$ longshore stress forcing over 100 km of the coast are listed in Table 3.1, where the length scale and other parameters in Table 2.1 are used.

Table 3.1

Scales and Nondimensional Parameters in the Wind-Driven Case

| | |
|---|---|
| Wind stress, $\tilde{\tau}$ | 1 dyne/cm$^2$ |
| Length scale, $\tilde{L}$ | 100 km |
| Depth, $\tilde{H}$ | 100 m |
| Wind stress curl | $10^{-7}$ dyne/cm$^3$ |
| Coriolis parameter, $f_0$ | $10^{-4}$ sec$^{-1}$ |
| Frictional coefficient, $\varepsilon$ | 0.05 |
| Velocity scale, $\tilde{U}$ | 1 cm/sec |

In the general case $h_0 \neq 0$. The effect of bottom depth at the coast depends on the parameter $\lambda$. For $\lambda << 1$, the term $\lambda \partial\phi/\partial\eta$ in (3.6) is negligible to the order $\lambda$ compared to the term $\partial\phi/\partial\xi$. The solution is therefore not affected by the choice of $h_0$, except in the region very close to the shore. If $\lambda >> 1$, the dominant balance in (3.6) is

$$-\lambda \frac{\partial \phi}{\partial \xi} = \left(\frac{L_y}{\varepsilon a_0}\right)^{1/2} \left(\tau_0 \tau_y - \sigma \int_{-h_0}^{0} z \frac{\partial \rho}{\partial y}\, dz\right) \qquad \text{at } x = 0 \qquad (3.8)$$

which simply states the compensation of offshore surface Ekman transport by the geostrophic onshore flow. Equation (3.8) is equivalent to the coastal boundary condition in Pedlosky's (1974) model. For $\sigma = 0$, $\phi$ is of the order $(L_y/\alpha_0/\varepsilon)^{1/2}\lambda^{-1}\tau_0$, which is $1/\lambda$ times smaller than that with $\lambda = 0$. We can write $\lambda$ in the form

$$\lambda = h_0(\varepsilon\alpha_0 L_y)^{-1/2} = (h_0/\alpha_0)/(\varepsilon L_y/\alpha_0)^{1/2} \qquad (3.9)$$

which is the ratio of the distance between the coastal wall and the apex of the wedge-shaped bottom, to the width of boundary layer. A deep coastal wall will effectively exclude the near-shore circulation and will not change the dynamics of interior flow significantly.

Equation (3.3) is the general boundary condition for coastal circulation problems. It is equivalent to a radiation condition in the heat conduction analogy. This relation is useful because a coastal wall can always be used to exclude the near-shore portion of the shelf when the flow in the interior region is concerned. On the other hand, if the near-shore circulation is of interest, (3.3) can be simplified to a flux condition for zero bottom depth at the coast. One application will be described in the next chapter, where we deal with the density diffusion at the coast. A coastal wall can be used to exclude the singularity in the density equation when $h = 0$.

3.2.2 Wind Stress Curl Forcing

Unlike the longshore wind stress forcing which drives a flow inside a coastal boundary layer, wind stress curl is an interior forcing effect

and the resulting flow has a much larger offshore extent than in the previous case of longshore stress forcing. We assume that the longshore wind stress vanishes at the coast and the surface wind stress curl is non-zero over the shelf and slope from $-L_y$ to 0 in the y direction. Using the same independent variable $\eta$ as in the previous section, we have

$$\frac{\partial \phi_0}{\partial \eta} = \frac{\varepsilon L_y}{\alpha_0} \frac{\partial^2 \phi_0}{\partial x^2} - \frac{\tau_0 L_y}{\alpha_0} F \qquad 0 \le x \le x_b \qquad (3.10a)$$

$$\frac{\partial \phi_1}{\partial \eta} = \frac{\varepsilon L_y}{\alpha_1} \frac{\partial^2 \phi_1}{\partial x^2} - \frac{\tau_0 L_y}{\alpha_1} F \qquad x_b \le x \qquad (3.10b)$$

where $\phi_0$ and $\phi_1$ are the stream functions in the shelf and the slope regions respectively. For $h_0 = 0$, the boundary condition at $x = 0$ becomes an insulating one:

$$\frac{\partial \phi_0}{\partial x} = 0 \qquad \text{at } x = 0 \qquad (3.11)$$

At $x = x_b$, we require the continuity of $\phi$ and $v_b$:

$$\phi_0 = \phi_1 \qquad (3.12a)$$

$$\frac{\partial \phi_0}{\partial x} = \frac{\partial \phi_1}{\partial x} \qquad (3.12b)$$

We also assume that $\phi_1$ vanishes on the seaward boundary and the initial conditions are $\phi_0 = 0$ and $\phi_1 = 0$ at $y = 0$.

To understand the dynamics of the flow under wind stress curl

forcing, Equation (3.2) can be integrated with $\beta = 0$ over an area enclosed by $y = 0$, $y = y_0 < 0$, $x = 0$, and $x = \infty$. It becomes

$$\int_0^\infty \frac{dh}{dx} dx \int_{y_0}^0 \frac{\partial \phi}{\partial y} dy = -\frac{\varepsilon}{f} \int_{y_0}^0 dy \int_0^\infty \frac{\partial^2 \phi}{\partial x^2} dx + \tau_0 f \int_0^\infty dx \int_{y_0}^0 dy \left[ \frac{\partial}{\partial x}\left(\frac{\tau_y}{f}\right) - \frac{\partial}{\partial y}\left(\frac{\tau_x}{f}\right) \right]$$

Using the boundary condition at $y = 0$, it is easy to show, with integration by parts, that the term on the left-hand side of the above equation is the total longshore transport across $y = y_0$. The first term on the right-hand side vanishes, because $\partial\phi/\partial x = 0$ at $x = 0$ and $x = \infty$. The last term is the line integral of wind stress vector along the boundary of integration region. The resulting equation is

$$\int_0^\infty h v_b (y = y_0)\, dx = \frac{\tau_0}{f} \oint \underset{\sim}{\tau} \cdot d\underset{\sim}{s}$$

Therefore, the total Ekman transport out of the section of the shelf between $y = 0$ and $y = y_0$ is compensated by a geostrophic longshore transport across $y = y_0$.

The flow pattern can be examined by boundary layer analysis. For the shelf and slope region outside boundary layers (cf. below), the dominant balance in (3.10a, b) gives a Sverdrup flow across isobaths. It is

$$\frac{\partial \phi_0^I}{\partial \eta} = -\frac{\tau_0 L_y}{\alpha_0} F \qquad 0 \le x \le x_b \qquad (3.13a)$$

$$\frac{\partial \phi_1^I}{\partial \eta} = -\frac{\tau_0 L_y}{\alpha_1} F \qquad x_b \le x \qquad (3.13b)$$

where the superscript "I" indicates interior solutions. $\eta = 0$ is equivalent to an eastern boundary in Stommel's (1948) model. Therefore, $\phi_0 = \phi_1 = 0$. Equations (3.13a, b) can be integrated from $\eta = 0$ in the forward direction of the parabolic equation. We have

$$\phi_0^I = \frac{\tau_0 L_y}{\alpha_0} \int_0^\eta F \, d\eta \qquad 0 \le x \le x_b \qquad (3.14a)$$

$$\phi_1^I = \frac{\tau_0 L_y}{\alpha_1} \int_0^\eta F \, d\eta \qquad x_b \le x \qquad (3.14b)$$

The interior response on the slope is then $\alpha_0/\alpha_1$ times smaller than that on the shelf. Typically, $\alpha_0/\alpha_1 \simeq 1/50$. We expect that the change in sea surface elevation caused by wind forcing is weak on the slope. The offshore velocity is found from (3.13a, b):

$$u_b^I = \frac{\tau_0 F}{\alpha_0} \qquad 0 \le x \le x_b \qquad (3.14c)$$

$$u_b^I = \frac{\tau_0 F}{\alpha_1} \qquad x_b \le x \qquad (3.14d)$$

The longshore velocity is

$$v_b^I = \tau_0 L_y \int_0^\eta \frac{\partial}{\partial x}\left(\frac{F}{\alpha_0}\right) d\eta \qquad 0 \le x \le x_b \qquad (3.14e)$$

$$v_b^I = \tau_0 L_y \int_0^\eta \frac{\partial}{\partial x}\left(\frac{F}{\alpha_1}\right) d\eta \qquad x_b \le x \qquad (3.14f)$$

In the wind stress curl forcing case, the longshore and the offshore flow

are of comparable strength in the forcing region. The maximum longshore flow is weaker by a factor $\varepsilon L_y/\alpha_0$ than that under longshore stress forcing. Table 3.1 also lists these flow parameters for 1 dyne/cm$^2$ variation in offshore wind stress over a longshore distance of 100 km.

In the region $y < -L_y$, the onshore interior bottom flow in (3.14c, d) is identically zero, and the bottom pressure is caused by the forward influence of the pressure field in the forcing region. In the heat conduction analogy, the pressure field is created by an initial "temperature" distribution at $y = -L_y$, which is given by evaluating (3.14a, b) at $\eta = 1$. For a steep slope with $\delta << 1$, the initial distribution of bottom pressure decays slowly, and the longshore velocity is about the same as that inside the forcing region.

Besides the coastal boundary layers discussed in the previous section, boundary layers also exist at the shelf break, where an abrupt change of bottom slope occur. These boundary layers are required to satisfy the conditions (3.12a, b). Since the boundary layer width is inversely proportional to $\alpha^{1/2}$, the boundary layer on the slope is $(\alpha_0/\alpha_1)^{1/2}$ times narrower than that on the shelf. According to (3.12b), $\phi_1$ must be $(\alpha_0/\alpha_1)^{1/2}$ times smaller than $\phi_0$. For a very steep continental slope, the effective boundary condition for the flow on the shelf is then

$$\phi_0 = 0 \qquad \text{at } x = x_b \tag{3.15}$$

The error in using (3.15) is of the order $(\alpha_0/\alpha_1)^{1/2}$. The heat

conduction analog to the continental slope is a material of very large heat capacity, while the shelf is of small heat capacity. As far as shelf circulation is concerned, the slope is effectively a constant temperature boundary.

If the forcing is limited on the slope, $\phi_0$ is, at most, of the same order as $\phi_1$. To satisfy (3.12b), the much larger length scale on the shelf requires

$$\frac{\partial \phi_1}{\partial x} = 0 \qquad \text{at } x = x_b \tag{3.16}$$

Equation (3.16) is the same as the coastal boundary condition in the case of a vanishing coastal wall [Equation (3.11)]. Therefore, the circulation on the slope is not altered whether the continental slope shoals to zero depth at the coast or joins a gentle shelf at the shelf break. In the heat conduction analogy, the boundary of a material with large heat capacity located in an environment of small heat capacity can be considered as insulating, since only a relatively small amount of heat will leak out. Equation (3.16) also shows that the bottom pressure is nearly constant across the boundary layer on the slope. If there is a longshore pressure gradient over the slope, it will fall onto the shelf/slope boundary. Therefore, the use of a longshore pressure gradient as boundary condition at the shelf break to parameterize the deep ocean influence, e.g. in Csanady's (1978) model, is justified.

In summary, the discussion in this section deduces some characteristics of the steady circulation over the shelf and slope. In

dealing with the circulation on the shelf, the continental slope acts as a boundary, where the bottom pressure is prescribed. This bottom pressure is more or less constant across the slope region. In particular, with vanishing forcing on the slope, it is expressed by (3.15). For circulation over the slope, the shelf is a boundary with vanishing normal pressure gradient given by (3.16). These inferences are useful in studying the circulation over continental margins.

In order to apply these inferences, some cautious notes must be made. Equations (3.15) and (3.16) are valid only to the leading order. Therefore, (3.16) does not imply $\partial\phi_0/\partial x = 0$, because $\partial\phi_0/\partial x$ is one order of magnitude smaller than $\partial\phi_1/\partial x$. It is also incorrect to derive $\phi_1 = 0$ from (3.15) for the flow on the slope. The boundary conditions would be over-specified, if $\phi_1 = 0$ and $\partial\phi_0/\partial x = 0$ were used.

3.3 Numerical Solutions

Equation (3.2) is solved numerically over topography simulating the Middle Atlantic Bight, which is characterized by a two-order of magnitude variation in the bottom slope (Figure 3.1). The shelf and slope regions are infinitely long in the y direction with isobaths parallel to the coast. We will assume that the wind forcing is limited from $-L_y$ to 0 in the y direction, which is represented by a half-period sine wave with a peak value of $\pi/2$ so that a unit mean wind stress is obtained in the forcing region. We will chose $\sigma = 0$ in this section. Because the forcing can influence the forward portion of the shelf only, an initial condition $\phi = 0$ is used at $y = 0$. Equation (3.3) is the boundary condition at the coast. The boundary condition (3.4) is applied at the

2000 m isobath. To simplify the interpretation, $\phi$ will be considered as the nondimensional sea surface elevation. The dimensional scales in Table 3.1 are used.

The computation starts from y = 0 and progresses in the -y direction. For each value of y, Equation (3.2) is solved by the Euler modified scheme to have second order accuracy in both x and y coordinates (e.g. Roache, 1976). As discussed earlier, the forward boundary condition is not needed. The important parameters are the magnitude of forcing, the boundary layer width $\delta$ [$\delta = (\varepsilon L_y/\alpha_0)^{1/2}$], and $\lambda$ given by (3.9). In the actual computation, we will fix $\delta$ and vary the shelf width, W, which is defined as the distance from the coast to the 200 m isobath. Solutions for longshore wind stress forcing and wind stress curl forcing are studied separately in order to isolate their influences. Because the equations are linear in the wind-driven cases, the general forcing problem in principle can be solved by adding the solutions for forcing at each coast section.

3.3.1 Longshore Wind Stress Forcing

Table 3.2 summarizes the numerical solutions under longshore wind stress forcing. The sea surface elevation in Case I is produced by a positive longshore stress over the portion of shelf from y = -2.5 to y = 0. The shelf is so wide that the coastal disturbances do not reach the shelf break. Figure 3.2 shows the distribution of sea surface elevation in this case. A parabolic boundary layer is present at the coast. The sea surface elevation decreases from y = 0 to y = -2.5. It then rises slowly in the region y < -2.5 The bottom velocity is not

Table 3.2

Summary of Numerical Solutions Under Longshore Wind Stress Forcing

| Nondimensional Quantities* | Case I | Case II | Case III |
|---|---|---|---|
| Shelf width, W, (100 km) | 1.6 | 0.85 | 0.85 |
| Water depth at the coast, $h_o$, (100 m) | 0 | 0.75 | 0 |
| Forcing range, $L_y$ (100 km) | 2.5 | 2.5 | 2.5 |
| Mean wind stress (1 dyne/cm$^2$) | 0.14 | 0.14 | 0.14 |
| $\delta/W$ | 0.2 | 0.4 | 0.4 |
| $\lambda$ | 0 | 2.1 | 0 |
| Maximum $\phi$ (1 cm) | -1.28 | -0.49 | -1.39 |
| Maximum $u_b$ (1 cm/sec) | -0.99 | -0.33 | -1.14 |
| Maximum $v_b$ (1 cm/sec) | 4.43 | 1.45 | 4.43 |
| Total transport ($10^5$ m$^3$/sec) | 0.35 | 0.36 | 0.36 |

* The dimensional scales are given in parenthesis.

shown, but it can be found easily from the gradient of sea surface elevation. Inside the forcing region, the offshore surface Ekman transport is compensated by a bottom geostrophic flow from the forward side of the forcing region. The strongest longshore flow occurs at the coast in the forcing region and migrates offshore in the region

$y < -2.5$. This longshore flow reaches a much longer distance than the wind stress itself. Although the strength of longshore velocity decreases on the shelf forward to the forcing region in the longshore direction, the total longshore transport across the shelf, calculated from the longshore velocity, is nearly constant in the region $y < -2.5$. In the case with a negative longshore stress, the flow behavior should be the same but the direction of flow is reversed.

The effect of a finite coastal bottom depth is examined in Case II, where a coastal wall is placed at $x = 0.75$. It is shown in Figure 3.3 that the surface elevation in the region $x > 0.75$ is similar to that with zero depth at the coast, except that the coastal wall cuts off the flow shoreward of it. In Case III, the longshore wind stress acts on a shelf where the boundary layer reaches the shelf break. The contour plot of bottom pressure is shown in Figure 3.4. According to this plot, the sea surface elevation field is qualitatively similiar to that in Figure 3.2, but the steep slope topography now plays a role in limiting the flow on the shelf. Longshore flow is present at the shelf break because of the constraint of a steep continental slope. These qualitative behavior is generally in agreement with those discussed in Section 3.2.1.

Quantitative effects of a coastal wall and a steep continental slope under longshore wind stress forcing can be found in Table 3.2. Since the maximum sea level change occurs at the coast, a coastal wall effectively reduces the maximum responses of the sea surface elevation and the magnitude of longshore velocity. The effect of a steep continental slope is not significant for the flow driven by longshore wind stress. The

total longshore transport is not influenced by either a coastal wall or a steep continental slope.

3.3.2 Wind Stress Curl Forcing

Figure 3.5 shows the sea surface elevation under forcing by a positive wind stress curl over the portion of the shelf between $y = 0$ and $y = -2.5$ (Case IV). The shelf is wider than the coastal boundary layer. In the forcing region, the sea surface is depressed in the $-y$ direction by the curl of wind stress. Forward to the forcing region in the longshore direction, the sea surface remains nearly the same. A steep continental slope plays an important role under wind stress curl forcing. The change in sea surface elevation is greatly reduced over the slope. The associated bottom velocity field can be seen in Figures 3.6 and 3.7. In Figure 3.6, the onshore flow in $-2.5 < y < 0$ is clearly associated with the Sverdrup transport. Forward to the forcing region ($y < -2.5$) the cross-shelf flow is weak. Longshore bottom flow shows a positive maximum at the shelf break (Figure 3.7). This longshore flow persists to a great longshore distance forward to the forcing region. At the coast, a weak counter flow in the forcing region is present. The longshore transport is mainly contributed by the strong longshore flow over the outer shelf (Figure 3.8). The total longshore transport integrated across the shelf is found to remain constant in the region $y < -2.5$.

When the wind stress curl is positive, it produces an upward vertical velocity at the base of the surface Ekman layer. This vertical transport is supported by the interior geostrophic onshore transport outside the

horizontal boundary layers. As the shelf break is approached, the strong bottom slope prevents the onshore geostrophic velocity from becoming too large. The transport then comes from the bottom Ekman layer and a positive longshore flow is generated. For a negative wind stress curl, the pattern is the same but $\phi$ changes sign and the flow direction is reversed.

The effect of a coastal wall is studied in Case V. The sea surface elevation and the maximum onshore velocity are about half of those in Case IV, and the maximum longshore flow is only slightly reduced (Table 3.3). Over a narrow shelf (Case VI), the sea surface elevation, the onshore flow, and the longshore velocity are only slightly samller then the relative values in Case IV (Table 3.3).

The circulation driven by wind stress curl has characteristics different from those of a longshore wind stress driven flow. The latter is a boundary layer flow and is less influenced by the pressence of a steep slope. However, the velocity distribution under wind stress curl forcing is mainly determined by the bottom topography with strongest flow at the shelf break. The region of steep continental slope serves as a buffer zone to the wind-driven shelf circulation. The steep bottom slope not only reduces the flow response to forcing but also prevents the circulation on the shelf from leaking onto the continental slope. With the exception of the area close to the shelf break, the deeper part of the slope is quite free from the wind effect.

## 3.4 The Insulating Effect of a Steep Slope on a Western Boundary Current

### 3.4.1 Introduction

The analyses in the earlier sections show that the slope region is not affected significantly either by the flow on the shelf or by the wind forcing over the slope. However, deep ocean "baroclinic" and "barotropic" currents may drive the circulation over the continental slope, especially on the western side of the ocean. To understand fully

Table 3.3

Summary of Numerical Solutions Under Wind Stress Curl Forcing

| Nondimensional Quantities* | Case IV | Case V | Case VI |
|---|---|---|---|
| Shelf width, W, (100 km) | 1.6 | 0.85 | 0.85 |
| Water depth at the coast, $h_o$, (100 m) | 0 | 0.75 | 0 |
| Forcing range, $L_y$ (100 km) | 2.5 | 2.5 | 2.5 |
| Mean wind stress curl ($10^{-7}$ dyne/cm$^2$) | 0.4 | 0.4 | 0.4 |
| $\delta/W$ | 0.2 | 0.4 | 0.4 |
| $\lambda$ | 0 | 2 | 0 |
| Maximum $\phi$ (1 cm) | -1.45 | -0.646 | -1.08 |
| Maximum $u_b$ (1 cm/sec) | -0.96 | -0.45 | -0.74 |
| Maximum $v_b$ (1 cm/sec) | 1.70 | 1.54 | 1.66 |
| Total transport ($10^5$ m$^3$/sec) | 1.80 | 1.05 | 1.05 |

* The dimensional scales are given in parenthesis.

the shelf/deep-ocean interaction, it is necessary to solve a nonlinear general circulation problem on the western side of the ocean with considerations of stratification and large bottom topographic variations, which is at present out of the question. However, as far as the shelf circulation is concerned, the detailed structure of western boundary current is not of interest to us. Some parameterization of the deep ocean flow hopefully will provide a qualitative description of the deep ocean influence.

The chart of mean wind stress curl over the North Atlantic Ocean (Leetmaa and Bunker, 1978) shows a line of zero wind stress curl generally following the path of the Gulf Stream. The curl is positive north of this zero contour line and negative south of it. It is of the order $10^{-8}$ cm/sec$^2$. Simple barotropic ocean models (e.g. Stommel, 1948) predict an anticyclonic gyre in the south and a cyclonic one in the north. The flow is intensified at the western boundary with the strongest current at the latitude of maximum wind stress curl. This pattern is altered by the presence of bottom topography at the western side of the ocean.

Schulman and Niiler (1970) solved numerically the linear equations of wind-driven circulation in a homogeneous ocean with topography running in the north-south direction at the western boundary of the ocean. Linear bottom friction as that in Stommel's (1948) model was used. In their solutions, the western boundary current flowed along constant f/h contours, and deep ocean gyres were distorted southward at the western boundary. The northern gyre was the one which contributed to the

near-bottom flow on the continental slope and rise off the Middle Atlantic Bight. A longshore pressure gradient imposed by deep ocean circulation at the shelf break was shown in their results. They also inferred the asymptotic behavior of the flow on a very narrow continental slope. It was found that the long-isobath flow over the continental slope was proportional to the water depth.

Killworth (1973b) studied the linear equations governing the circulation of a homogeneous ocean with the presence of a much steeper continental slope at the western boundary than that in the Schulman and Niiler's (1970) model. It was argued that the lateral viscosity dominated the vertical viscosity in the bottom Ekman layer over the continental slope. This assumption lead to a bottom frictional coefficient proportional to the bottom slope. With the aid of boundary layer analysis, Killworth found that most of the linear western boundary current was located at the foot of the slope. The steep slope effectively isolated the shelf circulation from deep ocean flow. The conclusion drawn from his study is qualitatively different from that of Schulman and Niiler (1970).

Schulman and Niiler's (1970) model, though much simplified, is likely to give a qualitatively accurate description of the barotropic western boundary undercurrent below the main thermocline north of the Gulf Stream. Nevertheless, there is a possibility that the gentle bottom slope used in their numerical computation causes a pressure gradient from deep ocean circulation being imposed on the shelf. In their asymptotic limit of a narrow slope region, the flow decreases smoothly

with bottom depth from the slope/rise junction to the shelf break. This is true only when the slope is much narrower than the boundary layer thickness. However, the thickness of boundary layers is generally of the same order of magnitude as the width of the continental slope or less. The limiting case in Schulman and Niiler's (1970) analysis can not be applied to the realistic topogaphy. The insulating effect of Killworth's (1973b) model is probably overemphasized on the continental slope, because of the assumed dependence of frictional coefficient on the bottom slope. This assumption conflicts with the generally accepted linear or quadratic bottom friction laws.

Circulation with stratification and bottom topography in the western North Atlantic Ocean was solved numerically by Semtner and Mintz (1977). Since they used a basin size about one third of the actual width of the North Atlantic Ocean, a large wind stress (3 dynes/cm$^2$) was needed to reproduce the observed Gulf Stream transport. In their model, the shelf flow north of Cape Hatteras seemed to be influenced by the cyclonic deep ocean gyre to the north. Their result was used by Beardsley and Winant (1979) to support the idea of a deep ocean imposed pressure gradient at the shelf break.

Before a definite conclusion on the slope/deep-ocean interaction can be made, several points need be clarified. Although the choice of a larger wind stress by Semtner and Mintz (1977) is valid in the deep ocean region, the effect of wind stress forcing on the shelf circulation is overestimated. Also, the cooling/heating is stronger on the shelf and upper slope than in the deep ocean because of the shallower depth. It is

not clear whether the pressure gradient on the shelf is derived from the deep ocean circulation or simply due to the response to local forcing. Furthermore, in Semtner and Mintz's (1977) results, the shelf flow contains a thermohaline component, which is caused by the local density field. It seems that the pressure gradient on the shelf in their model is not necessarily forced by the deep ocean circulation.

In view of the controversial speculations on the effect of a slope, it is important to analyze the conditions under which the deep ocean may drive the mean shelf circulation. In the following section, a quantitative analytical approach valid for steep topography is developed. We will study the case in which the density variations associated with the "baroclinic" current do not reach the bottom of continental slope, e.g. in the Slope Water region north of Cape Hatteras in the western North Atlantic Ocean. This approach should place the problem in a clearer focus than the numerical model of Semtner and Mintz (1977) or the boundary layer analysis of Killworth (1973b). A simple Stommel-type deep ocean model (Stommel, 1948) is used to parameterize the deep ocean influence as a boundary forcing on the near-bottom flow over topographic variations. This parameterization of deep ocean influence, however, is likely to be valid independently of the deep ocean model used. The effect of near-bottom density variations will be studied in the next chapter.

3.4.2 Model of Slope/Deep-Ocean Interaction

Consider an ocean with topography, which is uniform in the north-south direction. The coordinate system is defined so that x points

to the east and y to the north. The basin extends from x = 0 to $x_e$ in the east-west direction and infinitely long in the y direction. The bottom depth is nearly constant with a mean depth $h_d$ over most of the ocean. Inside a narrow band at the western side of the ocean, a shelf/slope topography as shown in Figure 3.1 is present. It joins smoothly to the deep ocean bottom. Variations in bottom density along isobaths are neglected. We will keep the $\beta$ terms in Equation (3.2) and use a constant Coriolis parameter when it is not differentiated (f = 1, nondimensionally). The vorticity equation governing the motion is

$$\varepsilon \frac{\partial^2 \phi}{\partial x^2} + \alpha \frac{\partial \phi}{\partial y} + \beta h \frac{\partial \phi}{\partial x} = \tau_o F - \beta \sigma \int_{-h}^{0} z \frac{\partial \rho}{\partial x} dz \qquad (3.2')$$

where the bottom pressure perturbation, $\phi$, is related to the bottom geostrophic velocity by

$$u_b = - \frac{\partial \phi}{\partial y} \qquad (3.1a')$$

$$v_b = \frac{\partial \phi}{\partial x} \qquad (3.1b')$$

The terms on the left-hand side of (3.2') represent curl of bottom stress, vertex stretching, and $\beta$ times the transport associated with the bottom geostrophic velocity. On the right-hand side of (3.2'), the terms are wind stress curl and $-\beta$ times the thermohaline transport definded by Equation (2.15). Under the assumption of vanishing long-isobath bottom density variations, only if $\beta$ is non-vanishing, can the bottom flow be

driven by the density field. On the continental shelf, the β terms are small because of shallow water depth. The local forcing is mainly caused by wind. In the lower slope and deep ocean regions, the β terms can be important.

In the region $x_d \leq x \leq x_e$, where the bottom depth variation is small, the vorticity tendency balance in (3.2') is reduced to

$$\varepsilon \frac{\partial^2 \phi}{\partial x^2} + \beta h_d \frac{\partial \phi}{\partial x} = \tau_0 F - \beta \sigma \int_{-h}^{0} z \frac{\partial \rho}{\partial x} dz \qquad x \geq x_d \qquad (3.17)$$

Outside the western boundary layer, the bottom friction term is negligible. Equation (3.17) expresses a Sverdrup relation, in which the transports of bottom geostrophic velocity and thermohaline velocity are balanced by the curl of wind stress. The first term on the left-hand side of (3.17) is important only inside the western boundary layer. At the eastern boundary of the ocean ($x = x_e$) the condition $\phi = 0$ must be satisfied. We will integrate (3.17) from $x_d$ to $x_e$. The integration leads to:

$$\delta_d \frac{\partial \phi}{\partial x} + \phi = -\frac{1}{\beta h_d} \int_{x_d}^{x_e} \tau_0 F \, dx + \frac{\sigma}{h_d} \int_{x_d}^{x_e} dx \int_{-h}^{0} z \frac{\partial \rho}{\partial x} dz = \phi_0 \qquad (3.18)$$

where $\delta_d = \varepsilon/(\beta h_d)$ is the width of Stommel's (1948) western boundary layer in a flat bottom ocean. $-h_d \phi_0$ is the "barotropic" transport integrated across the latitude circle, or the difference between the total Sverdrup transport produced by the wind stress curl and the thermohaline transport. The latter occurs mainly above the main thermocline. If the

bottom pressure at the eastern boundary is zero, $\phi_o$ may also be interpreted as the bottom pressure distribution at $x = x_d$. The solution for $x \leq x_d$ must satisfy (3.18) at $x = x_d$ through the continuity of $\phi$ and $\partial\phi/\partial x$. The boundary condition for the flow on the slope becomes

$$\delta_d \frac{\partial \phi}{\partial x} + \phi = \phi_o \qquad \text{at } x = x_d \qquad (3.19)$$

and the deep ocean circulation is decoupled from the problem. The validity of (3.19) does not depend on the exact location of $x_d$, once $x_d$ is outside the region of large topographic variations. Also, it does not depend on the particular model used for deep ocean flow, since only $\phi_o$ and the parameter $\delta_d$ are involved.

In the region $x \leq x_d$, we neglect the wind stress curl forcing in order to isolate the influence from deep ocean. Equation (3.2) becomes

$$\varepsilon \frac{\partial^2 \phi}{\partial x^2} + \alpha \frac{\partial \phi}{\partial y} + \beta h \frac{\partial \phi}{\partial x} = -\beta \sigma \int_{-h}^{0} z \frac{\partial \rho}{\partial x} dz \qquad (3.20)$$

The boundary condition at the coast with $h_o = 0$ is

$$\varepsilon \frac{\partial \phi}{\partial x} = 0 \qquad \text{at } x = 0 \qquad (3.21)$$

The initial condition

$$\phi = 0 \qquad \text{at } y=0 \qquad (3.22)$$

may be specified, if the deep ocean pressure field vanishes at $y \geq 0$. Equations (3.19) to (3.22) can be solved by assuming a bottom pressure distribution $\phi_0$ at $x = x_d$ and a density distribution in the region $x < x_d$. Two driving forces are present in this formulation: $\phi_0$, which is a parameterization of the deep ocean effect; and an interior forcing term in (3.20) caused by local thermohaline flow.

3.4.3 Flow Driven by a Longshore Thermohaline Current over the Slope

It has been shown in Section 3.2.2 that the pressure field set up by forcing in the slope region will appear as a longshore pressure distribution at the shelf break. Letting $\phi_0 = 0$, we may examine the effect of a thermohaline current on the pressure field over the slope. The flow behavior is the same as that under wind stress curl forcing. We will examine the response of the flow in the interior region of the slope away from boundary layers.

From (3.20), the interior vorticity tendency balance becomes

$$\alpha \frac{\partial \phi}{\partial y} = -\beta \sigma \int_{-h}^{0} z \frac{\partial \rho}{\partial x} dz = -\beta V_c$$

In dimensional form, the long-isobath pressure gradient is

$$\frac{\partial \phi^*}{\partial y^*} = -\frac{\beta^* V_c^*}{\alpha^* g}$$

For a mean current of the order 10 cm/sec extending to 100 m depth, the longshore sea surface gradient over a bottom slope of $10^{-2}$ is $10^{-9}$. With such a longshore gradient imposed at the shelf break,

Csanady's (1978) model gives a longshore bottom flow of 0.2 cm/sec, which is too small to have significant contribution to the mean flow. Only when the Gulf Stream meanders onto the slope region with a mean thermohaline velocity of 10 cm/sec extending to 500 m, can a bottom velocity of 1 cm/sec be produced on the shelf.

3.4.4 Forcing from Deep Ocean Currents

In this section, the right-hand side of (3.20) is set to be zero to study the effect of deep ocean currents. The forcing on the flow in the slope region comes from the boundary condition (3.19). Let $\alpha_o$ be the typical nondimensional slope and $L_y$ the longshore dimension of deep ocean gyre. A topographic boundary layer is present over the continental slope with width $\delta = (\varepsilon L_y/\alpha_o)^{1/2}$ as discussed in Section 3.2. Using the variables $\xi = (x_d - x)/\delta$ and $\eta = -y/L_y$, (3.20) leads to

$$\frac{\partial^2\phi}{\partial\xi^2} - \frac{\alpha}{\alpha_o}\frac{\partial\phi}{\partial\eta} - \frac{\delta}{\delta_d}\left(\frac{h}{h_d}\right)\frac{\partial\phi}{\partial\xi} = 0 \qquad 0 \le x \le x_d \qquad (3.23)$$

The boundary condition (3.19) becomes

$$\frac{\delta_d}{\delta}\frac{\partial\phi}{\partial\eta} + \phi = \phi_o \qquad \text{at } x = x_d \qquad (3.24)$$

If $\delta_d/\delta \gg 1$, the dominant balance in (3.24) is

$$\frac{\delta_d}{\delta}\frac{\partial\phi}{\partial\eta} = \phi_o \qquad \text{at } x = x_d \qquad (3.25)$$

and $\phi$ is of the order $\delta/\delta_d \ll 1$ in the region $x \le x_d$. In this case,

only a small portion of the deep ocean bottom pressure field will reach the region of large topographic variations. Therefore, even the boundary layer is of the width of the slope, the sea surface elevation at the shelf break is still $\delta/\delta_d$ times smaller than the deep ocean value. To the deep ocean flow, it is equivalent to have $\phi = 0$ condition at the western boundary and a strong western boundary current is present as in Stommel's (1948) model. For a gentle topography $\delta/\delta_d >> 1$, (3.24) becomes $\phi = \phi_o$, and the deep ocean bottom pressure distribution extends entirely over the slope as if no boundary were present between them.

To estimate the magnitude of $\phi_o$, we need to know the total Sverdrup transport and the thermohaline transport in the ocean. The uncertainty in the wind stress curl calculation prohibits an accurate estimation of the Sverdrup transport. Leetmaa et al. (1977) compared the transport calculated from the wind stress curl with the thermohaline transport. They found these two values were equal in the southern gyre within an uncertainty of $\pm$ 10 Sverdrup in the deep water between 1000 and 3000 decibars. Using 10 Sverdrup as the upper limit for the barotropic transport in the northern gyre between 1000 and 3000 decibars, the barotropic transport will produce a sea surface rise of 5 cm across the basin along a latitude circle. With a north-south scale of 1000 km in wind stress, the sea surface gradient is $5 \times 10^{-8}$ outside the western boundary layer. If the width of the long-isobath flow on the continental rise and slope off Cape Code observed by Luyten (1977) and Schmitz (1974) is used as the width of western boundary layer, $\delta_d$ will be about 100 km. For $\varepsilon = 0.05$, $L_y = 10$ and $\alpha_o = 50$, which correspond to a longshore

scale of 1000 km in the y direction and a bottom slope of $5 \times 10^{-2}$, we have $\delta \simeq 0.1$ or 10 km dimensionally. The sea surface gradient over the slope is at most $5 \times 10^{-9}$. Even if this gradient is totally imposed onto the shelf break, it is unable to make a significant contribution to the shelf circulation.

Equations (3.19) to (3.22) have been solved numerically using the topography shown in Figure 3.1. A longshore forcing range of 1000 km is used. The parameters $\epsilon$ and $\beta$ are 0.05 and 0.01 respectively. Figure 3.9 is a map of the bottom pressure distribution. The long-isobath velocity is shown in Figure 3.10. Obviously, a realistic continental slope effectively prevents the deep ocean circulation from influencing the near-bottom flow on the shelf. This illustrates in detail the conclusion already reached in Section 3.2 from a general analysis of the vorticity tendency balance.

3.5 Applications of the Slope Model

The characteristics of the mean circulation on the continental slope may be used to interpret some geochemical observations. Biscaye et al. (1978) studied the near-bottom distribution of suspended particles and excess radon-222 on the continental shelf and slope off New York Bight. They found that the concentration of suspended particles generally showed a seaward decrease across the shelf. However, beyond the shelf break, there was a zone aproximately parallel to the isobaths, in which the concentration of suspended particles went through a minimum and rose again in the deep water. The center of this minimum concentration of suspended particles was somewhere betweem the 1500 m and the 2000 m

isobaths. The distribution of near-bottom excess radon was similar to that of suspended particles. It also showed a zone of minimum concentration which coincided with that of suspended particles. Biscaye et al. (1978) found that the zone of minimum concentration of near-bottom excess radon and suspended particles was not correlated with either the bottom sediment distribution or the concentration in the surface layer. Two uncompatible explanations were suggested by them. One was that the near-bottom water over the slope was so quiescent that the excess radon, being produced within the sediments and diffused across the sediment-water interface, was not mixed vertically more than a meter or so above the bottom. The other explanation was that the near-bottom flow over the slope was so active that the water mixed with the mid-depth water from the ocean interior, which would be low in suspended particles and contain no excess radon. Such mixing had to be strong enough to dilute the flux of excess radon from the sediment, however, the mixing should not stir up the bottom sediments.

The model solutions in this chapter readily give an explanation to the distributions of suspended particles and excess radon. We have shown that the slope region is not disturbed by either the wind from the surface or the circulation on the shelf. The deep ocean circulation is also prevented from reaching the slope region. This argument is applicable to low frequency flow. In the higher frequency band, near-bottom current measurements of Luyten (1977) and Schmitz (1974) showed that there was no increase in kinetic energy form the continental rise to the slope region. It is unlikely that there is any mechanism

which will increase the near-bottom mixing on the slope. It may be concluded that the upper shelf region below the thermocline is so quiescent that the excess radon produced in the sediments is not mixed into the water column and no disturbing mechanism is avaliable to resuspend the bottom sediment as observed by Biscaye et al. (1978).

## 3.6 Summary

In this chapter, we have discussed the model responses of the flow on the continental shelf and slope under forcing by longshore wind stress, wind stress curl, and deep ocean currents. The flow driven by the longshore wind stress is mainly inside a coastal boundary layer as in Csanady's (1978) model. Outside this boundary layer, the flow is driven by the curl of wind stress. This flow is strongly influenced by the bottom topography. The continental slope has two effects: it reduces the flow response to wind stress curl forcing over the steep slope, and it prevents both the deep ocean circulation and the shelf circulation from leaking onto the slope. An examination of the influences of thermohaline flow over the slope and the near-bottom deep ocean circulation show that, without the forcing caused by long-isobath bottom density variations, these two sources are unable to contribute significantly to the flow on the upper slope below the thermocline. The model results reveal that, except for a possible deep ocean imposed thermohaline velocity component, the upper slope below the thermocline is quiescent. These results can be used to explain some geochemical observations on the continental shelf also.

Figure 3.1 Bottom profile used in numerical computations. The distance and the depth are scaled by 100 km and 100 m respectively. The shelf shown is a "wide" shelf.

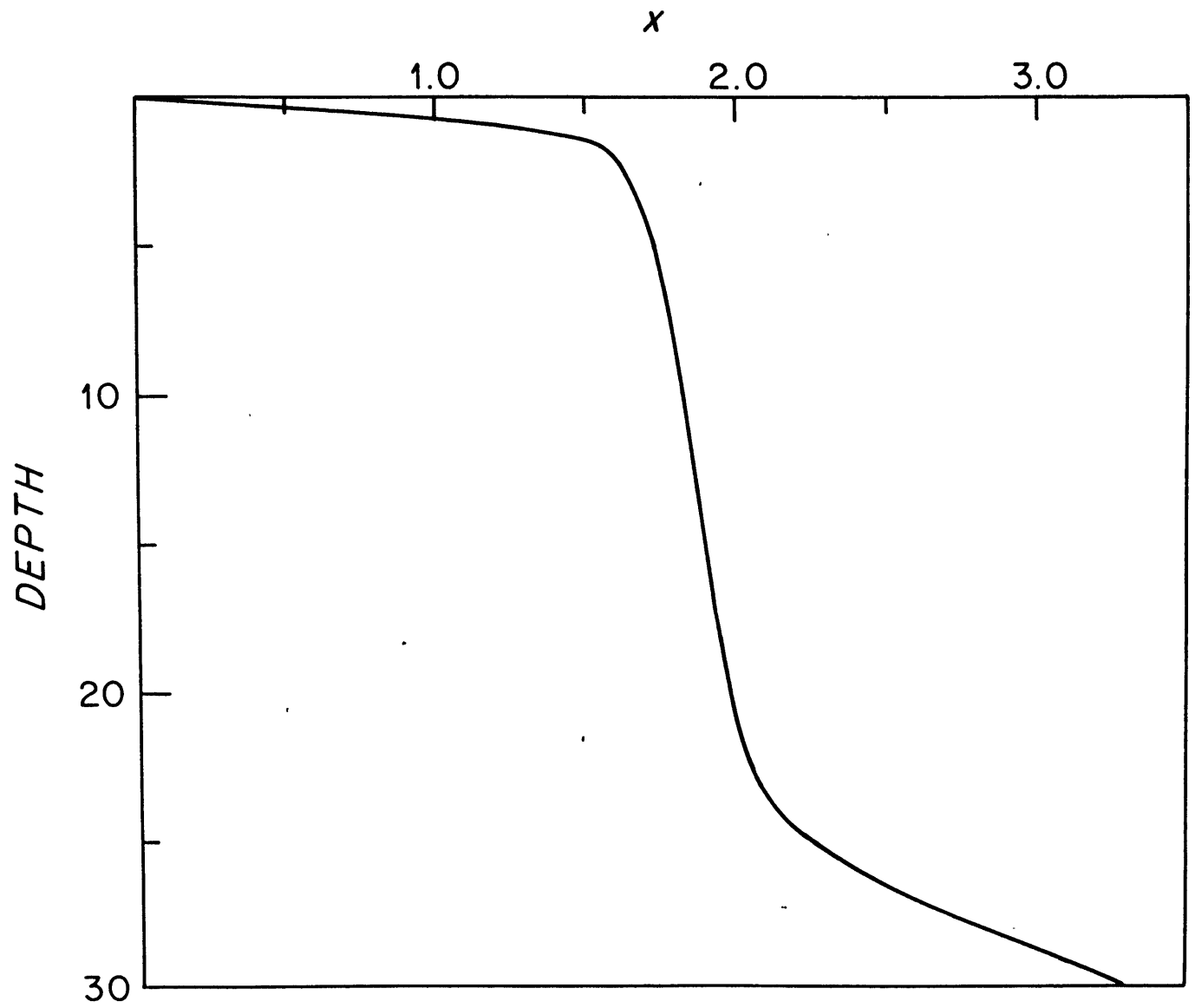

x
1.0
2.0
3.0
DEPTH
10
20
30

Figure 3.2 Distribution of bottom pressure $\phi$ over a "wide" shelf, forced by a positive longshore stress from $y = -2.5$ to $y = 0$ (Case I). The nondimensional contour interval is 0.1.

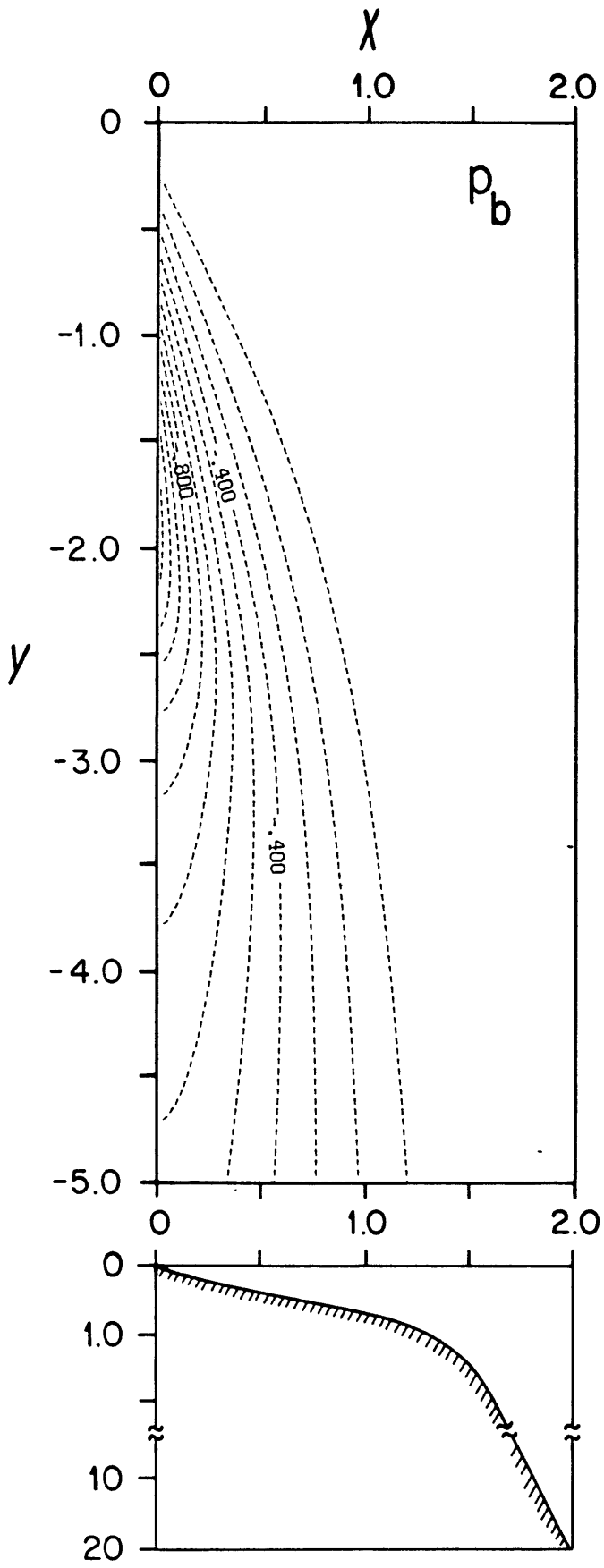

x
0
1.0
2.0
0
-1.0
-2.0
-3.0
-4.0
-5.0
y
$p_b$
800
400
400
0
1.0
2.0
0
1.0
10
20

Figure 3.3 Distribution of bottom pressure $\phi$ forced by a positive longshore stress from y = -2.5 to y = 0 with a coastal wall placed at x = 0.75 (Case II). The nondimensional contour interval is 0.1.

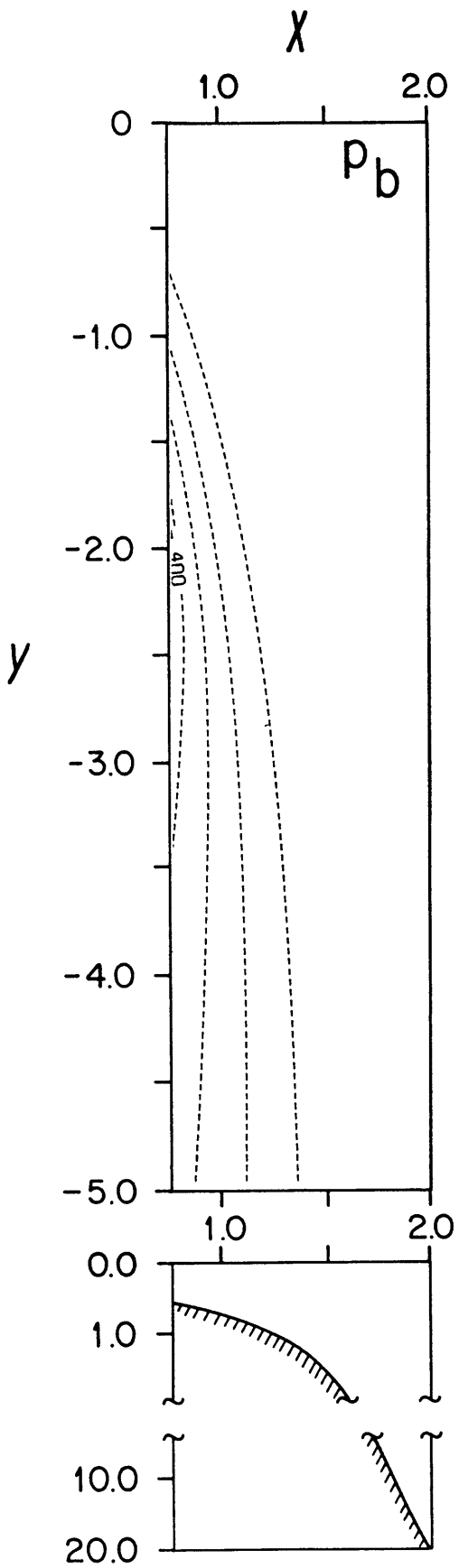

X
1.0
2.0
0
$p_b$
-1.0
-2.0
400
y
-3.0
-4.0
-5.0
1.0
2.0
0.0
1.0
10.0
20.0

Figure 3.4 Distribution of bottom pressure $\phi$ over a "narrow" shelf, forced by a positive longshore stress from $y = -2.5$ to $y = 0$ (Case III). The nondimensional contour interval is 0.1.

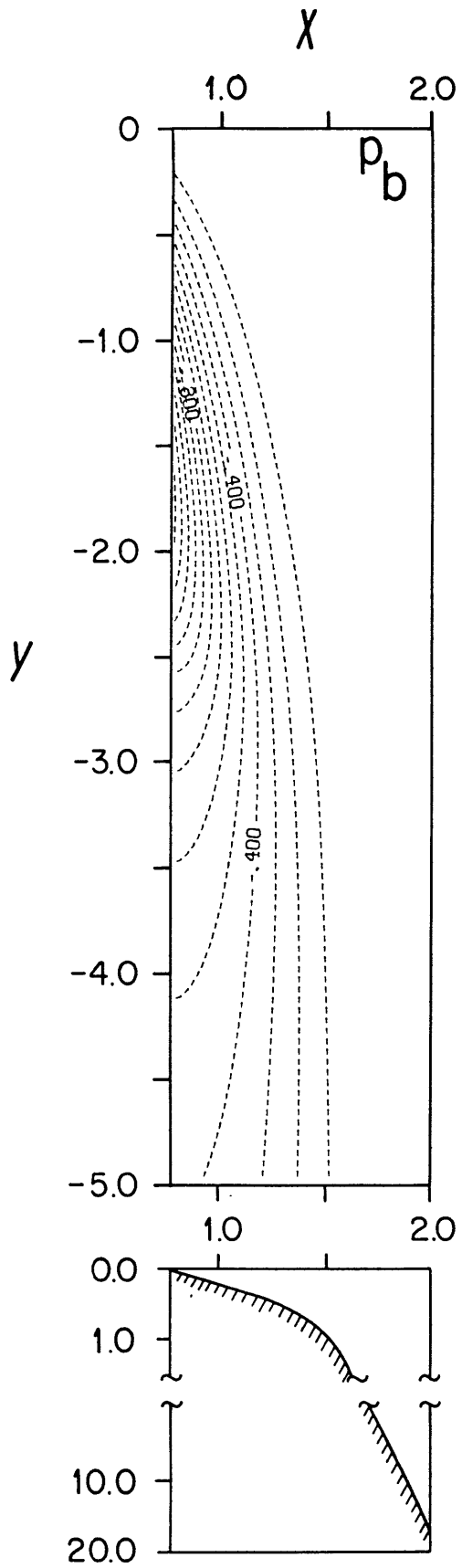

X
1.0
2.0
0
$p_b$
-1.0
-2.0
-3.0
-4.0
-5.0
y
300
400
400
1.0
2.0
0.0
1.0
10.0
20.0

Figure 3.5 Distribution of bottom pressure $\phi$ forced by a positive wind stress curl from y = -2.5 to y = 0, which is uniform in x (Case IV). The nondimensional contour interval is 0.1.

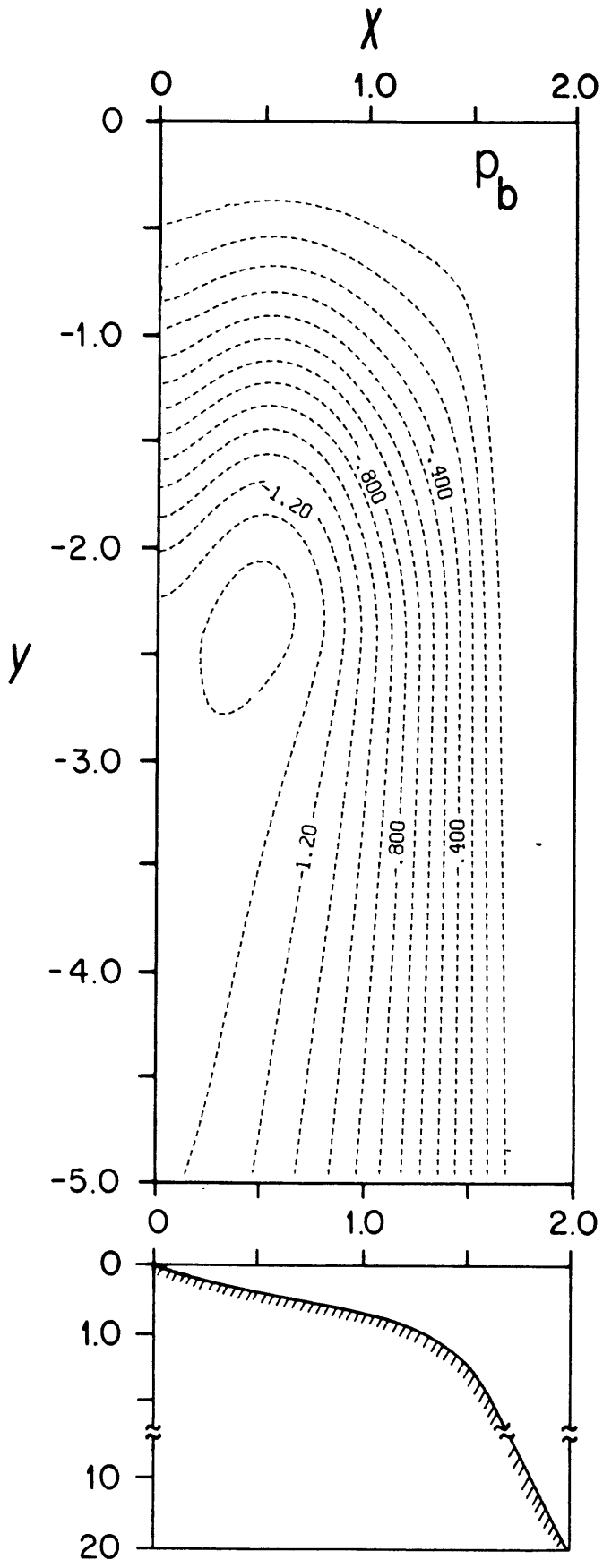

X
0
1.0
2.0
0
-1.0
-2.0
-3.0
-4.0
-5.0
y
$p_b$
-1.20
-800
-400
0
1.0
2.0
0
1.0
10
20

Figure 3.6 x-component bottom geostrophic velocity distribution calculated from the bottom pressure field in Figure 3.5. Dashed lines represent negative values.

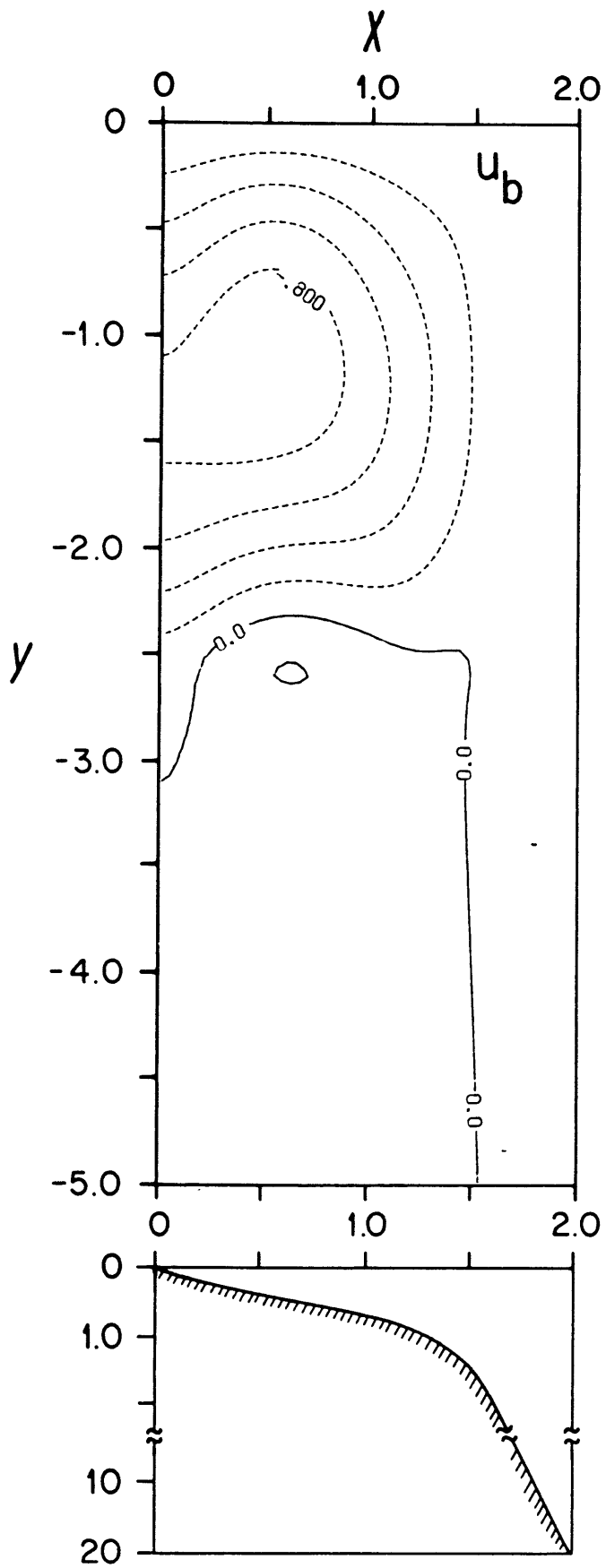

X
0
1.0
2.0
0
-1.0
-2.0
-3.0
-4.0
-5.0
y
$u_b$
.800
0.0
0.0
0.0
0
1.0
10
20

Figure 3.7 y-component bottom geostrophic velocity distribution calculated from the bottom pressure field in Figure 3.5. Dashed lines represent negative values.

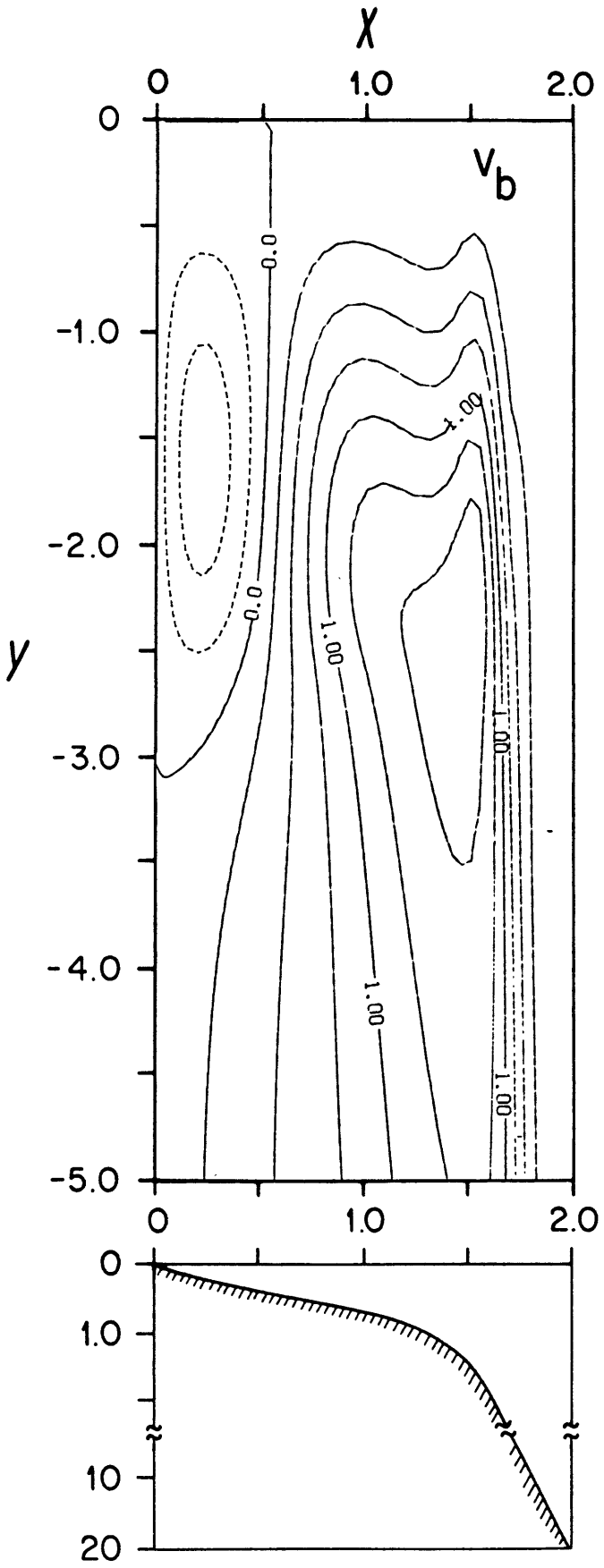

X
0
1.0
2.0
0
$V_b$
-1.0
-2.0
-3.0
-4.0
-5.0
y
0.0
0.0
1.00
1.00
1.00
1.00
1.00
0
1.0
10
20

Figure 3.8 Transport of longshore bottom velocity shown in Figure 3.7.

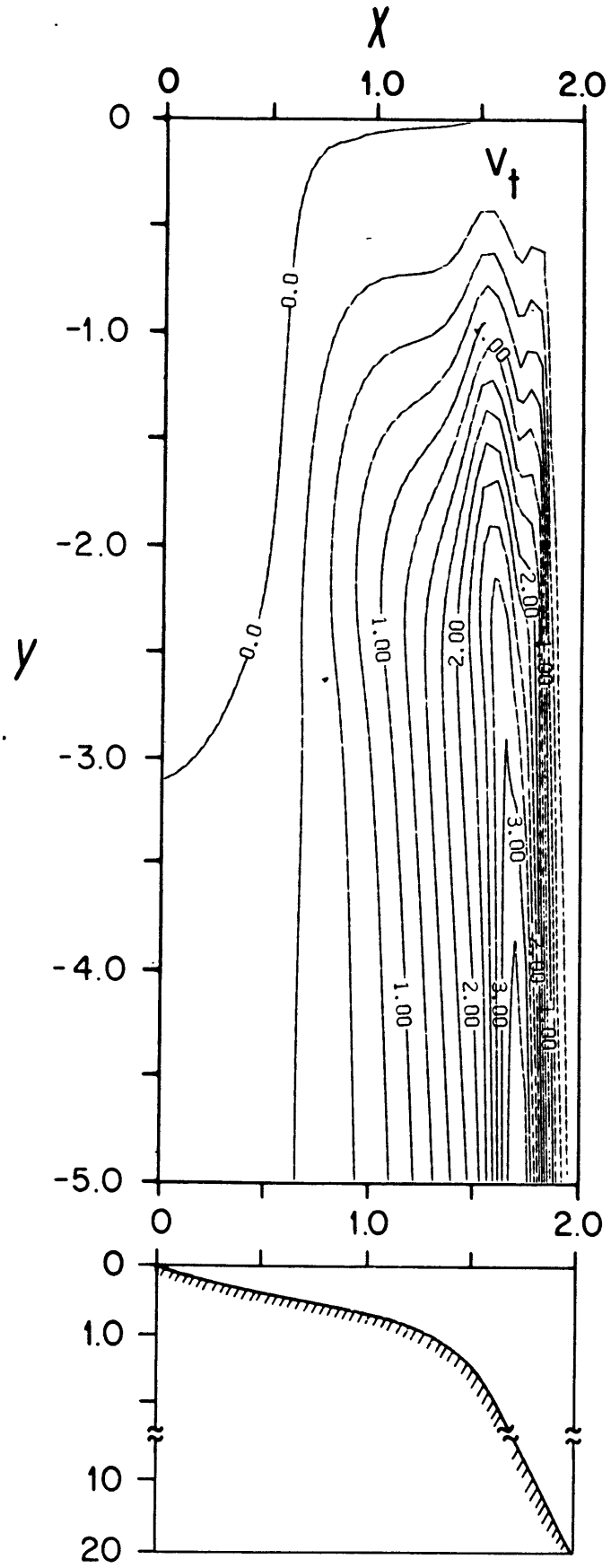

X
0
1.0
2.0
0
-1.0
-2.0
-3.0
-4.0
-5.0
y
$V_t$
0.0
0.0
1.00
1.00
2.00
2.00
3.00
3.00
0
1.0
10
20

Figure 3.9 Bottom pressure field produced by deep ocean forcing with $\epsilon = 0.05$ and $\beta = 0.01$.

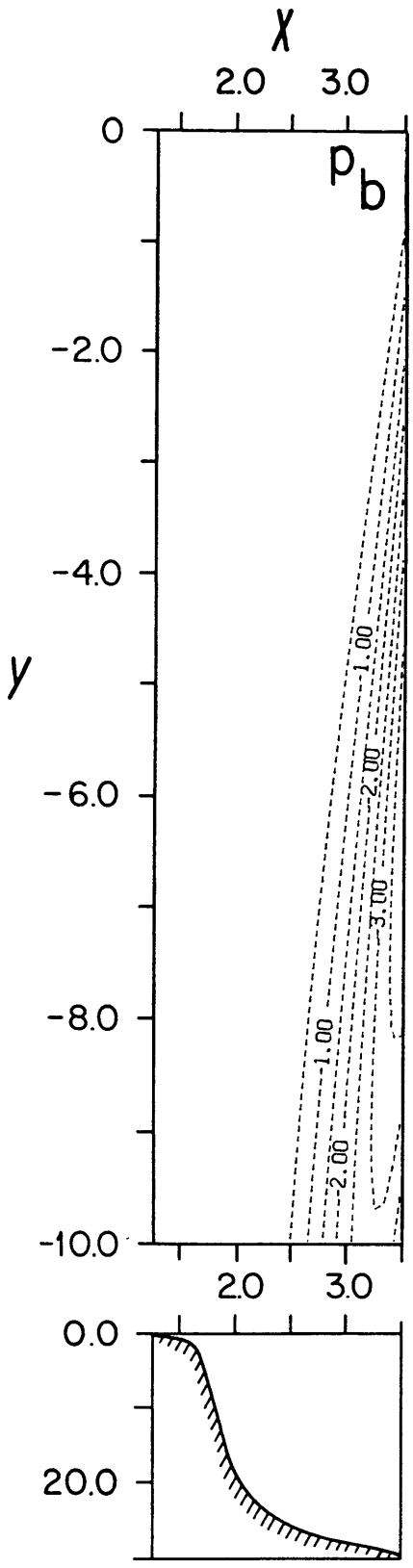
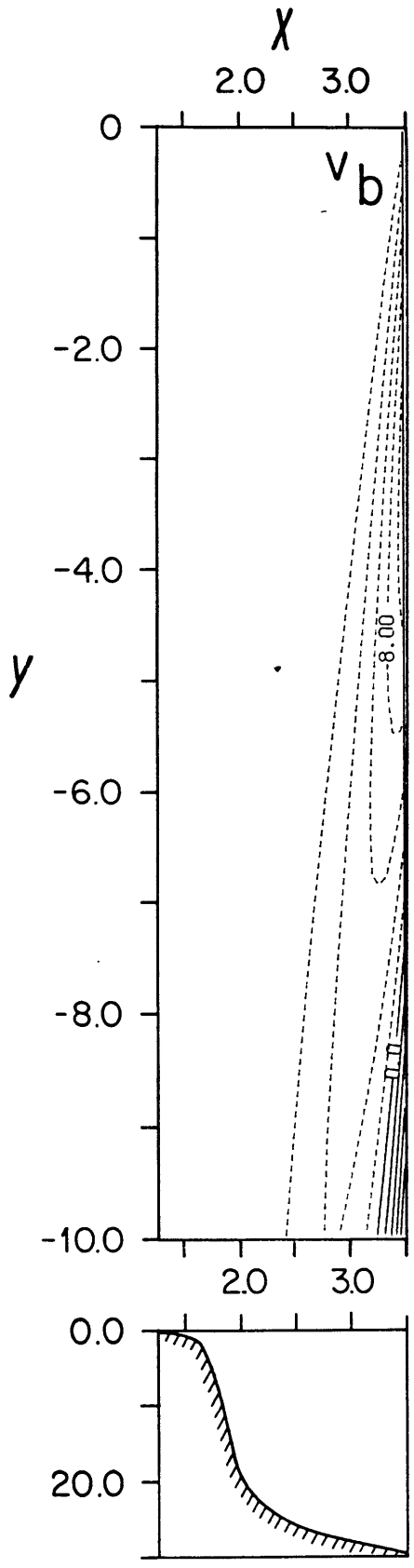

X
2.0
3.0
0
$p_b$
-2.0
-4.0
y
-6.0
-8.0
-10.0
1.00
2.00
3.00
1.00
2.00
2.0
3.0
0.0
20.0

Figure 3.10 Long-isobath bottom velocity calculated from the pressure field in Figure 3.9.


X
2.0
3.0
0
$v_b$
-2.0
-4.0
y
-8.00
-6.0
-8.0
-10.0
2.0
3.0
0.0
20.0

# CHAPTER 4

# DENSITY-DRIVEN FLOW AND THE DISPERSION OF DENSITY PERTURBATIONS

## 4.1 Introduction

In a rotating homogeneous fluid the vorticity constraint of bottom topography effectively prevents cross-isobath geostrophic flow. If the bottom density field varies only in the cross-isobath direction, one particular solution of Equations (2.18) and (2.19) is the zero bottom geostrophic velocity. The result is thermohaline circulation with geostrophic velocity calculated with the bottom on the reference level. In this situation the vorticity is not affected by topographic variations. However, when a bottom density gradient exists along isobaths, simple sea level adjustment to the density field is not possible. The geostrophic velocity relative to the bottom, calculated from the density field, becomes divergent. This divergence leads to vorticity changes and the generation of long-isobath bottom flow.

There are several places in the world ocean, where surface cooling or evaporation is so strong that the water column becomes unstable and dense water is formed by this atmospheric effect, e.g. in the Antarctic Continent, the Norwegian Sea, and the Mediterranean Sea. Dense water is also found in the outflow waters from these regions (see Warren, 1981, for a review). Furthermore, the dense water may reach the ocean bottom in areas with shallow water depths, and a dynamic interaction between long-isobath density variations and bottom topography may take place. The most prominent example is the production of dense saline Antarctic

Bottom Water on the Antarctic continental shelves by the salt release during ice formation (Gill, 1973). Over mid-latitude shelves, the dense water caused by winter cooling may reach the bottom also. Examples can be found in the northern Adriatic Sea (Hendershott and Rizzoli, 1976), the Middle Atlantic Bight (Bigelow, 1933), and the Gulf of Maine, where the Gulf of Maine Intermediate Water is formed (Brown and Beardsley, 1978). Another source of possible interaction between density and topography is the river efflux under weakly stratified conditions. Unlike the case in which dense water sinks to the bottom, the light water remains on the bottom because of the mixing under atmospheric cooling and tidal action near the coast.

The mere long-isobath bottom flow generation process is not the whole story. Observations show that the Gulf of Maine Intermediate Water reaches the New England shelf in summer (Hopkins and Garfield, 1979). The Antarctic Bottom Water also flows along the Weddell Sea shelf break westward to the northern tip of the Antarctic Peninsula (Forster and Carmack, 1976). Apparently, bottom flow advects the density field, and the resulting density structure, in turn, produces new long-isobath bottom flow. The dynamics of this "self-advective" interaction can be understood only if both density advection and topography are taken into account. However, this leads to a very complex problem.

Numerous attemps have been made to model the mean shelf circulation including density effects. The complexity of the problem has necessitated various simplifications. Basically, there are three categories of model assumptions. In the first category, bottom

topography is neglected, e.g. Stommel and Leetmaa's (1972) model on the eastern North American shelf and Killworth's (1974) model on the Antarctic shelves. The second category models take into account both topography and stratification but not the effect of density advection. The model of Pedlosky (1974) belongs to this one, as do many "diagnostic" numerical models. The major shortcoming of these models is the neglect of the important dynamics of density advection which causes the density perturbation to propagate away from the source region. Hendershott and Rizzoli (1976) included all the essential dynamic factors in their numerical calculations. Their model belongs to the third category, in which stratification, topography, and density advection are all considered. In this chapter, the dynamics of density-driven flow is further investigated both analytically and numerically using simple models of the third category.

We will apply the equations derived in Chapter 2 to the general problem of interaction between steep bottom slope and density variations caused by both surface density flux and buoyancy sources at the coast. The evolution of the flow driven by horizontal density differences will be predicted by the model. The case to be studied is when the horizontal density variations reach the bottom and the constant density lines at the bottom do not coincide with isobaths. If surface heating or river discharge merely produces a uniform layer of light water at the surface, the density field will have no dynamic significance to the bottom flow. So is the case when the bottom density is constant along isobaths. These two situations have been discussed earlier in Chapter 3.

## 4.2 Formulation of the Problem

### 4.2.1 The Velocity Field

We consider the density-driven flow on a shelf with a long and straight coast, where bottom depth depends on the offshore coordinate only. The coordinate system is the same as that in Figure 2.1. For density-driven flow, the velocity scale is chosen according to the density variations so that $\sigma$ is unit and $\tau_0$ is zero. The $\beta$-effect is neglected and the nondimensional Coriolis parameter f is +1 or -1 depending on the hemisphere where the shelf is located. Therefore, 1/f determines the direction of the time-like coordinate in the heat conduction analogy. The governing equations (2.18) and (2.19) become

$$\frac{\partial u_b}{\partial x} + \frac{\partial v_b}{\partial y} = -\frac{\alpha}{f}\frac{\partial \rho_b}{\partial y} \tag{4.1a}$$

$$\varepsilon \frac{\partial v_b}{\partial x} - f\alpha u_b = 0 \tag{4.1b}$$

where $\alpha$ is the bottom slope in nondimensional coordinates.

When the long-isobath bottom density variations are not negligible, (4.1a) shows that the bottom velocity becomes divergent and a stream function can not be defined. However, it is possible to decompose the bottom velocity into one divergent component $v_d$ and two nondivergent ones, $v_e$ and $u_e$:

$$v_b = v_d + v_e \tag{4.2a}$$

$$u_b = u_e \tag{4.2b}$$

and $v_d$ is defined by

$$\frac{\partial v_d}{\partial y} = -\frac{\alpha}{f}\frac{\partial \rho_b}{\partial y}$$

Over an infinitively long shelf with horizontal isopycnals in the undisturbed region, $v_d$ can be chosen as

$$v_d = -\frac{\alpha}{f}[\rho_b - \bar{\rho}_b(x)] = -\frac{\alpha}{f}\rho' \tag{4.3}$$

where $\bar{\rho}_b(x)$ is the bottom density at infinity. $v_d$ then vanishes at infinity with localized disturbances. For simplicity, we will consider $\bar{\rho}_b(x)$ to be identically zero. This situation occurs on the shelf when a homogeneous bottom layer is present below the seasonal thermocline. The nondivergent velocities are expressed by a stream function $\phi$,

$$u_e = -\frac{\partial \phi}{\partial y} \tag{4.4a}$$

$$v_e = \frac{\partial \phi}{\partial x} \tag{4.4b}$$

With application of (4.2) to (4.4), (4.1b) may be rewritten as

$$\varepsilon \frac{\partial^2 \phi}{\partial x^2} + f\alpha \frac{\partial \phi}{\partial y} = \frac{\varepsilon}{f} \frac{\partial}{\partial x}(\alpha \rho') \tag{4.5}$$

4.2.2 Case of Vertically Homogeneous Water Column

We will model the winter condition on the continental shelf, when the water column is nearly vertically homogeneous. Using (4.3) and (4.4), Equation (2.40) can be expressed in terms of $v_d$, $\phi$, and $\rho'$. We have

$$\frac{\partial \rho'}{\partial t} + u_a \frac{\partial \rho'}{\partial x} + v_a \frac{\partial \rho'}{\partial y} = \frac{\gamma}{h} \frac{\partial}{\partial x}\left(h \frac{\partial \rho'}{\partial x}\right) + \gamma \frac{\partial^2 \rho'}{\partial y^2} + Q_0 \frac{Q}{h} \tag{4.6}$$

where

$$u_a = -\frac{\partial \phi}{\partial y} - \frac{\varepsilon}{h}\left(\frac{\partial \phi}{\partial x} + v_d\right)$$

and

$$v_a = \left(\frac{\partial \phi}{\partial x} + v_d\right) - \frac{\varepsilon}{h}\frac{\partial \phi}{\partial y}$$

are the sum of the bottom geostrophic velocity and the depth-averaged bottom frictional velocity. To avoid the singularity at h = 0, we apply a coastal wall of depth $h_0$ at x = a. The coastal boundary conditions from (2.20) and (2.38) become

$$\varepsilon \frac{\partial \phi}{\partial x} + f h_0 \frac{\partial \phi}{\partial y} = \frac{\varepsilon \alpha}{f} \rho' + \frac{h^2}{2} \frac{\partial \rho'}{\partial y} \qquad \text{at } x = a \tag{4.7a}$$

and

$$\gamma h_0 \frac{\partial \rho'}{\partial x} = R_0 R \qquad \text{at } x = a \tag{4.7b}$$

where $R_0 = \tilde{R}/(\varepsilon_R f_0 \tilde{H} \tilde{L} \Delta\tilde{\rho})$ and R is the nondimensional buoyancy flux. We assume that the density disturbance is limited in space so that the

other boundary conditions are

$$\phi = 0; \quad v_b = 0; \quad \text{and } \rho' = 0 \qquad \text{at } x \to \infty \text{ and } y \to \pm\infty \qquad (4.8)$$

Equations (4.5) and (4.6), with the boundary conditions (4.7) and (4.8), may be used to model the flow driven by surface density flux or a river buoyancy source.

In the mid-shelf region over a wide shelf, the velocity and density fields are not affected by boundary layers. Initially, the horizontal density field has the same length scale as that of the surface density flux, which is of the order of hundreds of kilometers. We scale the density field according to the size of atmospheric disturbances. For an order one longshore density perturbation and an order one bottom slope, $v_d$ being given by (4.3) is also of order one. From (4.5), the stream function $\phi$ of the nondivergent velocity is of the order $\varepsilon$ in the interior region, and the flow is dominated by the direct density-driven component $v_d$. For $\gamma << 1$, the order one interior balance in the density equation (4.6) is between the time dependent term and the longshore advection term. The leading order balance in (4.6) is

$$\frac{\partial \rho'}{\partial t} - \frac{\alpha}{f} \rho' \frac{\partial \rho'}{\partial y} = 0 \qquad (4.9)$$

where (4.3) has been used for $v_d$. Equation (4.9) is a nonlinear first order partial differential equation, which is the same equation governing the shock wave propagation (e.g. Whitham, 1974). The density

diffusion in the y direction is important in the shock region. Therefore, we will retain the y-diffusion term and write the governing equation away from coastal and shelf edge boundary layers as

$$\frac{\partial \rho'}{\partial t} - \frac{\alpha}{f} \rho' \frac{\partial \rho'}{\partial y} = \gamma \frac{\partial^2 \rho'}{\partial y^2} \tag{4.10}$$

which is Burgers' equation after a coordinate transformation (Whitham, 1974). Equation (4.10) will be discussed in detail in the next section.

In the vorticity equation (4.5), the same topographic boundary layers of Section 3.2 exist near the coast and at the shelf break. Strong density gradients are also present at both the shelf break and the coast. We will call these regions of strong density gradient "density boundary layers" to distinguish them from the topographic boundary layers of the bottom pressure field. The near-shore flow is complicated by both topographic and density boundary layers. When the density field at the coast varies in the longshore direction and the coastal depth is finite ($h_0 \neq 0$), there is a thermohaline transport normal to the coast. A topographic boundary layer is needed to satisfy the no normal flow condition (4.7a). Letting the longshore length scale of the density variation be $L_y$ over a shelf of constant slope $\alpha_0$, the topographic boundary layer is of the width $\delta = (\epsilon L_y/\alpha_0)^{1/2}$. Expressing (4.5) in terms of topographic boundary layer variables $\xi = x/\delta$ and $\eta = -y/L_y$, we have

$$\frac{\partial^2 \phi}{\partial \xi^2} - f \frac{\partial \phi}{\partial \eta} = \frac{\alpha_0 \delta^2}{f} \frac{\partial \rho'}{\partial x} \tag{4.11}$$

The boundary condition (4.7a) may be rewritten as

$$\frac{\partial \phi}{\partial \xi} - \frac{f h_0}{\alpha_0 \delta} \frac{\partial \phi}{\partial \eta} = \frac{\delta \alpha_0}{f} \rho' - \frac{h_0^2}{2\delta \alpha_0} \frac{\partial \rho'}{\partial \eta} \tag{4.12}$$

The relative importance of the two terms on the right-hand side of (4.12) may be decided by an order of magnitude estimation. Because $\rho'$ and $\partial \rho'/\partial \eta$ are order one by the present scaling, the terms $\delta \alpha_0 \rho'/f$ and $h_0^2/(2\delta \alpha_0) \partial \rho'/\partial \eta$ on the right-hand side of (4.12) are of the order $\delta \alpha_0$ and $h_0^2/(\delta \alpha_0)$ respectively. The ratio of the latter to the former is $(h_0/\alpha_0)^2/\delta^2$. Therefore, if the coastal wall is inside the topographic boundary layer ($h_0/\alpha_0 << \delta$), the first term, $\delta \alpha_0 \rho'/f$, dominates.

In the atmospheric cooling case, the forcing scale along the x axis is approximately the shelf width. The stream function $\phi$ is of the order $\delta$ at most by the use of (4.11) and (4.12), and an order one longshore nondivergent velocity cancels the divergent longshore velocity at the coast. For a coastal buoyancy flux, a density boundary layer width

$$\delta_R \sim \gamma h_0 / R_0$$

can be found from the density boundary condition (4.7b). The forcing term on the right-hand side of (4.11) is then of the order $(\alpha_0 \delta/f) \delta/\delta_R$. The salinity gradient caused by freshwater runoff is generally limited to a narrow near-shore band inside the topographic boundary layer. Therefore, $\delta/\delta_R >> 1$ and forcing on the right-hand side of (4.11)

dominates those on the right-hand side of (4.12). Although the forcing term is significant only inside a density boundary layer, the flow field extends to a wider topographic boundary layer. Outside the topographic layer, the flow is weak. A similar situation occurs at the shelf break. The influence of the shelf break front on the mean flow is limited to the vicinity of the front. We will suppose that the flow over the mid-shelf is not greatly affected by these boundary layers.

The density boundary condition (4.7b) shows that large density perturbations are produced when $h_0$ is small. However, the above analysis demonstrates that the main forcing on the vorticity equation comes from the term on the right-hand side of (4.11), which is independent of $h_0$. Consequently, the artificial coastal wall is not critical for the solutions, and the singularity in the density equation has only local effect.

4.3 Dispersion of an Initial Density Perturbation along Isobaths

Equation (4.10) shows that the density field over the mid-shelf is characterized by a shock wave-like propagation of the density perturbation along isobaths. Simple analytical solutions of (4.10) may be used to describe the development of density field from an initial density distribution. The examples given in this section refer to the case of a shelf in the Northern Hemisphere. In the Southern Hemisphere, the propagation direction is reversed.

Let the initial density perturbation along a particular isobath be

$$\rho' = F(y) \qquad \text{at } t = 0 \qquad (4.13)$$

which may be produced, e.g. by a sudden overturning of the water column. Let the perturbation be limited in the y- direction in such a way that:

$$F(y) \to 0 \qquad \text{as} \quad y \to \pm\infty \tag{4.14}$$

For a shelf with constant slope $\alpha_0$, we will replace y by $\eta = -fy/\alpha_0$. Equation (4.10) is then reduced to

$$\frac{\partial \rho'}{\partial t} + \rho' \frac{\partial \rho'}{\partial \eta} = \nu \frac{\partial^2 \rho'}{\partial \eta^2} \tag{4.15}$$

where $\nu = \gamma/\alpha_0^2$. This is Burgers' equation (Whitham, 1974). Illuminating results follow from the known analytical solutions of (4.15).

The characteristics of the flow depend on the sign of F(y). $F(y) > 0$ corresponds to an excess of density, and $F(y) < 0$, a deficiency of density. Assume an initial delta function density perturbation

$$F(\eta) = A\delta(\eta) \qquad A > 0 \tag{4.16}$$

The solution of (4.15) is given by

$$\rho'(\eta,t) = \sqrt{\frac{\nu}{t}}\, \frac{(e^{\mu}-1)\, e^{-\eta^2/(4\nu t)}}{\sqrt{\pi} + (e^{\mu}-1)\int_{\frac{\eta}{\sqrt{4\nu t}}}^{\infty} e^{-z^2}\, dz} \tag{4.17}$$

where $\mu = A/2\nu$ (Whitham, 1974). Two parameter ranges of $\mu$ in (4.17) are of interest. For $\mu \ll 1$, the denominator in (4.17) is $\sqrt{\pi} + O(\mu)$ and

$$\rho'(\eta,t) \simeq \frac{A}{\sqrt{4\pi\nu t}}\, e^{-\frac{\eta^2}{4\nu t}} \tag{4.18}$$

This is the solution of the heat equation for an initial delta function distribution of temperature. Indeed in this approximation

$$\rho' \frac{\partial \rho'}{\partial \eta} \ll \frac{\partial^2 \rho'}{\partial \eta^2}$$

and

$$\frac{\partial \rho'}{\partial t} \simeq \nu \frac{\partial^2 \rho'}{\partial \eta^2}$$

which is precisely the heat equation. The density disturbance diffuses evenly in both $+\eta$ and $-\eta$ direction away from the source. The other parameter range $\mu \gg 1$ is of greater interest. We write $\theta = \eta/(2At)^{1/2}$. For $\eta > 0$, the asymptotic expansion of the integral in (4.17) is

$$\int_{\sqrt{\mu}\theta}^{\infty} e^{-\zeta^2} d\zeta \sim \frac{e^{-\mu\theta^2}}{2\sqrt{\mu}\,\theta}\left(1 - \frac{1}{2\mu\theta^2} + \cdots\right), \quad \mu \gg 1$$

To the leading order, (4.17) becomes

$$\rho' \simeq \sqrt{\frac{\nu}{t}}\, \frac{e^{\mu}\, e^{-\mu\theta^2}}{\sqrt{\pi} + e^{\mu} e^{-\mu\theta^2} \frac{1}{2\sqrt{\mu}\,\theta}}$$

or

$$\rho' \simeq \sqrt{\frac{2A}{t}}\, \frac{\theta}{1 + 2\theta\sqrt{\pi\mu}\, e^{\mu(\theta^2-1)}} \; ; \quad \theta = \frac{\eta}{\sqrt{2At}} > 0 \; ; \qquad \mu \to \infty \tag{4.19}$$

In the limit $\mu >> 1$, the term $2\theta\sqrt{\pi\mu}\exp[\mu(\theta^2-1)]$ is much greater than 1 for $\theta > 1$, and is much smaller than 1 for $\theta < 1$. Equation (4.19) is further approximated by

$$\rho'(\eta,t) \simeq \eta/t \qquad \text{in } 0 < \eta < (2At)^{1/2} \tag{4.20}$$
$$\simeq 0 \qquad \text{otherwise.}$$

This solution is of a saw-tooth shape. A density front is formed at $\eta = (2At)^{1/2}$ and $\rho'$ jumps from $(2A/t)^{1/2}$ to zero across the front. The width of the front can be estimated by using a Tayor expansion of Equation (4.19) at $\theta = 1$. Let $\theta = 1 - \theta'$, where $\theta' << 1$. We have

$$\rho' \simeq \sqrt{\frac{2A}{t}} \; \frac{(1-\theta')}{[1+2(1-\theta')\sqrt{\pi\mu}\, e^{4\mu\theta'}]}$$

For $\mu >> 1$

$$\rho' \simeq \sqrt{\frac{A}{2\pi\mu t}} \; e^{-4\mu\theta'}$$

The width of the density front is given by $\theta' = 1/4/\mu$, or $\nu t^{1/2}/(2A)^{1/2}$ in $\eta$ coordinate. Figure 4.1 is a sketch of $\rho'(2A/t)^{-1/2}$ as a function of $\eta(2At)^{-1/2}$.

The position of the density front is determined by $\eta = (2At)^{1/2}$. It follows that the front moves in the $+\eta$ direction with a speed $(A/2t)^{1/2}$. Since the dependent variable in Figure 4.1 is $\rho'(2At)^{-1/2}$, the maximum magnitude of density perturbation decreases as $t^{-1/2}$, independent of $\gamma$.

However, the total density perturbation along an isobath is conserved. This is easily seen by integrating (4.15) from $\eta = -\infty$ to $+\infty$:

$$\frac{\partial}{\partial t}\int_{-\infty}^{\infty} \rho' d\eta = -\frac{\rho'^2}{2}\Big|_{\eta=-\infty}^{\infty} + \nu \frac{\partial \rho'}{\partial \eta}\Big|_{\eta=-\infty}^{\infty} = 0$$

where $\rho' = 0$ and $\partial\rho'/\partial\eta = 0$ at $\eta = \pm\infty$ have been used. The evolution of the density structure of a heavy water blob described by (4.19) is sketched schematically in Figure 4.2. It is obvious that the heavy water perturbation moves along isobaths in the direction of Kelvin wave propagation.

The characteristics of the solution for an initial density deficiency are different from those of (4.20). Let

$$F(\eta) = -A\delta(\eta) \qquad A > 0 \qquad \text{at } t = 0$$

The asymptotic behavior is

$$\rho(\eta) \simeq -\eta/t \qquad \text{in } -(2At)^{1/2} < \eta < 0$$
$$\simeq 0 \qquad \text{otherwise}$$

which is the same as the solution for a positive initial perturbation, except that the direction of propagation is reversed. The longshore density dispersion for a negative perturbation is also shown in Figure 4.2.

In the oceanic bottom water formation, the density distribution is

seldom a delta function. Nevertheless, certain properties of the solution (4.17), e.g. the speed of front propagation and the conservation of total density perturbation, are independent of the diffusion coefficient. For a general density distribution with $\mu \gg 1$, they can be inferred from the first order equation by neglecting the diffusion term:

$$\frac{\partial \rho'}{\partial t} + \rho' \frac{\partial \rho'}{\partial \eta} = 0 \tag{4.21}$$

For an initial perturbation $F(\eta)$, the solution of (4.21) is

$$\rho' = F(\eta - \rho' t) \tag{4.22}$$

$\rho'$ is constant along characteristic curves, which are straight lines with slope $\rho'$ on the $\eta$-t plane. The front forms when two characteristic curves intercept. The propagation speed of the density front, c', which is different from the slope of characteristic curves, can be found by transformation to a coordinate system moving with the front. Letting $\eta' = \eta - c't$, $t' = t$, and $G = \rho'^2/2$, (4.21) becomes

$$\frac{\partial \rho'}{\partial t'} - c' \frac{\partial \rho'}{\partial \eta'} + \frac{\partial G}{\partial \eta'} = 0 \tag{4.23}$$

In (4.23), $\partial\rho'/\partial t'$ is of order one in the coordinate system moving with the front. But $\partial\rho'/\partial\eta'$ is much greater than one. Assuming that the front is at $\eta' = 0$, we integrate (4.23) across the front from 0- to 0+

$$-c'[\rho'(0^+) - \rho'(0^-)] + G(0^+) - G(0^-) \simeq 0$$

Therefore, c' is given by

$$c' \simeq \frac{G(0^+) - G(0^-)}{\rho'(0^+) - \rho'(0^-)} \simeq \frac{1}{2}[\rho'(0^+) + \rho'(0^-)] \qquad (4.24)$$

If c is the propagation speed in the y-coordinate, it may be written as

$$c \simeq -\frac{\alpha_0}{2f}[\rho'(0^+) + \rho'(0^-)] = \frac{1}{2}[v_d(0^+) + v_d(0^-)] \qquad (4.25)$$

Equation (4.25) shows that the front propagation speed is the average of $v_d$ across the front.

We define the total long-isobath kinetic energy per unit depth as

$$\int_{-\infty}^{\infty} \frac{1}{2} v_d^2 \, dy = \frac{\alpha_0^2}{f^2} L_y \int_{-\infty}^{\infty} \frac{1}{2} \rho'^2 \, d\eta$$

To examine the decay of kinetic energy, Equation (4.15) is multiplied by $\rho'$ and integrated from $y = -\infty$ to $+\infty$. Using the boundary conditions $\rho' = 0$ and $\partial\rho'/\partial\eta = 0$ at infinity, we have

$$\frac{\partial}{\partial t} \int_{-\infty}^{\infty} \frac{1}{2} \rho'^2 \, d\eta = -\frac{\nu}{2} \int_{-\infty}^{\infty} \left(\frac{\partial \rho'}{\partial \eta}\right)^2 d\eta$$

The front region with strong density gradient is mainly responsible for the dissipation. The width of the front has been estimated earlier in

this section as $v/(2A/t)^{1/2}$. Therefore, $\partial\rho/\partial n \simeq 2A/(vt)$ and

$$\frac{\partial}{\partial t}\int_{-\infty}^{\infty} \tfrac{1}{2} v_d^2 \, dy = -\frac{\alpha_0^4 L_y}{2f^2}\left(\frac{2A}{t}\right)^{3/2}$$

The kinetic energy of density perturbation decays as $t^{-3/2}$. The decay is fast if the perturbation is strong or the bottom slope is large.

We will estimate physical quantities of the flow field from the above results. The most significant quantity is the propagation speed of a density front. Suppose that at t = 0, the perturbation in density is concentrated at y = 0 with total density excess of $0.2 \times 10^4$ gm/cm$^2$ along an isobath. $\mu$ is 12.5 if $K_H = 4 \times 10^6$ cm$^2$/sec and the bottom slope is $10^{-3}$. Equation (4.20) shows that the maximum density inside the saw-tooth shape perturbation will have a value of $0.28 \times 10^{-3}$ gm/cm$^3$ over a longshore distance of 140 km after 47 days. The front propagation speed is 1.7 cm/sec. After 6 months, the maximum density will be $0.14 \times 10^{-3}$ gm/cm$^3$ and the density perturbation spreads over a longshore distance of 277 km. The front propagation speed has decreased to 0.87 cm/sec.

In the case of flow driven by density flux at the coast, the flow behavior depends on the characteristics of the topographic and density boundary layers. To demonstrate this situation for a shelf with constant slope $\alpha_0$, we eliminate $u_b$ from (4.1a, b). The resulting equation is

$$-f\alpha_0 \frac{\partial v_b}{\partial y} = \varepsilon \frac{\partial^2 v_b}{\partial x^2} + \alpha_0^2 \frac{\partial \rho'}{\partial y} \qquad (4.26)$$

The boundary condition is $v_b = 0$ at x = 0. In the Northern Hemisphere,

the bottom velocity field in the topographic boundary layer spreads in the -y direction independent of the sign of $\rho'$, because of the parabolic nature of (4.26). However, the flow direction is determined by the density perturbation. We will call -y the forward direction as before and assume that the longshore density perturbation is limited between $y = 0$ and $y = -L_y$. For a buoyancy flux ($\rho' < 0$), $\partial\rho'/\partial y$ is positive at $y = 0$ and negative at $y = -L_y$. In terms of the heat conduction analogy, there is a "heat" source at $y = 0$ and a "heat" sink at $y = -L_y$. The longshore velocity develops from zero at $y = 0$ to a positive value at $y = -L_y$. In the region $y < -L_y$, the longshore flow becomes negative near the coast. This negative longshore flow extends outward in the -y direction in a parabolic boundary layer.

Because $v_b = 0$ at $y = 0$, there is no density advection backward across the line $y = 0$. At $y = -L_y$, the longshore flow goes from zero at the coast to a negative value in the near-shore region. This flow will advect the negative density perturbation forward beyond the $y = -L_y$ line. Therefore, longshore dispersion of near-shore light water in the -y direction will develop with time.

For a positive density perturbation, the flow direction is reversed. We have $v_b = 0$ at $y = 0$ as before. However, $v_b$ is now positive at $y = -L_y$ near the coast. It prevents the longshore density advection to the region $y < -L_y$. The initial spreading of dense water is offshore. When there is significant dense water in the interior region, the self-advection process discussed earlier comes into play. These qualitative differences in flow responses to coastal buoyancy flux and

density flux will be examined numerically in the next section.

## 4.4 Numerical Solutions

In this section, Equations (4.3), (4.5), and (4.6) are solved numerically for flow forced by a coastal buoyancy source and surface density flux over a limited area. The topography used in the computation is uniform in y and has a shelf width of 160 km (Figure 3.1). A vertical wall is placed in the near-shore region with boundary conditions given by (4.7a, b). Since the forcing term in (4.6) is inversely proportional to the water depth h, the density perturbation is small for large h. The seaward boundary conditions in (4.8) are applied to some deep water locations or outside the region of density perturbations on the shelf. The analyses in the previous section show that the solutions are characterized by density dispersion in the forward direction. Therefore, the flow and the density perturbation vanish at the backward boundary. To avoid the unrealistic boundary layers at the forward boundary, we approximate the boundary conditions in (4.8) by the computational ones, $\partial\rho'/\partial y = \partial\phi/\partial y = 0$, for technical convenience (Roache, 1976).

The computation starts with $\rho' = 0$ and $\phi = 0$ when the forcing is applied at $t = 0$. At each time step, the density equation is solved by an implicit scheme (Roache, 1976), and the velocity field is calculated in the same way as in Section 3.3. One iteration is used at each time step to estimate the advection velocity. The computation proceeds for a dimensional time period of about six months.

### 4.4.1 The Density and Velocity Scales

Because of the nonlinearity of the problem, the resulting density

perturbations are not linearly related to the magnitudes of forcing. It is necessary to deal with each case with different density flux separately. Since the choices of density and velocity scales are arbitrary, we will use the scales which provide computational convience. For density-driven flow, the velocity is scaled by the magnitude of density perturbation. Therefore, the parameter $\sigma$, which is the relative contribution of the density-driven component to the total velocity, is chosen to be 1. We will use the definitions in Chapter 2 for nondimensional parameters, and "~" represents scales of variables as used earlier. In terms of dimensional constants, the choice of $\sigma = 1$ gives a diffusivity

$$\gamma = \rho_o f_o K_H / (g\tilde{H}\Delta\tilde{\rho}) \tag{4.27}$$

The nondimensional coastal buoyancy flux and surface density flux with $\sigma = 1$ are

$$R_o = \rho_o f_o \tilde{R} / (g\tilde{H}D\Delta\tilde{\rho}^2) \tag{4.28}$$

$$Q_o = \rho_o f_o \tilde{Q}\tilde{L} / (g\tilde{H}D\Delta\tilde{\rho}^2) \tag{4.29}$$

In the river buoyancy flux case, the density field is determined by both near-shore advection and diffusion. A river stream flux of 1000 $m^3$/sec is about that of the Hudson estuary in the Middle Atlantic Bight. Assume that this flux spreads over 100 km of coastline to avoid large

density gradient at the coast. The flux per unit coastline is then 100 $cm^2/sec$, which is about the average flux in the Middle Atlantic Bight. Using a value of 0.025 $gm/cm^3$ as the density contrast between the river water and the shelf water, we have $\tilde{R}$ = 2.5 gm/sec/cm. A density scale of 0.001 $gm/cm^3$ will give $R_0$ = 0.025. The velocity scale is then derived from the density scale by using the relation $\sigma$ = 1. Table 4.1 lists the parameters related to a forcing magnitude of $\tilde{R}$ = 2.5 gm/sec/cm.

Typical winter heat loss in the Middle Atlantic Bight is 250 $Watts/m^2$. With a heat capacity of 1°C/cal and a thermal expansion coefficient of $10^{-4}$ $cm^3/°C$ for sea water at 5°C, this heat loss corresponds to a density flux of $6 \times 10^{-7}$ $gm/sec/cm^2$ into the water. To find a density scale from this forcing magnitude, we assume that the density advection is not significant until at $t \simeq O(1)$. A convenient scale $\Delta\tilde{\rho}$ is obtained by using $Q_0$ = 1 in (4.29). We have

$$\Delta\tilde{\rho} = (\rho_0 f_0 \tilde{Q}/g)^{1/2}/D \qquad (4.30)$$

The nondimensional parameters and scales derived from this density flux are listed in Table 4.2 .

4.4.2 Coastal Density Flux Forcing

In the numerical computation for the flow driven by coastal density flux, a coastal wall is placed at x = 0.2 in the topography of Figure 3.1. The water depth is 25 m at the coast. The seaward boundary is at x = 1.45 with a depth of 130 m. The river flux is located from y = -1 to 0. The characteristics of the flow and density fields are demonstrated

by the solution with $R_0/\gamma = 2.5$ and $\gamma = 0.025$. These parameters correspond to the dimensional quantities specified in Table 4.1. The nondimensional forcing function R is 1 from y = -1.0 to y = 0 and zero otherwise. Figure 4.3 shows the development of density field as a function of time. At t = 1, the advection of density is not significant and the contour lines are only slightly distorted from a simple diffusion cloud. The advection to the -y direction becomes obvious at t = 5. The density deficiencies are limited inside a coastal density boundary layer, and spreads toward the -y direction. In the region y > 0, the density diffusion dominates, and the dispersion of density perturbation is small. For t > 5, the feature is similar to that at t = 5 with the density perturbation propagating further to the -y direction. The mean propagation speed of the density perturbation in this figure is about 0.3 in nondimensional unit or 2.6 km/day dimensionally.

The mechanism of this density advection can be examined from the bottom geostrophic velocity distributions in Figure 4.3. At t = 1, the bottom geostrophic velocity is not quite established. Consequently, the density advection is weak. Significant bottom geostrophic velocity is present at $t \geq 5$. For y > 0, there is a weak onshore flow which compensates the offshore thermohaline transport caused by a longshore density gradient at the coast [Equation (4.7a)]. In the region $-1 \leq y \leq 0$, the velocity field is dominated by the divergent velocity component associated with the large near-shore density deficiency [Equation (4.3)]. This divergent velocity is longshore and positive. In the region y < -1.0, a topographic boundary layer is produced by the

TABLE 4.1

Scales and Nondimensional Parameters for Flow

Driven by Coastal Buoyancy Flux

| Symbol | Numerical values |
|---|---|
| $\tilde{R}$ | 2.5 gm/sec/cm |
| $R_o$ | 0.025 |
| $\Delta\tilde{\rho}$ | $10^{-3}$ gm/cm$^3$ |
| $f_R = f_o^2\tilde{L}/(g\Delta\tilde{\rho}/\rho_o)$ | 0.1 |
| $\epsilon_R = D/f_R$ | 0.01 |
| $\tilde{U} = \epsilon_R f_o \tilde{L}$ | 10 cm/sec |
| $\tilde{T} = \tilde{L}/\tilde{U}$ | $10^6$sec (11.6 days) |
| $K_H$ | $10^6$ cm$^2$/sec |
| $\gamma$ | 0.01 |

TABLE 4.2

Scales and Nondimensional Parameters for Flow

Driven by Surface Density Flux

| Symbol | Numerical values |
|---|---|
| $\tilde{Q}$ | $6 \times 10^{-7}$ gm/cm$^2$/sec |
| $\Delta\tilde{\rho} = (\rho_o f_o \tilde{Q}/g)^{1/2}/D$ | $0.2 \times 10^{-3}$ gm/cm$^3$ |
| $f_R = f_o^2 \tilde{L}/(g\Delta\tilde{\rho}/\rho_o)$ | 0.41 |
| $\varepsilon_R = D/f_R$ | 0.0024 |
| $\tilde{U} = \varepsilon_R f_o \tilde{L}$ | 2.4 cm/sec |
| $\tilde{T} = \tilde{L}/\tilde{U}$ | $4 \times 10^7$ sec (47 days) |
| $\gamma$ | 0.04 |

coastal longshore density gradient near $y = -1$. This boundary layer develops in the $-y$ direction and is similar to the one under longshore wind stress forcing (Chapter 3). The flow inside the boundary layer is longshore to the $-y$ direction, and is responsible for the longshore advection of density deficiencies.

The evolution of the density minimum at $y = -1.0$ as a function of time is plotted in Figure 4.4. There is a rapid initial density decrease after the coastal buoyancy flux is applied. At $t \simeq 2$, a quasi-steady state is reached. In this quasi-steady state, the magnitude of the density minimum does not change significantly, and the buoyancy influx is balanced by the longshore advection. It is clear that the minimum density per unit forcing strength depends only weakly on $\gamma$.

The longshore density advection is further demonstrated in Figure 4.5, where the density distribution at $x = 0.3$ is plotted as a function of $y$ for $R_0/\gamma = 2.5$. At $y = 0$, the density deficiency diffuses away from the source. However, at $y = -1$, the development of density field is by advection. At $t = 1$, the density deficiency is advected only slightly beyond $y = -1$ in the $-y$ direction. Significant advection occurs at $t = 5$, and the light river water reaches $y = -3$. This qualitative difference for the density distributions in the forward and backward directions is also clear at $t = 10$.

To find the parameter dependence of this self-advection process, the coastal longshore density distribution at $t = 10$ is plotted in Figure 4.6 with fixed $R_0/\gamma = 2.5$ for $\gamma = 0.05$ ($R_0 = 0.125$) and $\gamma = 0.025$ ($R_0 = 0.0625$). In dimensional terms, it is equivalent to fixing $R^*/K_H$

and changing $K_H$. In the region $y > -1.0$, where the density diffusion process dominates, the density distribution depends on the magnitude of $\gamma$. However, in the density advection region ($y < -1.0$), the differences in density structure for various $\gamma$ are small. The characteristics of the flow are also examined in Figure 4.6 for different $\gamma$ with $R_o$ equal to 0.0625. The distributions for $\gamma = 0.025$ and 0.05 are quite different. The latter shows a much stronger advection than the former. It seems that the characteristics of longshore density advection depend on the magnitude of $R_o/\gamma$.

The dependence of density field on the magnitude of forcing is shown in Figure 4.7, where $\gamma = 0.025$ and $R_o/\gamma$ varies. Dimensionally, it is equivalent to varying R* for the same $K_H$. The density distribution at $x = 3$, scaled by $R_o/\gamma$, is plotted as a function of longshore distance for $t = 10$. The distribution of density produced by diffusion alone is also shown in this figure. It is clear that the density advection is stronger for larger $R_o$.

Although density fronts are not present in the coastal boundary layers, the self-advection process is still significant. The numerical results shown above suggest that the parameter $R_o/\gamma$ determines the strength of self-advection, similar to the dependence of shock-wave like characteristics on $\mu$ in Burgers' equation. It is possible to find the relation between $R_o/\gamma$ and $\mu$. In Burgers' equation, $\mu$ is proportional to the ratio of total density perturbation to the diffusivity. For the river outflow problem with a longshore width of $L_R$, we can use the rate of total buoyancy flux, $R_o L_R$, as the magnitude of density

perturbation. We have

$$\mu = R_o L_R \alpha_o^2/(2\gamma)$$

Therefore, $R_o/\gamma$ is a measure of the importance of advection in a flow driven by a coastal buoyancy source with fixed $L_R$.

The density distribution and the flow field also depend on the sign of R. A negative R corresponds to a density source at the coast (a "sinking" plume). Figure 4.8 shows the development of the density and flow fields with R = -1 between y = -1 and y = 0. The values of $R_o$ and $\gamma$ are the same as those used in Figure 4.8. This case is qualitatively different from the one with a positive R. Close to y = 0, the bottom flow is weak and the density field is dominated by the diffusion process as in the buoyancy flux case. However, in the region y < -1, the longshore velocity near the coast is positive, which prevents the density excess from being advected into the region y < -1. Offshore advection of heavy water into the interior region can be seen at t = 5. At t = 10, there is a significant amount of dense water outside the coastal boundary layer. It is clear that the flow in the interior region is governed by the dispersion of dense water along isobaths as discussed in Section 4.2 (Figure 4.8d). The resulting density field is much the same as the flow forced by surface cooling over the outer shelf, which will be studied in the next section. Figure 4.9 is a contour plot of the isopycnals on the y-t plane. It clearly shows the propagation of dense water to the -y direction in the interior region.

4.4.3 Flow Forced by Surface Density Flux

To demonstrate the evolution of the density and flow fields produced by surface density flux, numerical solutions have been obtained for a flux which is present from t = 0 to t = T. The surface density flux is uniform in the cross-shelf direction. It has the form:

$$Q(y) = \begin{cases} \pi/2 \sin(\pi y/L_y) & -L_y < y < 0 \\ 0 & \text{otherwise} \end{cases}$$

The density flux at the coast is zero in this case. The corresponding dimensional quantities can be found in Table 4.2. Figure 4.10 shows the development of density field with T = 2, $L_y$ = 1 and $\gamma$ = 0.05. These parameters correspond to cooling over a 100 km longshore distance for 3 months. The parameter $\mu$, which determines the behavior of Burgers' equation, is 20 in this case. One expects that density fronts will form. At t = 1, the density field can be approximated by the local response to cooling (Figure 4.10a). The dominant balance is

$$\partial\rho/\partial t = Q/h \qquad (4.31)$$

The contour lines are slightly distorted to the -y direction and a density front with strong longshore gradient begins to form. The density front is clearly shown at t = 2 and the advection of density perturbation is apparent (Figure 4.10b). After the forcing stops at t = 2, the front

continues to propagate in the -y direction (Figure 4.10c). At this stage, the movement can be inferred from Burgers' equation (4.15). The magnitude of density perturbation decreases because of the longshore spreading and diffusion.

The longshore bottom geostrophic velocity produced by the density field is plotted in Figure 4.11. When forcing is present ($t \leq 2$), a negative longshore flow is developed in the forcing region. This is the divergent component of bottom velocity given by (4.3). The maximum velocity on the shelf is 2.0 (Figure 4.11b). Strong longshore flow exists at the shelf break, since the steep bottom slope is very effective in generating bottom flow as shown by (4.3). Near the coast, a topographic boundary layer with positive longshore velocity develops in the -y direction. After the forcing terminates, the longshore velocity associated with the density distribution decays. The maximun velocity is located at the shelf break. The x-component of bottom geostrophic velocity is weak except inside a topographic boundary layer near the coast as shown in Figure 4.12a. The flow is onshore with a magnitude of 0.7. By the time $t = 5$, it decreases to less than 0.1.

The formation and propagation of density fronts in the -y direction is demonstrated in Figure 4.13, where the density is plotted along the $x = 1$ isobath. At $t = 1$, the distribution is due to the direct response to cooling. Advection is weak at this time. As the density continues to increase, advection becomes more important and the excess density is advected away from the forcing region in the -y direction. At $1 < t < 2$, there is a balance between the density input and the horizontal

advection, and a quasi-steady value for the maximum density is reached. During this period, the mean front propagation speed calculated from (4.24) is about 1, which agrees with the mean speed estimated from the locations of maximum density in Figure 4.13. After the forcing stops at $t = 2$, the forward face of the front continues to propagate, and the density at the trailing part decreases. A saw-tooth shape distribution is formed as demonstrated by the solution of Burgers' equation given by (4.20).

The longshore dispersion of density perturbation is clearly demonstrated in Figure 4.14, where constant density lines are shown on the y-t plane. In this case, $\gamma = 0.1$ and cooling is applied from $t = 0$ to 2 over a longshore range between $y = -1.0$ to 0. In the cooling stage, $0 < t < 2$, the density maximum propagates in the $-y$ direction with a nearly constant speed. After the cooling ends at $t = 2$, the propagation speed of the location of density maximum becomes faster initially and slows down after $t = 3$. At $t = 5$, the propagation is so slow that the density maximum is nearly stationary. It is easy to understand why this happens. The longshore advection tends to move the front forward. However, the strong longshore diffusion in the front region erodes the front and moves the location of the density maximum backward. If a balance between these two tendencies is achieved, the location of the density maximum will be stationary.

The characteristics of density field can be found by examining solutions with different nondimensional diffusivities. The density distribution along the $x = 1$ isobath for $\gamma = 0.1$ is plotted in Figure

4.15. During the forcing period, the propagation speed of the front is approximately equal to the one with $\gamma = 0.05$ in Figure 4.13. However, in the free propagation stage ($t > 2$), the front is dissipated faster than that in Figure 4.13. At $t = 4$, the front is almost stationary as shown in Figure 4.14.

With longer forcing duration, the maximum density remains the same (Figure 4.16). Since the propagation speed depends on the magnitude of perturbation, it is unchanged during cooling. Once the cooling ends, the one with shorter cooling duration will decay faster. The longshore range of cooling has a stronger effect on the density and velocity fields than the duration of cooling. Figure 4.17 shows the longshore density distribution for $L_y = 2$ and $T = 2$. The maximum density in this case is larger than that with $L_y = 1$. Therefore, the front in Figure 4.17 has a faster propagation speed.

4.4.4 Discussion

Before a comparison with observation is made, we must briefly discuss the applicability of the model under various circumstances. During the winter months in the Middle Atlantic Bight, dense water formed at the surface sinks rapidly to the bottom and the resulting vertical density distribution is nearly uniform. During this period, the low salinity water from the river inflow is also mixed to the bottom. This is the situation which is most likely to be described by the model. In summer, a strong thermocline is formed at a depth of about 15 - 20 m. The horizontal density gradient in the surface layer is small. In the lower layer, the water is not affected significantly by heating and the

assumption of vertical homogeneity is still approximately true. However, the strong pycnocline prevents the river water from reaching the bottom, and the river water spreads at the surface to a long distance offshore. The idealizations used above do not apply to the case of river forcing under vertical stratification.

Equations (2.18) and (2.19), which determine the bottom geostrophic velocity, are derived under a general stratified condition. They are not affected by the presence of a seasonal thermocline at the mid-depth. The nondimensional density equation is given by

$$\frac{\partial \rho'}{\partial t} + (u_b + u_c + u_f)\frac{\partial \rho'}{\partial x} + (v_b + v_c + v_f)\frac{\partial \rho'}{\partial y} + w\frac{\partial \rho'}{\partial z} = \gamma \frac{\partial^2 \rho'}{\partial x^2} + \gamma \frac{\partial^2 \rho'}{\partial y^2} + \gamma \frac{\partial^2 \rho'}{\partial z^2}$$

where the subscripts "b", "c", and "f" represent the bottom geostrophic component, the thermohaline component, and the frictional component of velocity field respectively. Considering a strong seasonal thermocline at the mid-depth and a homogeneous water column in the vertical direction below the thermocline, we have

$$\frac{\partial \rho'}{\partial z} = 0$$

in the lower layer. Below the thermocline, the thermohaline velocities $u_c$ and $v_c$ are given by (2.11) and (2.13):

$$u_c = \frac{\sigma}{f}\frac{\partial \rho'}{\partial y}(z + h)$$

$$v_c = -\frac{g}{f}\frac{\partial \rho'}{\partial x}(z+h)$$

In this case, the density advection caused by the thermohaline velocity is identically zero in the lower layer. Above the bottom frictional layer, $u_f$ and $v_f$ are negligible. The balance between the rate of density change and the horizontal advection by the bottom geostrophic velocity still holds below the seasonal thermocline. It is likely that the propagation of density perturbation in the lower layer is not affected. Besides giving a description of the density-driven flow in winter and earlier spring, the model also gives some clues on the water movement below the seasonal thermocline in summer.

We have treated the river effect as a density flux distributed along a larger piece of the coast. This is certainly not valid at the mouth of the estuary. However, the intent is to model the circulation over length scales of the order of shelf width and larger. The detailed density structure near the source should have no influence on the dynamics of shelf-wide circulation. The same boundary condition was used by Hendershott and Rizzoli (1976).

4.5 Evidence of Bottom Water Movement on Continental Shelves

Although detailed comparison between model results and observations is not possible, some model predictions on bottom water movement on continental shelves can be used to explain the observed bottom density field. We will discuss in this section some observational evidence in the Adriatic Sea, the Antarctic Continent, and the Middle Atlantic Bight.

4.5.1 Winter Circulation in the Adriatic Sea

Circulation in the Adriatic Sea in the winter of 1965-1966 was studied by Hendershott and Rizzoli (1976). A cold air mass outbreak from eastern Europe reached the Adriatic Sea on January 6, 1966, and resulted in intense cooling, which lasted for about 20 days. From the meteorological data, Hendershott and Rizzoli (1976) estimated a surface density flux of $1.5 \times 10^{-6}$ gm/cm$^2$/sec during this period. Their density sections of February 1966 showed that the water was vertically homogeneous and a density increas of $0.5\text{-}1.0 \times 10^{-3}$ gm/cm$^3$ from the November value was observed.

The most significant features during this cooling period were the formation of a cyclonic gyre in the northern Adriatic Sea and the advection of density field by this gyre. A "tail" of dense water could be seen in their plot of the horizontal density distribution in February 1966. This dense water extended southward to Jabuka Pit along the bottom topography on the western side of the basin. Along the Italian coast, a band of low salinity water from the Po River was also observed. These features were demonstrated in a numerical model by Hendershott and Rizzoli (1976) as being caused by forcing from surface density input and coastal buoyancy flux. The long-isobath dispersion of density perturbations and the formation of a cyclonic gyre were shown in their results.

The theory formulated in this chapter can explain both the numerical and the observational results. We will first calculate the value of $\mu$ defined in Section 4.3. Because of the complex bottom topography and the geometry of the basin, we will use an average bottom slope of $10^{-3}$. For

a density perturbation of $0.5 \times 10^{-3}$ gm/cm$^3$ over a long-isobath distance of 100 km, $\mu$ is 15. Therefore, the cooling event in the Adriatic Sea in earlier 1966 was dominated by the self-advection process discussed earlier in this chapter. Comparison can be made between the predicted and observed propagation speeds of the "tail" of dense water. In the observed horizontal density distribution, the "tail" reached Jabuka Pit in early February. If we assume that the dense water covered a distance of 200 km from its main location in the north to Jabuka Pit during this cooling period, the mean propagation speed would be 6.6 km/day. A rough estimate of the propagation speed from the numerical solution of Hendershott and Rizzoli is about 200 km in 40 days, or 5 km/day. These values can be compared with the theoretical one given by (4.16). Using a density difference of $1.0 \times 10^{-3}$ gm/cm$^3$ and a mean bottom slope of $10^{-3}$, the front propagation speed is 4.3 km/day. Considering the difficulty in determining the initial location of dense water in the data, this value is not significantly different from the observed one.

In analyzing their results, Hendershott and Rizzoli (1976) demonstrated diagnostically that the flow pattern could be explained by the density distribution at each time step. The present theory shows that density fronts are formed and propagate out of the formation region as shock-wave like structures. This prognostic interpretation gives some insight into the dynamics of winter circulation in the Adriatic Sea.

4.5.2 Bottom Water Movement in the Antarctic Continent

Another area where the bottom water movement has been observed is the

Weddell Sea in the Antarctic Continent. Gill (1973) suggested that the dense water was formed by salt release during freezing of the surface water. He also observed that the horizontal salinity gradient could become large in the Weddell Sea. The dense water flowed westward on the shelf after sinking to the bottom. A westward increase of salinity of 0.4 o/oo was observed (Gill, 1973). This westward movement of bottom water was also shown in the map of bottom potential temperature distribution given by Foster and Carmark (1976). Dense water accumulation on the western side of the Ross Sea was observed by Jacobs et al. (1970). Current measurements by Foldvik and Kvinge (1974) indicated a strong westward flow (≃ 7 cm/sec) at the shelf break in the Weddell Sea.

The present theory gives a simple explanation to the formation of strong horizontal density gradient and the westward movement of bottom water. Because of the deficiency of data, a detailed comparison with observations can not be made. However, the atmospheric influence over the Antarctic Continent should be more effective in producing bottom water than in the Adriatic Sea. The westward long-isobath propagation of density fronts caused by nonlinear advection is likely to be the dominant process on the shelves of the Antarctic Continent.

4.5.3 Cold Water Pool in the Middle Atlantic Bight

In the Middle Atlantic Bight, bottom water movement is present in the cold water pool and the outflow of Gulf of Maine Intermediate Water in spring and summer. For a cooling rate of -250 Watts/$m^2$ in the coldest period of December and January (Beardsley and Boicourt, 1981),

the density accumulation in the water column will be 2.4 $gm/cm^2$ after 47 days (Table 4.2). The density perturbation is then $0.48 \times 10^{-3}$ $gm/cm^3$ in 50 m of water. The parameter $\mu$, which determines the behavior of Burgers' equation, is 25 for a longshore cooling range of 100 km, so density fronts are expected to form under winter cooling.

Hopkins and Garfield (1979) demonstrated that the Gulf of Maine Intermediate Water could be identified in spring in the Middle Atlantic Bight during the cold years of 1964-1966. This feature can be explained by the model on the outflow of coastal heavy density anomaly (Section 4.4.2). Dense water produced in winter flows out of the Gulf of Maine from the Great South Channel and the Northeast Channel in spring. The accumulation of dense water on the shelf eventually lead to the formation and propagation of density fronts.

Recent observations on the cold pool (Houghton et al., 1981) give supporting evidence on the bottom water movement in the Middle Atlantic Bight in spring and summer. Houghton et al. (1981) analyzed the distribution of minimum temperature water in the Middle Atlantic Bight in 1979. The southwestward propagation of cold bottom water and the existance of strong longshore density gradients were clearly shown by the contour lines of minimum temperature distribution in a map with longshore distance and time as axes. One feature of this illustration was that the location of temperature minimum moved southwestward with variable speed.

Long-isobath density fronts can also be observed in the bottom temperature maps of Bigelow (1933). Figures 4.18a-c, reproduced from Bigelow (1933), illustraste the development of long-isobath temperature

gradients. The successive passage of density fronts can be inferred from monthly variations of bottom temperature at a fixed cross-shelf section along 71°W. Figure 4.19 is reproduced from Chamberlin (1978) and Crist and Chamberlin (1979), which shows the monthly progress of bottom temperature for the years 1974 to 1976. In 1974, bottom water with temperature less than 5° C was present through late February. After a short warm period, a parcel of cold water moved in and stayed for a month. Then the third cold water parcel arrived in April. There was a quiet period in early May. The last cold parcel arrived in late May with temperature about 2° C higher than the earlier ones. The patterns for 1975 and 1976 were similar except that the earlier events were not distinguishable. The last warm event occurred in all three years, although the arrival time was different in each year, mid-May in 1974 and 1976, and mid-July in 1975. Figure 4.20 is the distribution of bottom temperature on the south side of Georges Bank in May 1979 plotted from the data of EG & G (1979). A band of cold bottom water with temperature less than 7°C was present from the Northeast Channel to Nantucket. It is reasonable to suppose that the last event was produced by the water flowing out of the Northeast Channel.

The cold water movement in the Middle Atlantic Bight is generally considered to be caused by advection, independently of the density field. However, linear translative motion produced by longshore mean flow can not explain the formation of strong density gradients in the longshore direction. Figure 18a shows that the density was homogeneous in the longshore direction in February 1929. In April, a strong

longshore density gradient was present off Chesapeake Bay, with a temperature difference of 3°C in 100 km (Figure 18b). Another front appeared off Delaware coast in July 1929 (Figure 18c). Current observations (Beardsley et al., 1976) show that the current in that region is generally southward and stronger than the current further north. There is no convergence in the longshore current to form strong longshore density gradients. The heating from the atmosphere is of a much larger length scale and cannot be the cause of these gradients. Because longshore density fronts can be observed thoughout spring and summer, it is unlikely that the slope water will produce such a consistent feature at different locations over a period of several months.

Figure 4.19 suggests that fronts propagate southwestward along the coast instead of being formed locally. The associated strong density gradient is maintained throughout summer without being diffused away. It is not likely that the density front would survive strong tides and other high frequency disturbances on the south side of Georges Bank, were it carried southwestward by mean flow independent of the density field. The explanation for the persistence of density gradients has to involve the self-advection of density field, i.e. the propagation of shock-wave like density fronts. The nonlinear advection process in the present model shows that a density front may intensify under certain circumstances.

Another feature of the model is that the propagation speed need not to be the same as the flow velocity, and may not be constant through spring and summer. Figure 4.14 agrees with the distribution of temperature minimum observed by Houghton et al. (1981). In July and

August, the nearly stationary location of the observed longshore temperature minimum in the south can be predicted by the model. Houghton et al. (1981) also mentioned a strong longshore temperature gradient at the Hudson Canyon with a much slower propagation speed. One explanation could be the interruption of longshore bottom velocity by the canyon topography. The self-advection process will resume only after enough cold water has diffused across the canyon. This would explain the slower propagation speed of the temperature front than the speed measured by current meters.

4.6 Summary

In this chapter, we have investigated the density-driven flow over topography. It is found that the interaction between the long-isobath bottom density difference and the bottom topography is dynamically important. Away from coastal boundary layers, a near-bottom dense water blob will move in the direction of Kelvin wave propagation. For a light water blob, the direction of propagation is reversed. Strong density fronts may appear in the forward face of the density perturbation. This is the same process as the shock wave formation in Burgers' equation.

Self-advection can also be produced by river discharge at the coast under winder conditions. The light water will move inside a coastal boundary layer along the coast in the direction of Kelvin wave propagation. For dense water discharge, the movement of density perturbation is no longer along the coast. The density perturbation moves offshore initially and then propagates as a dense water blob in the mid-shelf region.

This model can be used to explain the bottom water movement in the

Adriatic Sea, the Antarctic Continent, and the Middle Atlantic Bight. The predictions of the model agree qualitatively with the observed bottom water movements. The model also gives correctly the speed of front propagation.

Figure 4.1 Schematic diagram demonstrating the solution of Burgers' equation. The density distribution at $t = 0$ is a delta function located at $y = 0$.

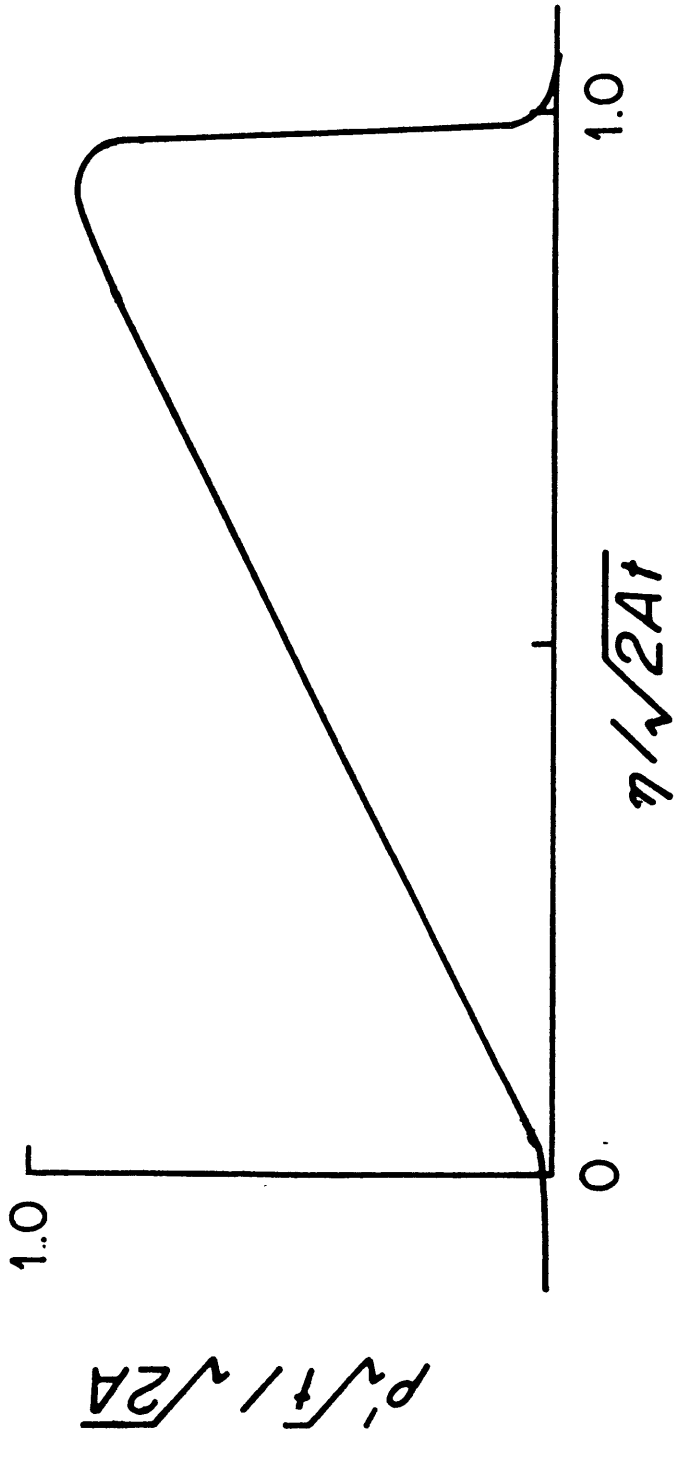

1.0
0
1.0
$\eta/\sqrt{2At}$
$\rho_i/\rho/\sqrt{2A}$

Figure 4.2 Schematic diagram showing solutions of Burgers' equation at different values of time with an initial (t = 0) delta function disturbance located at y = 0. A positive disturbance is shown by solid lines, and a negative one by dashed lines.

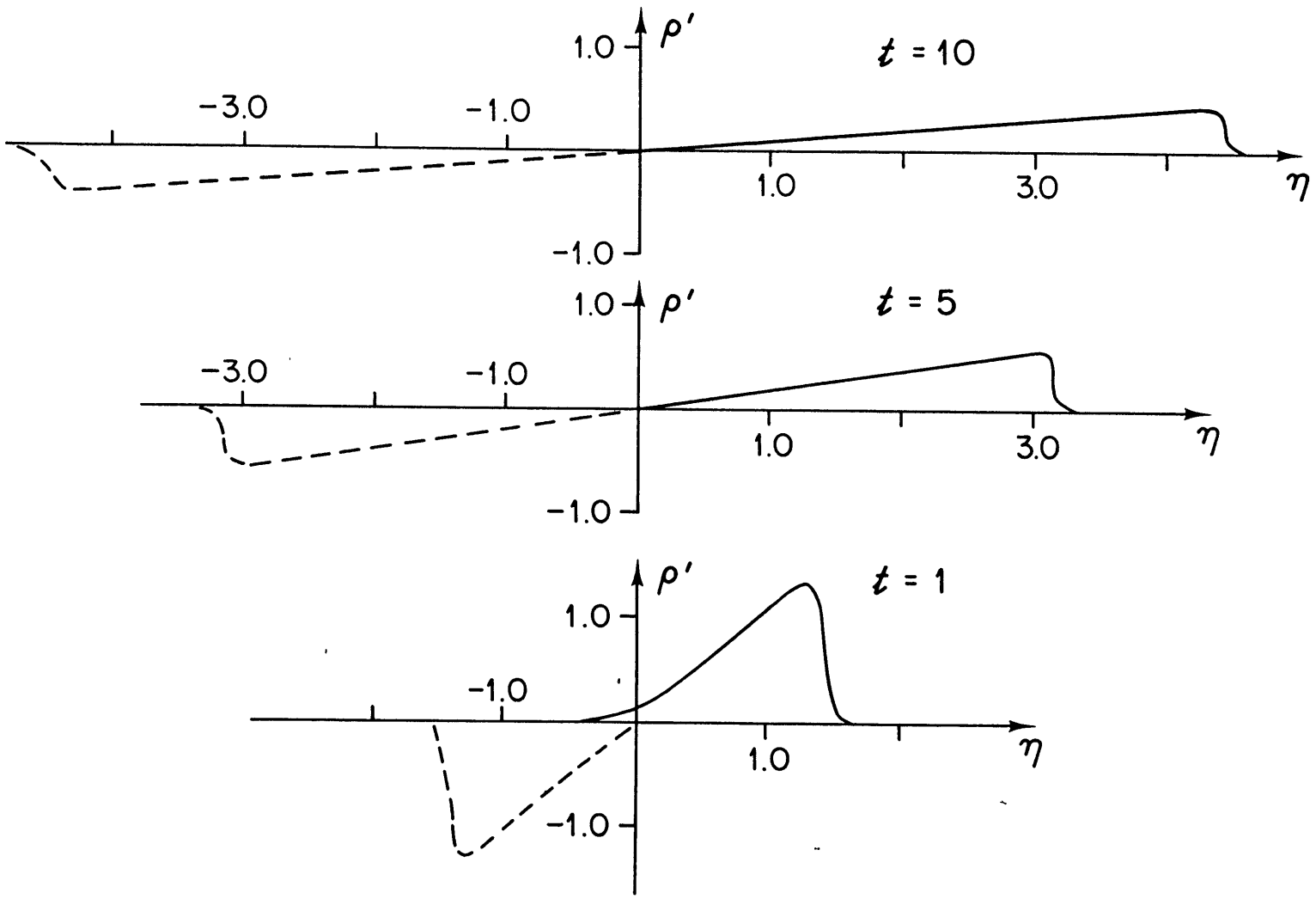

ρ'
t = 10
1.0
-1.0
-3.0
-1.0
1.0
3.0
η
ρ'
t = 5
1.0
-1.0
-3.0
-1.0
1.0
3.0
η
ρ'
t = 1
1.0
-1.0
-1.0
1.0
η

Figure 4.3a Distributions of density (left) and bottom velocity (right) at $t = 1$ produced by buoyancy flux located at $-1 < y < 0$. The parameters are $R_0/\gamma = 2.5$ and $\gamma = 0.025$. The density field is contoured with an interval of 0.25.

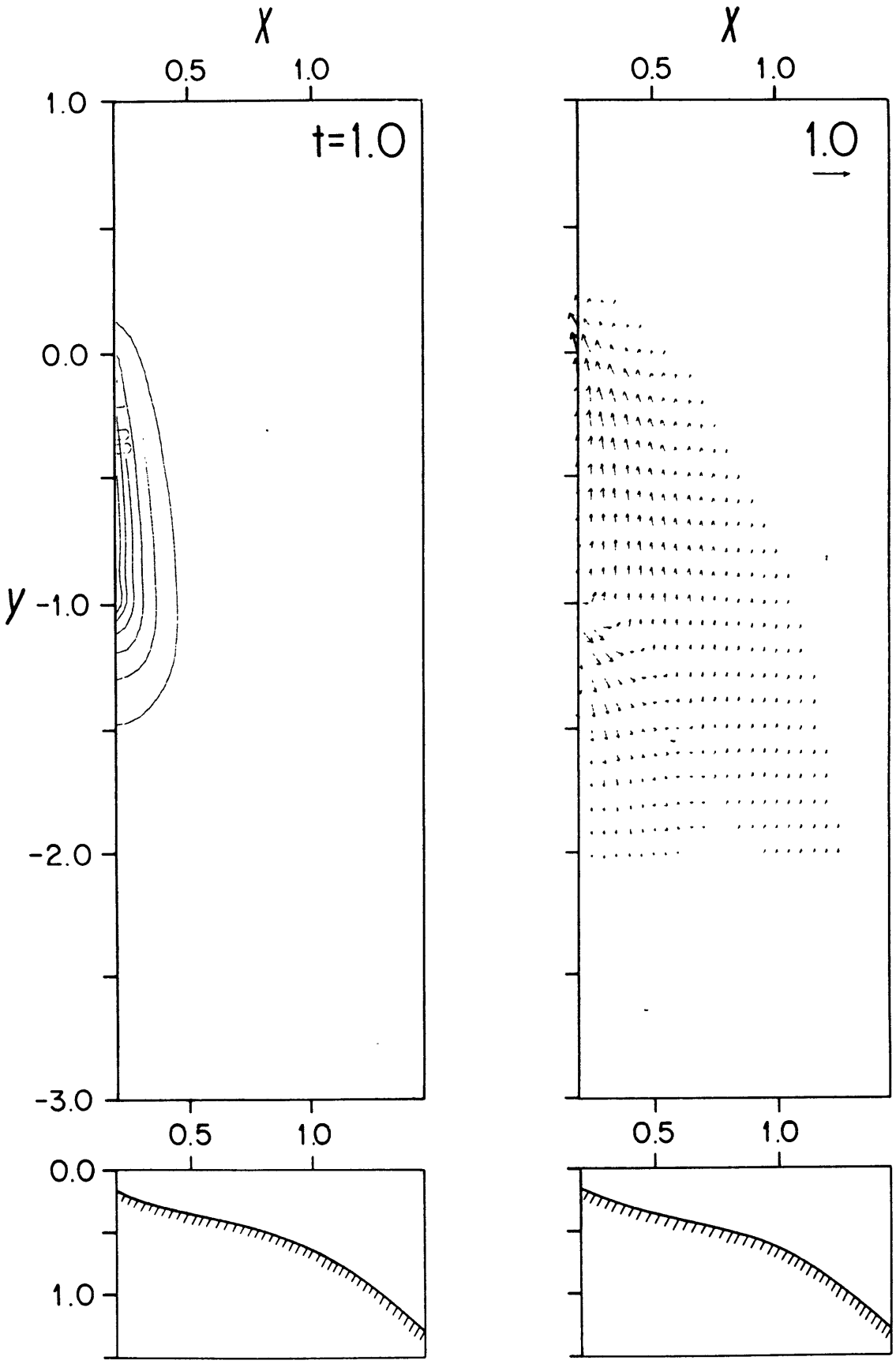

X
0.5
1.0
1.0
t=1.0
0.0
y -1.0
-2.0
-3.0
0.5
1.0
0.0
1.0
X
0.5
1.0
1.0
0.5
1.0

Figure 4.3b Distributions of density (left) and bottom velocity (right) at $t = 5$ produced by buoyancy flux located at $-1 < y < 0$. The parameters are $R_0/\gamma = 2.5$ and $\gamma = 0.025$. The density field is contoured with an interval of 0.25.

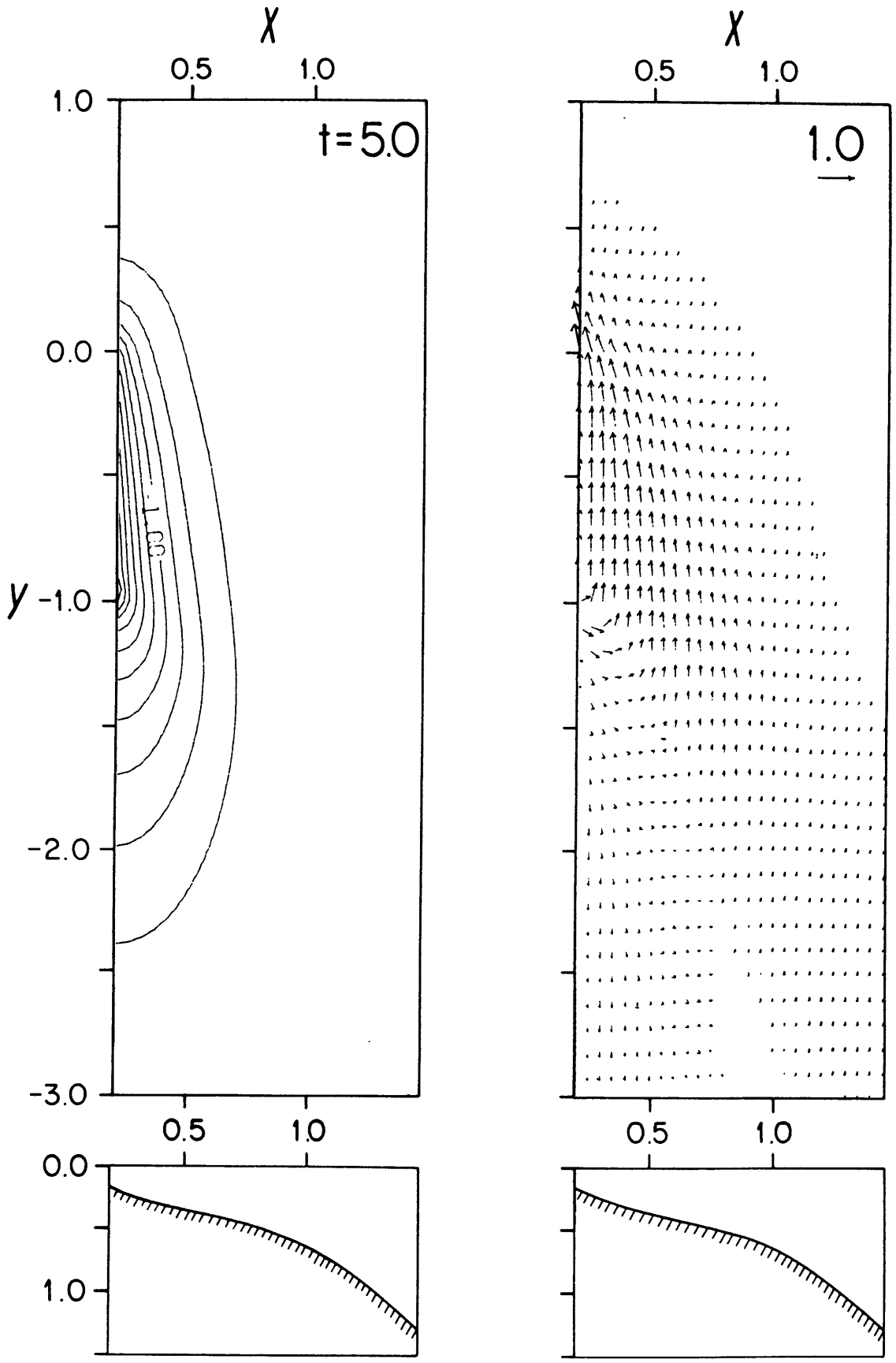

X
0.5
1.0
1.0
t=5.0
0.0
y -1.0
-2.0
-3.0
0.5
1.0
0.0
1.0
X
0.5
1.0
1.0
0.5
1.0

Figure 4.3c Distributions of density (left) and bottom velocity (right) at $t = 10$ produced by buoyancy flux located at $-1 < y < 0$. The parameters are $R_0/\gamma = 2.5$ and $\gamma = 0.025$. The density field is contoured with an interval of 0.25.

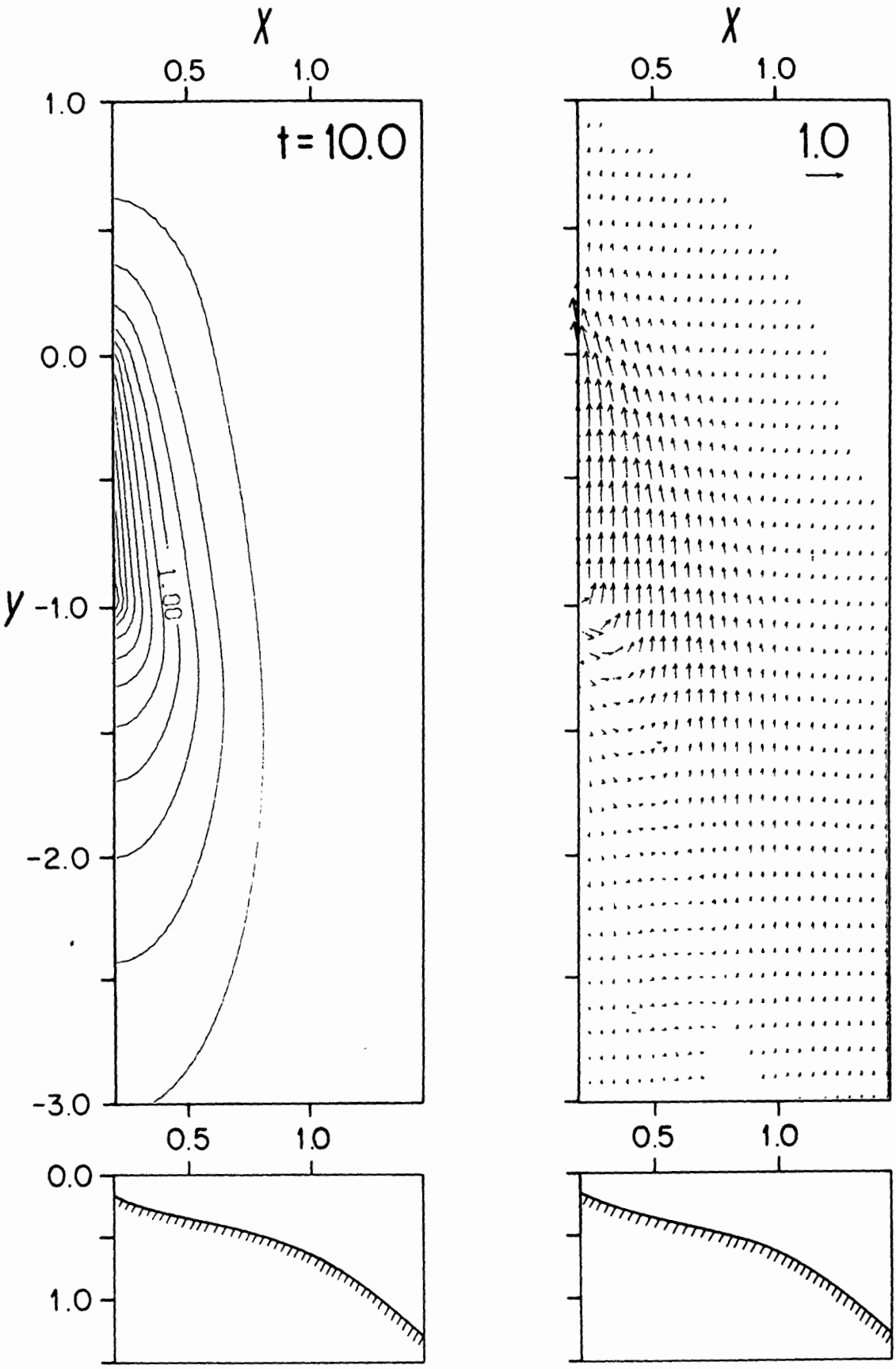

X
0.5
1.0
1.0
t = 10.0
0.0
y -1.0
-2.0
-3.0
1.00
0.5
1.0
0.0
1.0
X
0.5
1.0
1.0
0.5
1.0
0.0
1.0

Figure 4.4 Evolution of the density distribution at $y = -1$ as a function of time.

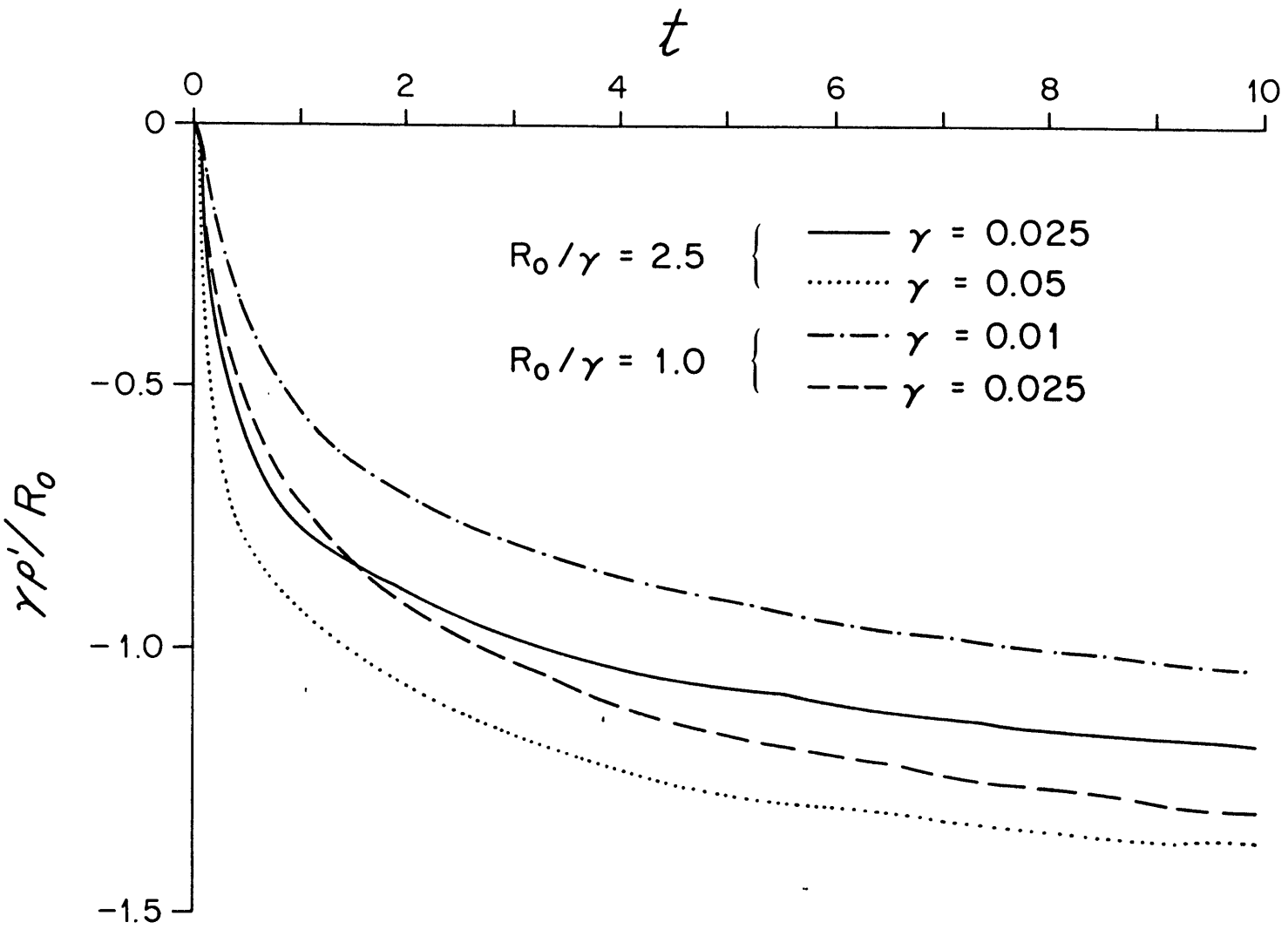

t
0
2
4
6
8
10
0
−0.5
−1.0
−1.5
γρ'/R₀
R₀/γ = 2.5
γ = 0.025
γ = 0.05
R₀/γ = 1.0
γ = 0.01
γ = 0.025

Figure 4.5 Longshore density distribution along the x = 0.3 isobath at different values of time.

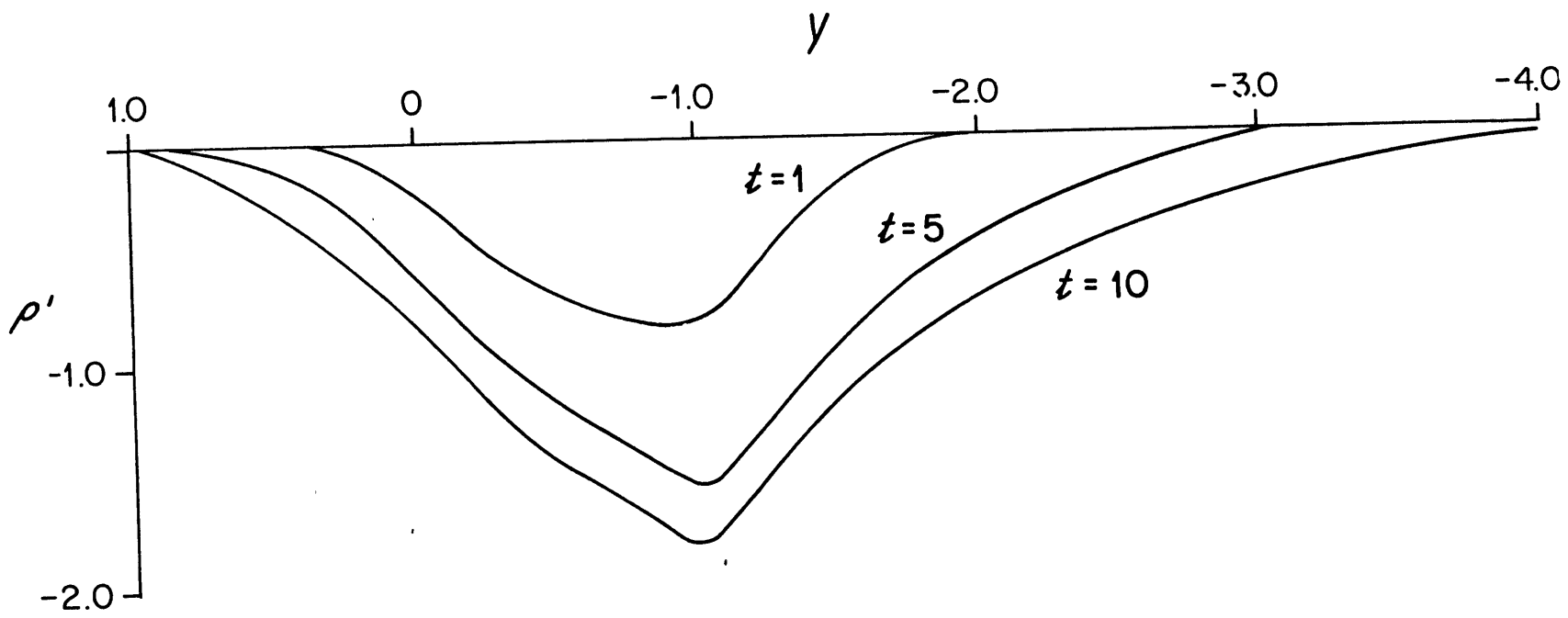

y
1.0
0
-1.0
-2.0
-3.0
-4.0
t = 1
t = 5
t = 10
ρ'
-1.0
-2.0

Figure 4.6 Longshore density distribution along the x = 0.3 isobath at t = 10 for different values of $\gamma$

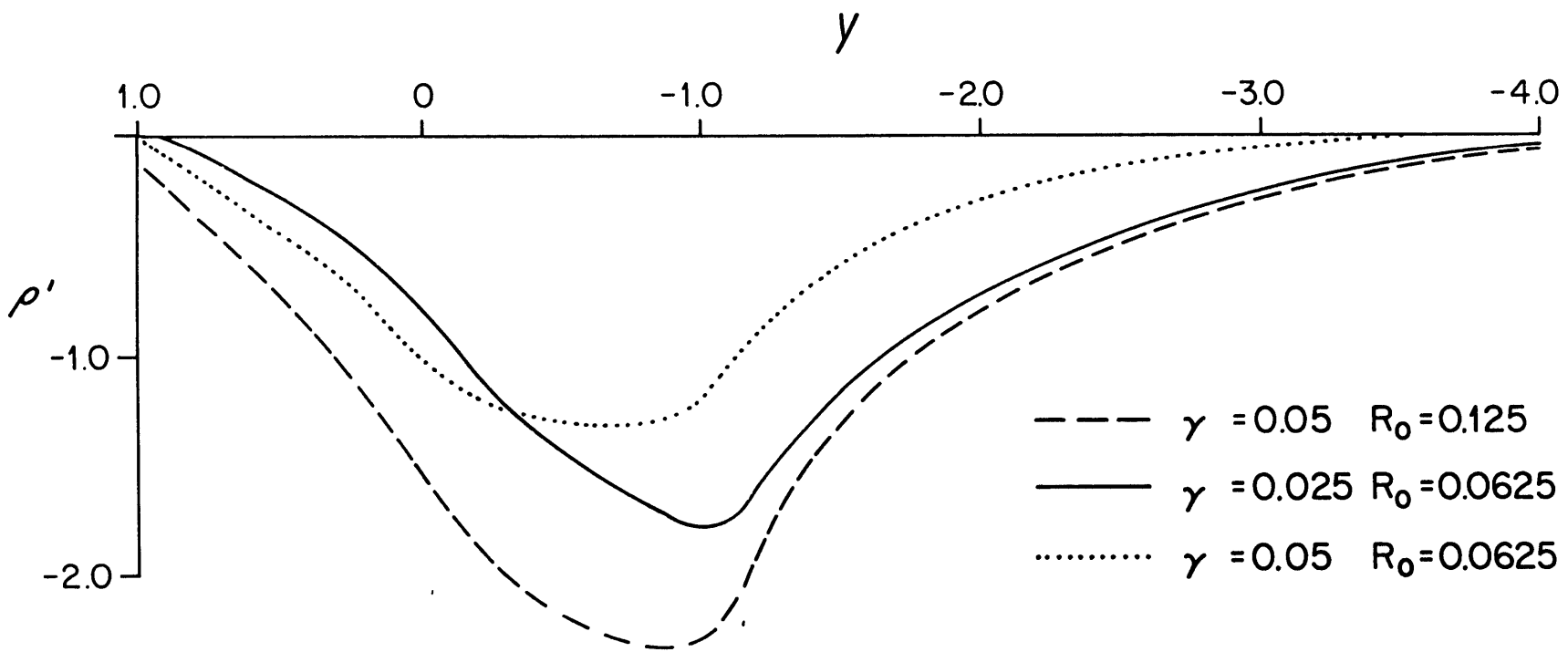

y
1.0
0
-1.0
-2.0
-3.0
-4.0
ρ'
-1.0
-2.0
γ =0.05 R0=0.125
γ =0.025 R0=0.0625
γ =0.05 R0=0.0625

Figure 4.7 Longshore density distribution along the $x = 0.3$ isobath at $t = 10$ for different values of $R_0/\gamma$ with $\gamma = 0.025$. The density is scaled by $R_0/\gamma$.

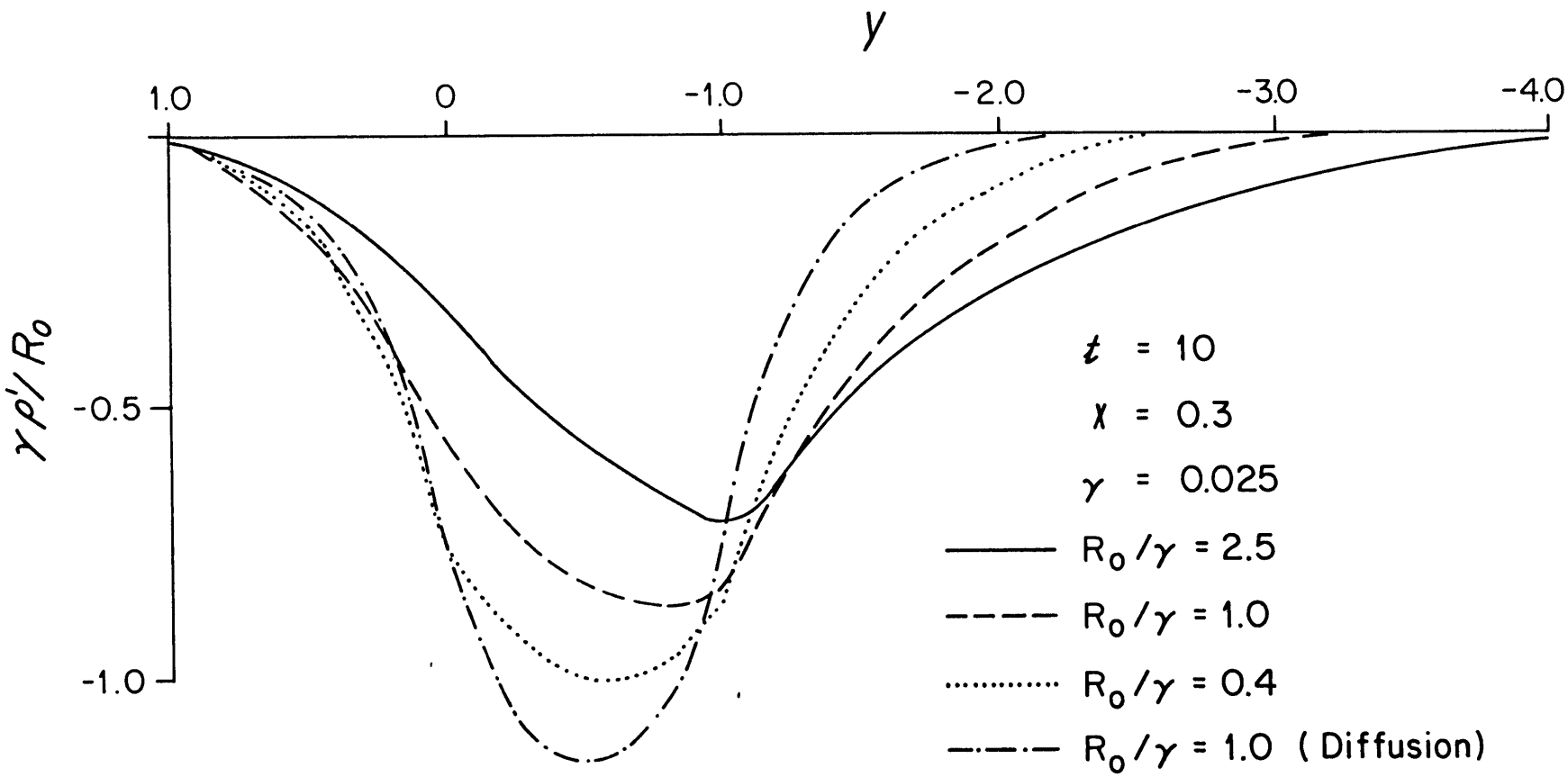

y
1.0
0
-1.0
-2.0
-3.0
-4.0
γρ'/R0
-0.5
-1.0
t = 10
χ = 0.3
γ = 0.025
R0/γ = 2.5
R0/γ = 1.0
R0/γ = 0.4
R0/γ = 1.0 ( Diffusion)

Figure 4.8a Distributions of density (left) and bottom velocity (right) at $t = 1$ with forcing from a coastal density source locasted at $-1 < y < 0$.

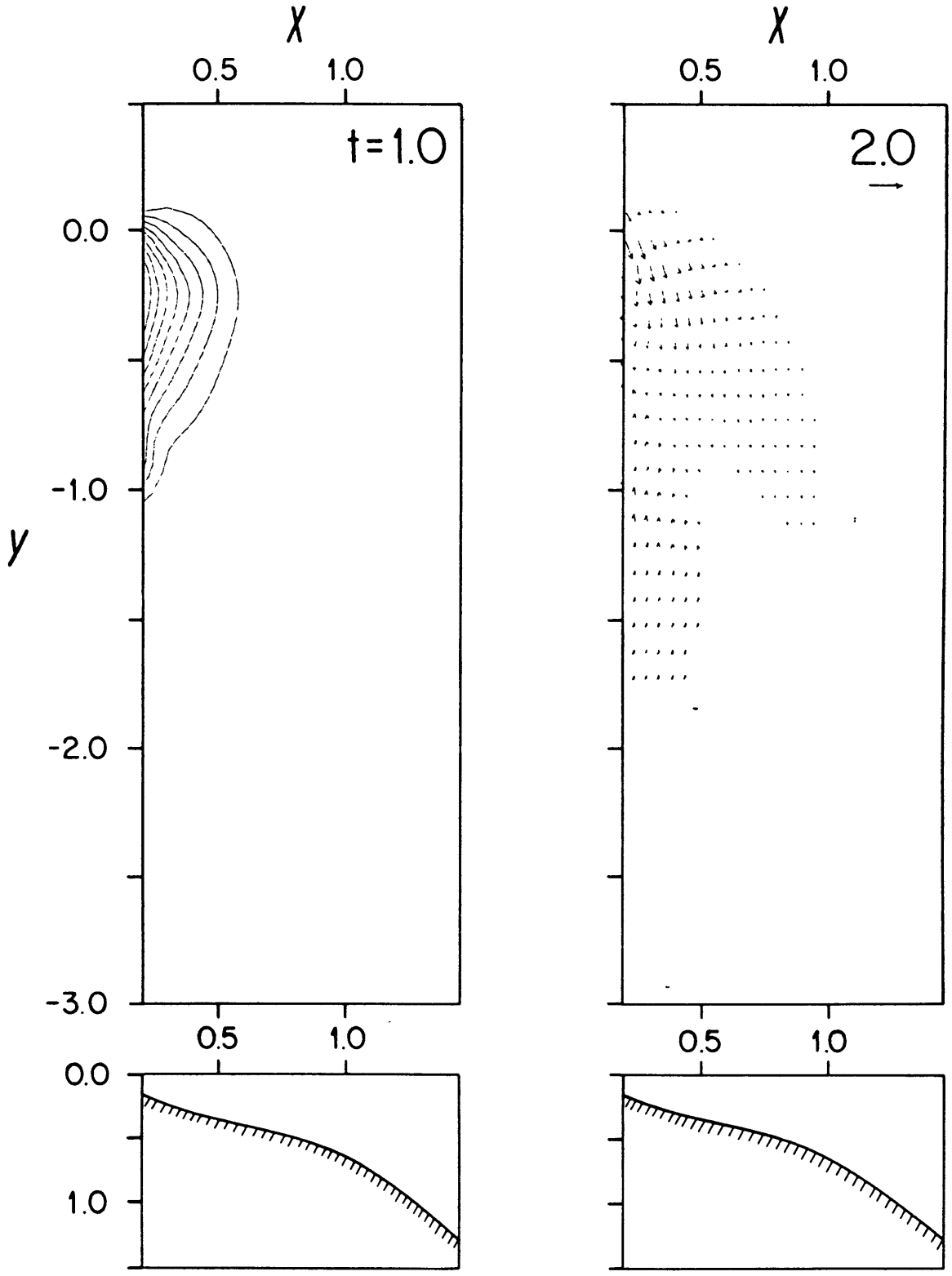

X
0.5
1.0
t=1.0
2.0
0.0
-1.0
-2.0
-3.0
y
0.5
1.0
0.0
1.0
0.5
1.0
0.0
1.0

Figure 4.8b Distributions of density (left) and bottom velocity (right) at $t = 5$ with forcing from a coastal density source located at $-1 < y < 0$.

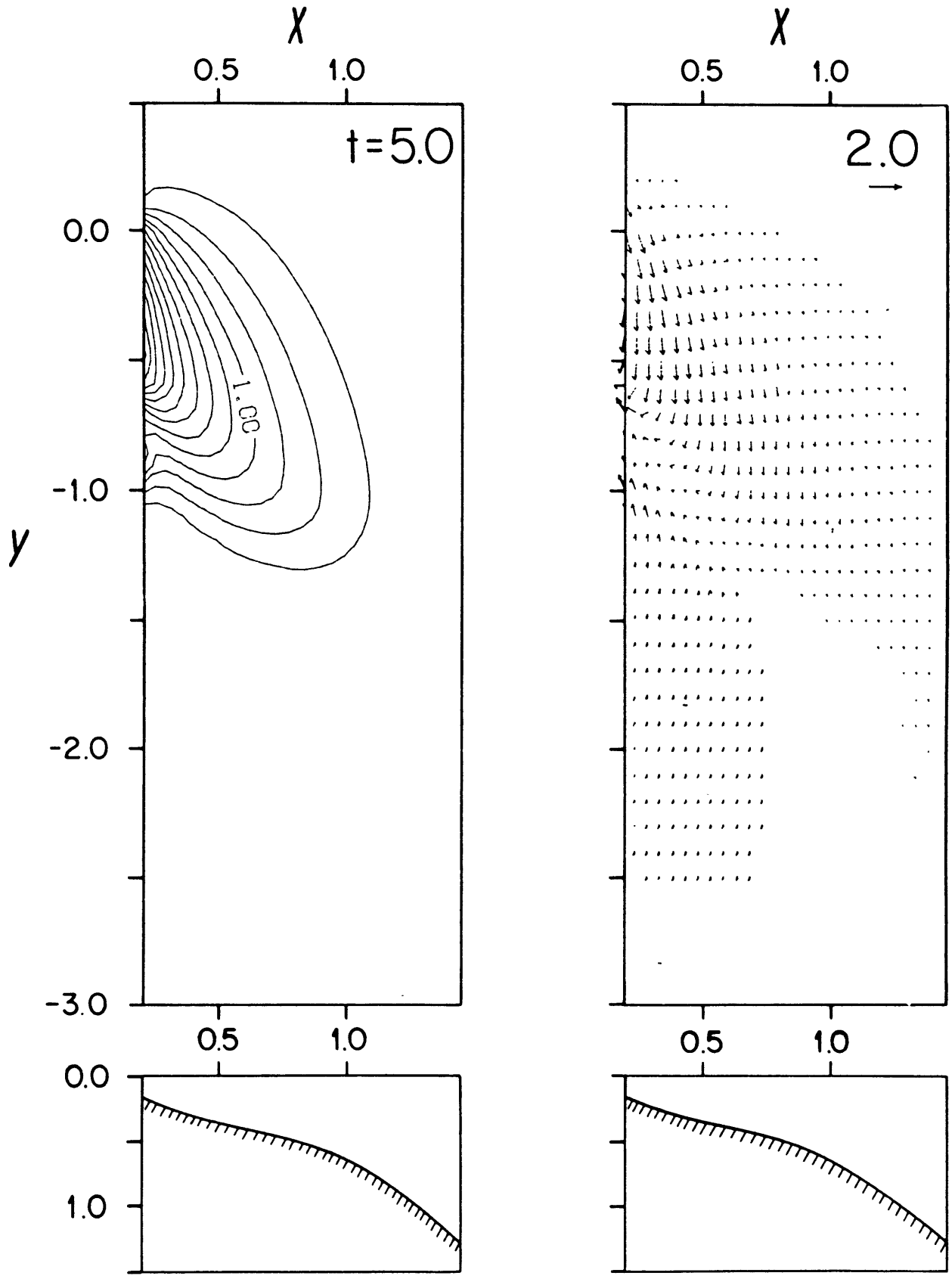

X
0.5
1.0
t=5.0
0.0
-1.0
-2.0
-3.0
y
1.00
X
0.5
1.0
2.0
0.5
1.0
0.0
1.0
0.5
1.0

Figure 4.8c Distributions of density (left) and bottom velocity (right) at t = 10 with forcing from a coastal density source located at $-1 < y < 0$.

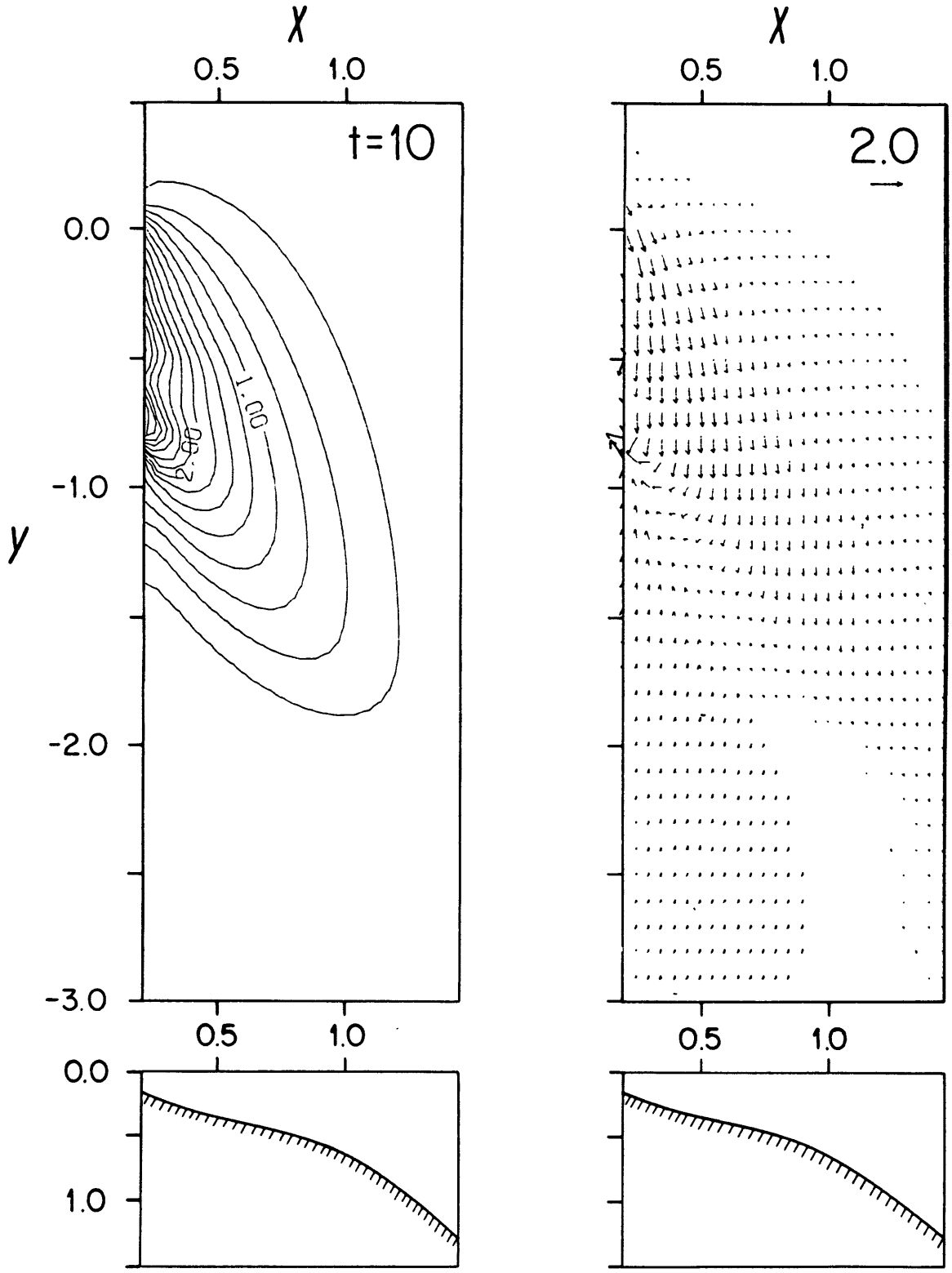

X
0.5
1.0
t=10
0.0
-1.0
-2.0
-3.0
y
.99
1.00
0.5
1.0
0.0
1.0
X
0.5
1.0
2.0
0.5
1.0

Figure 4.8d Distributions of density (left) and bottom velocity (right) at $t = 15$ with forcing from a coastal density source located at $-1 < y < 0$.

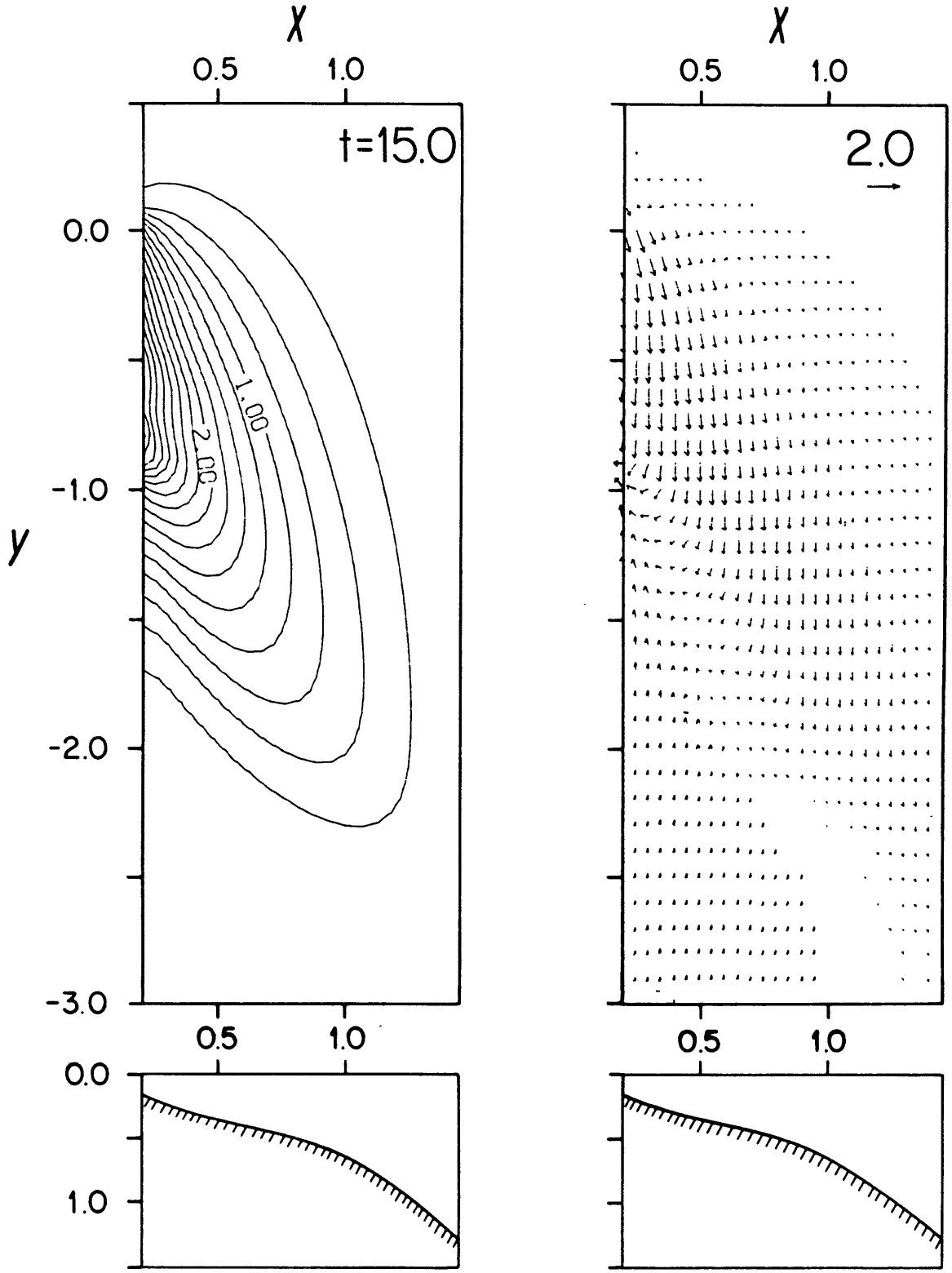

X
0.5
1.0
t=15.0
0.0
-1.0
-2.0
-3.0
y
1.00
2.00
0.5
1.0
0.0
1.0
X
0.5
1.0
2.0
0.5
1.0

Figure 4.9 Contour plot of longshore density distribution along the $x = 2.5$ isobath on the y-t plane. The forcing is a coastal density source at $-1.0 < y < 0$. Dashed line shows the location of density maximum along the isobath.

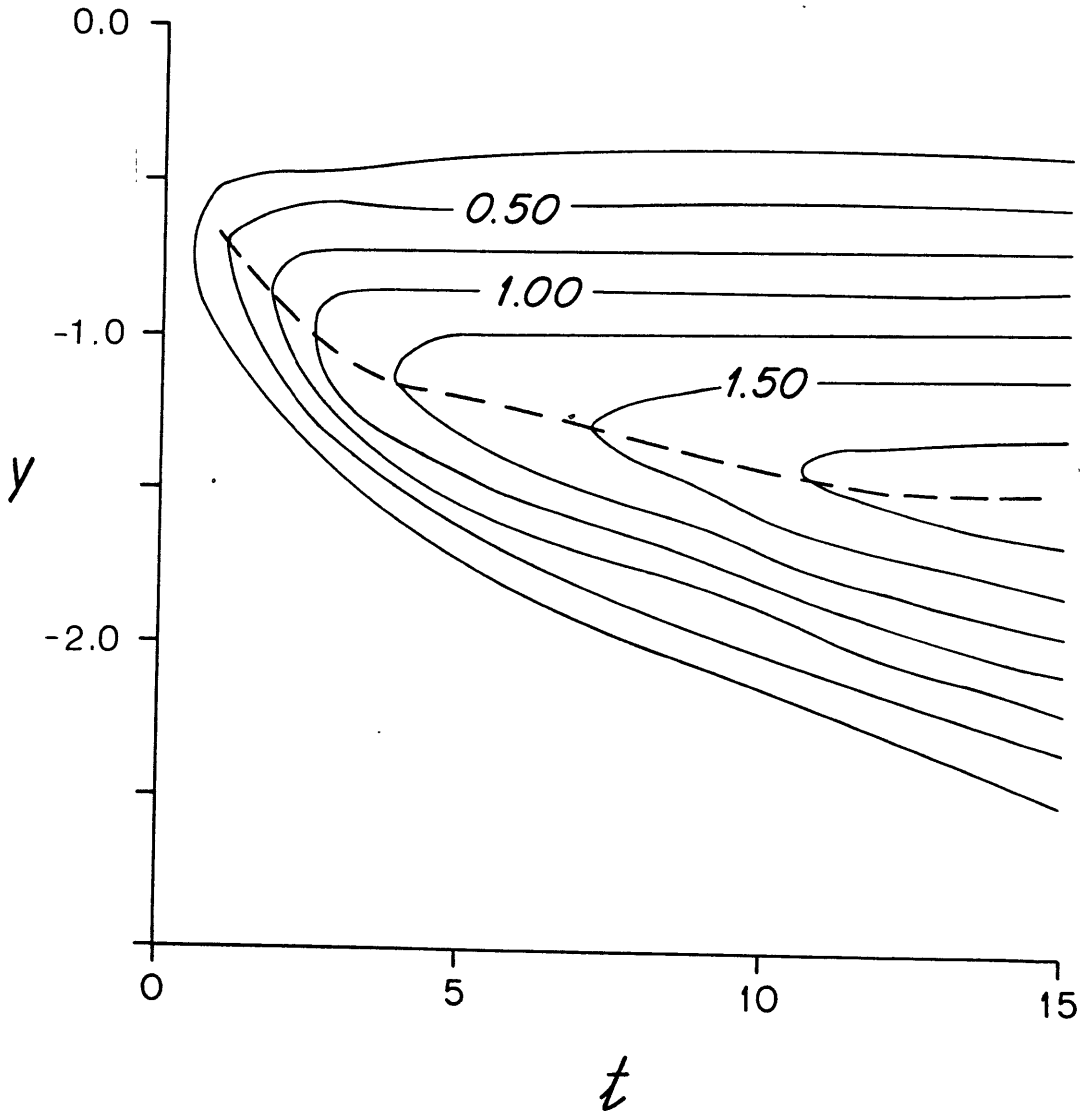

0.0
-1.0
-2.0
y
0.50
1.00
1.50
0
5
10
15
t

Figure 4.10a Contour plot of density field at t = 1 produced by surface cooling. The forcing is applied at $-1.0 < y < 0$ from t = 0 to t = 2.

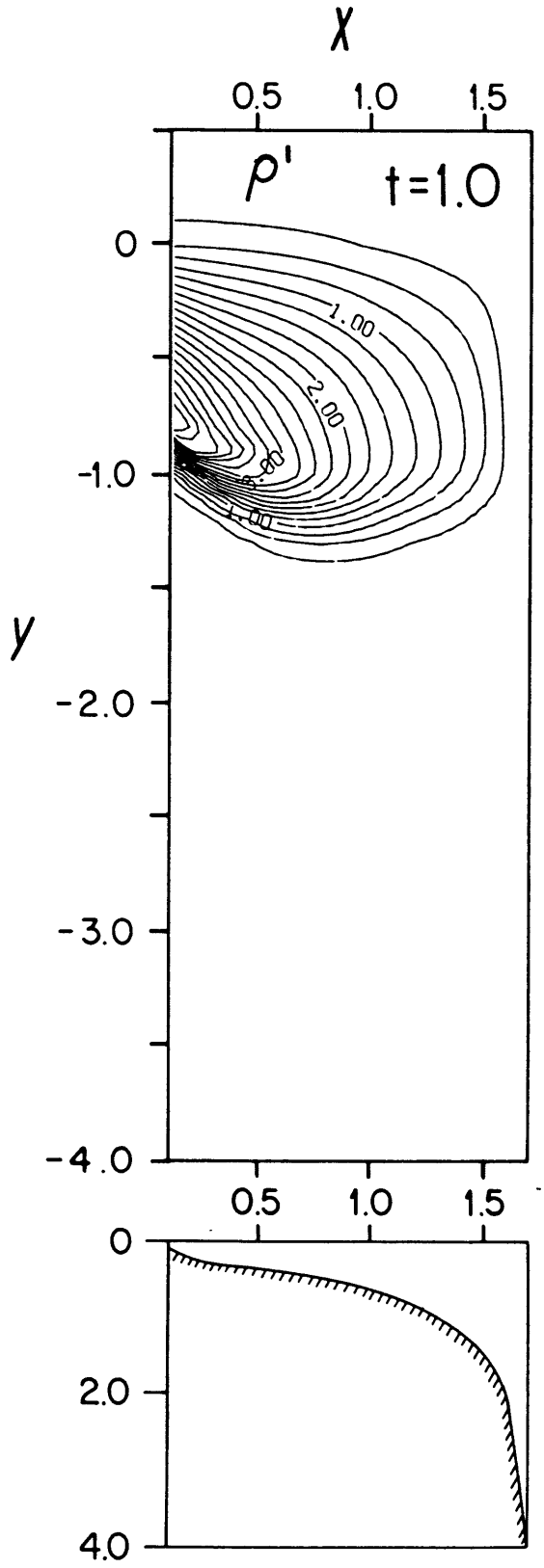

X
0.5
1.0
1.5
ρ'
t=1.0
0
-1.0
-2.0
-3.0
-4.0
y
1.00
2.00
.50
1.00
0
2.0
4.0

Figure 4.10b Contour plot of density field at t = 2 produced by surface cooling. The forcing is applied at $-1.0 < y < 0$ from t = 0 to t = 2.

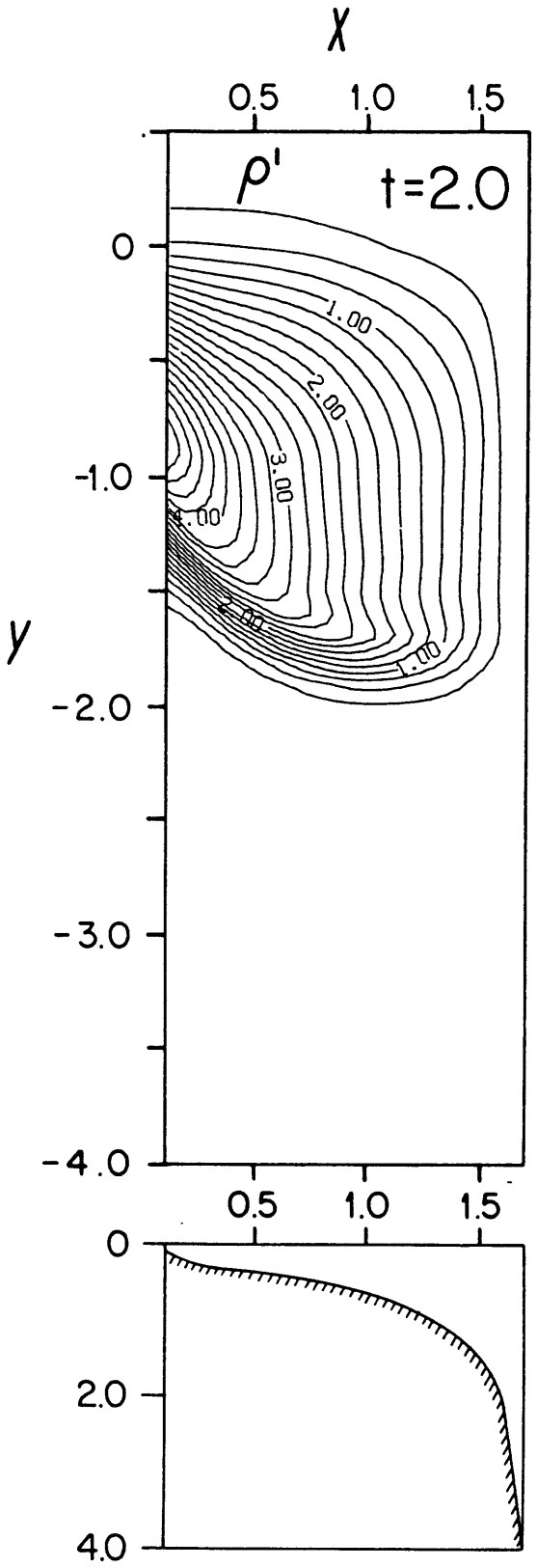

X
0.5
1.0
1.5
ρ'
t=2.0
0
-1.0
-2.0
-3.0
-4.0
y
1.00
2.00
3.00
4.00
2.00
1.00
0.5
1.0
1.5
0
2.0
4.0

Figure 4.10c Contour plot of density field at t = 5 produced by surface cooling. The forcing is applied at $-1.0 < y < 0$ from t = 0 to t = 2.

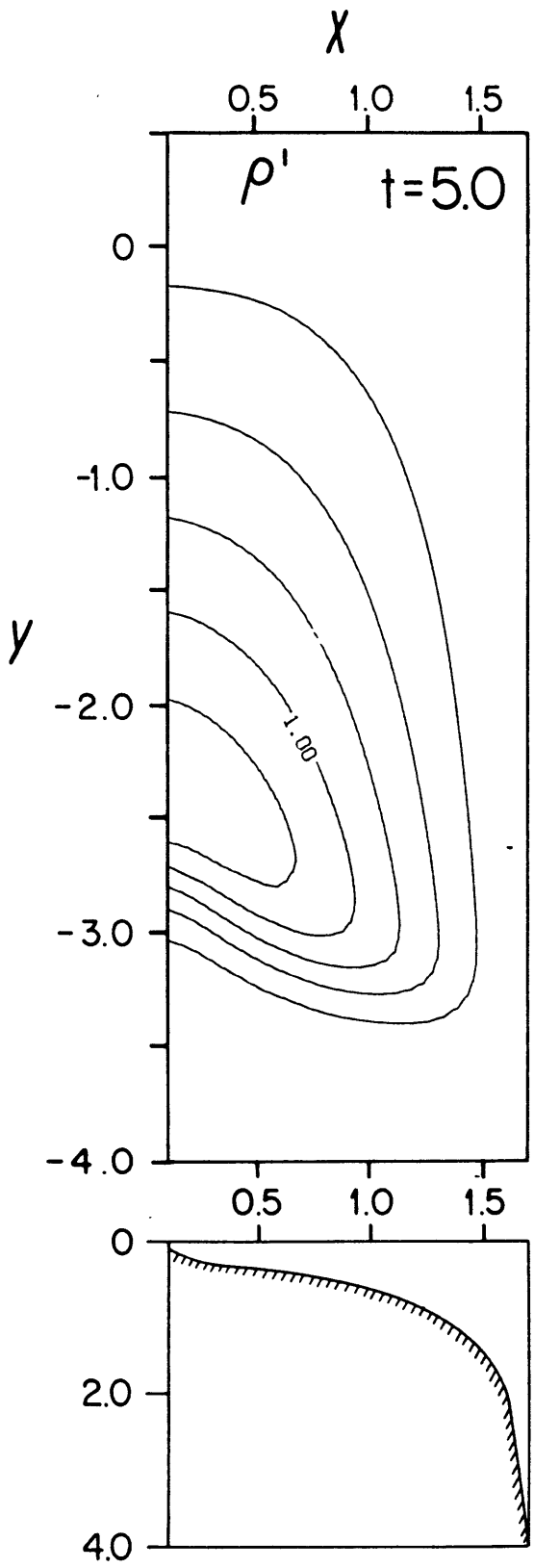

X
0.5
1.0
1.5
ρ'
t=5.0
0
-1.0
y
-2.0
1.00
-3.0
-4.0
0.5
1.0
1.5
0
2.0
4.0

Figure 4.11a Magnitude of the longshore bottom velocity at t = 1, corresponding to the density field in Figure 4.10a.

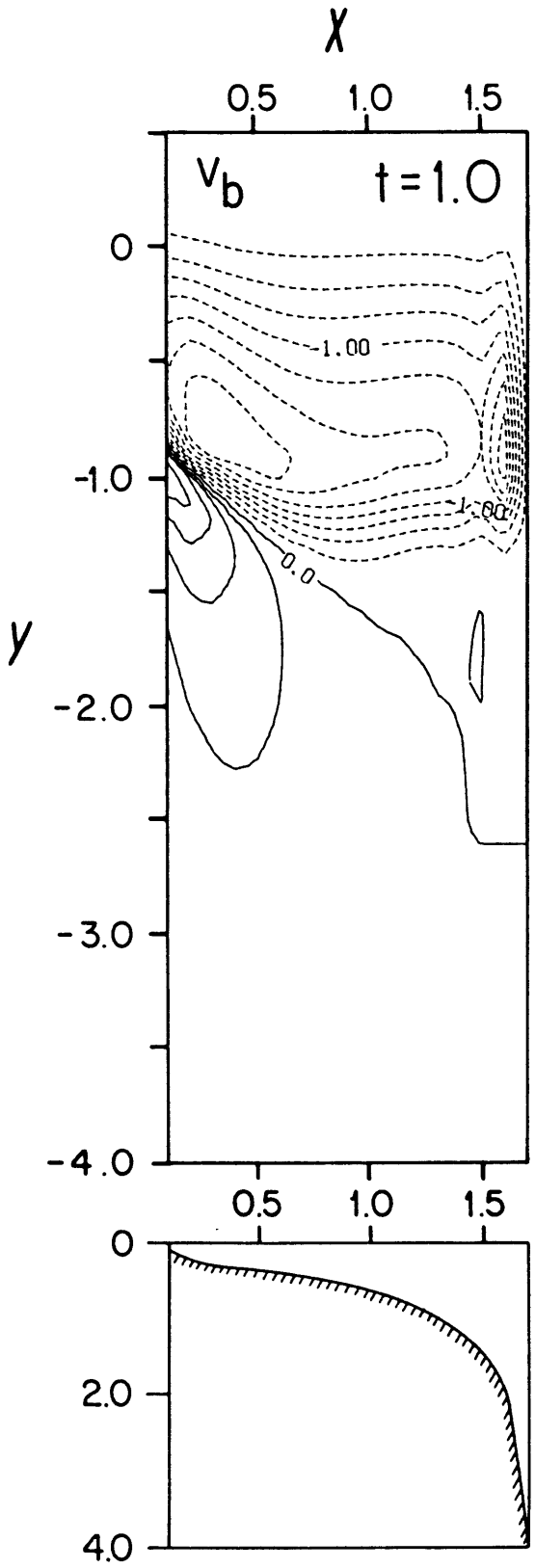

X
0.5
1.0
1.5
$V_b$
t=1.0
0
-1.0
-2.0
-3.0
-4.0
y
-1.00
-1.00
0.0
0.5
1.0
1.5
0
2.0
4.0

Figure 4.11b Magnitude of the longshore bottom velocity at t = 2, corresponding to the density field in Figure 4.10b.

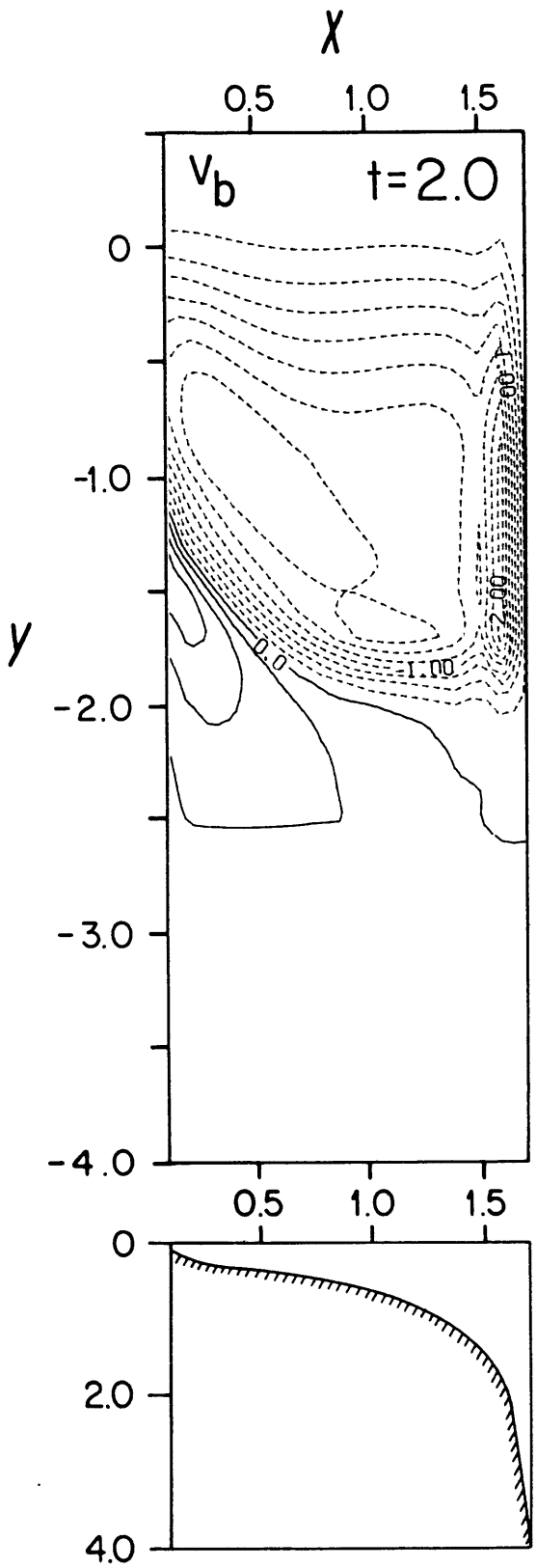

X
0.5
1.0
1.5
$V_b$
t=2.0
0
-1.0
-2.0
-3.0
-4.0
y
-1.00
-2.00
0.0
1.00
0.5
1.0
1.5
0
2.0
4.0

Figure 4.11c Magnitude of the longshore bottom velocity at t = 5, corresponding to the density field in Figure 4.10c.

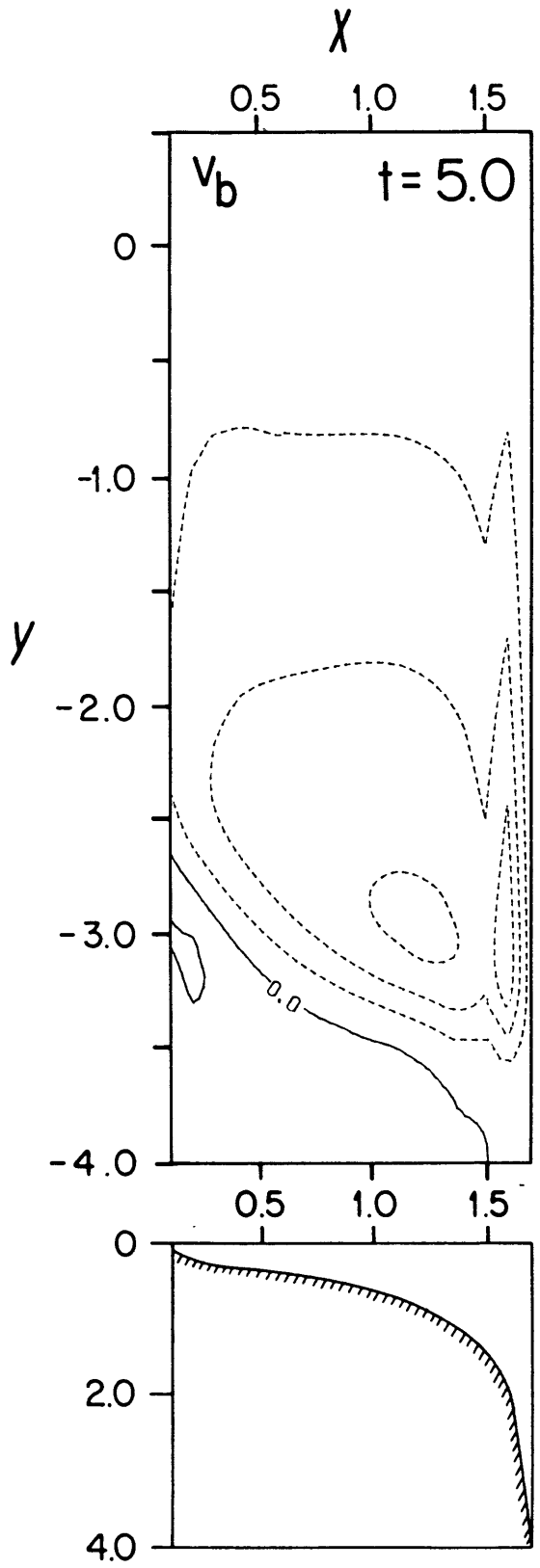

X
0.5
1.0
1.5
$V_b$
t= 5.0
0
-1.0
y
-2.0
-3.0
0.0
-4.0
0.5
1.0
1.5
0
2.0
4.0

Figure 4.12a Magnitude of the offshore bottom velocity at t = 1, corresponding to the density field in Figure 4.10a.

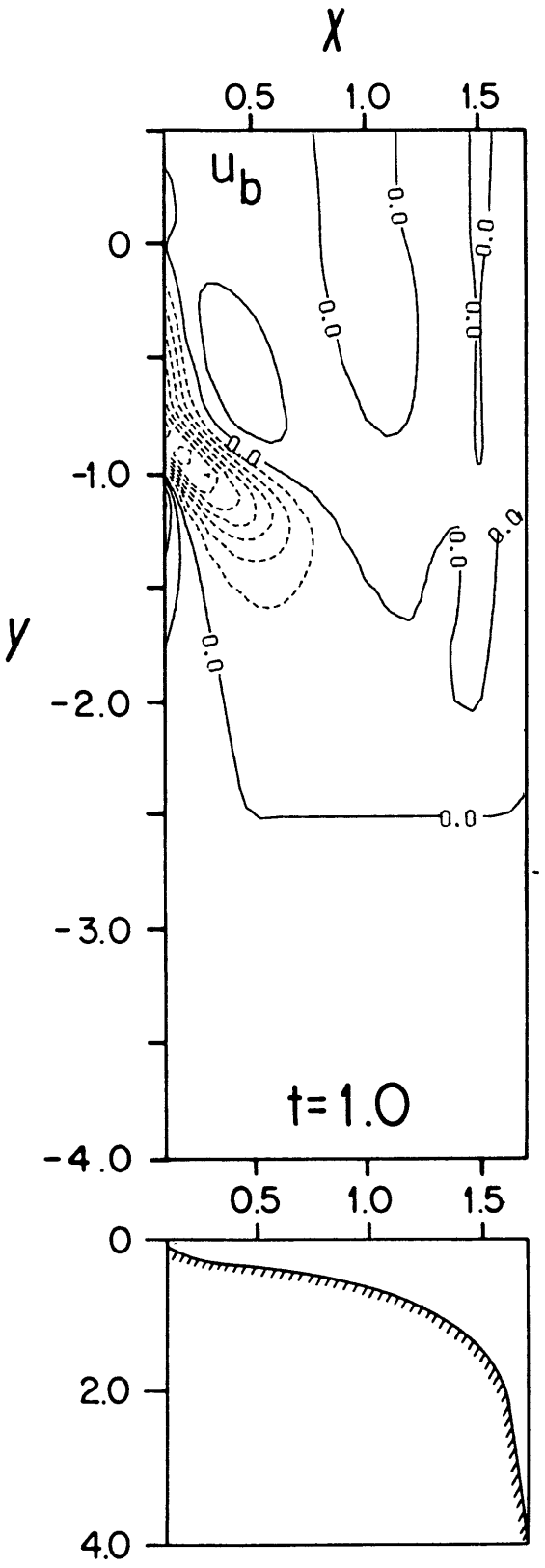

x
0.5
1.0
1.5
$u_b$
0
-1.0
-2.0
-3.0
-4.0
y
0.0
t=1.0
0.5
1.0
1.5
0
2.0
4.0

Figure 4.12b Magnitude of the offshore bottom velocity at t = 2, corresponding to the density field in Figure 4.10b.

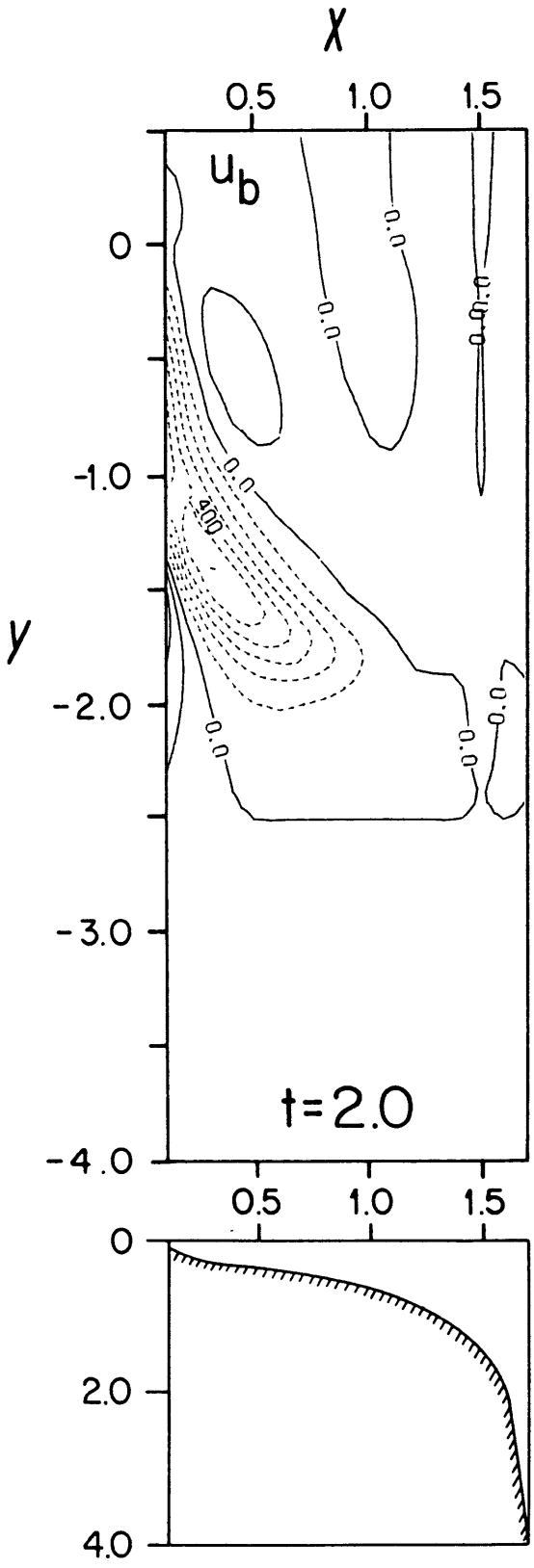

x
0.5
1.0
1.5
$u_b$
0
-1.0
-2.0
-3.0
-4.0
y
0.0
-.400
t=2.0
0
2.0
4.0

Figure 4.12c Magnitude of the offshore bottom velocity at t = 5, corresponding to the density field in Figure 4.10c.

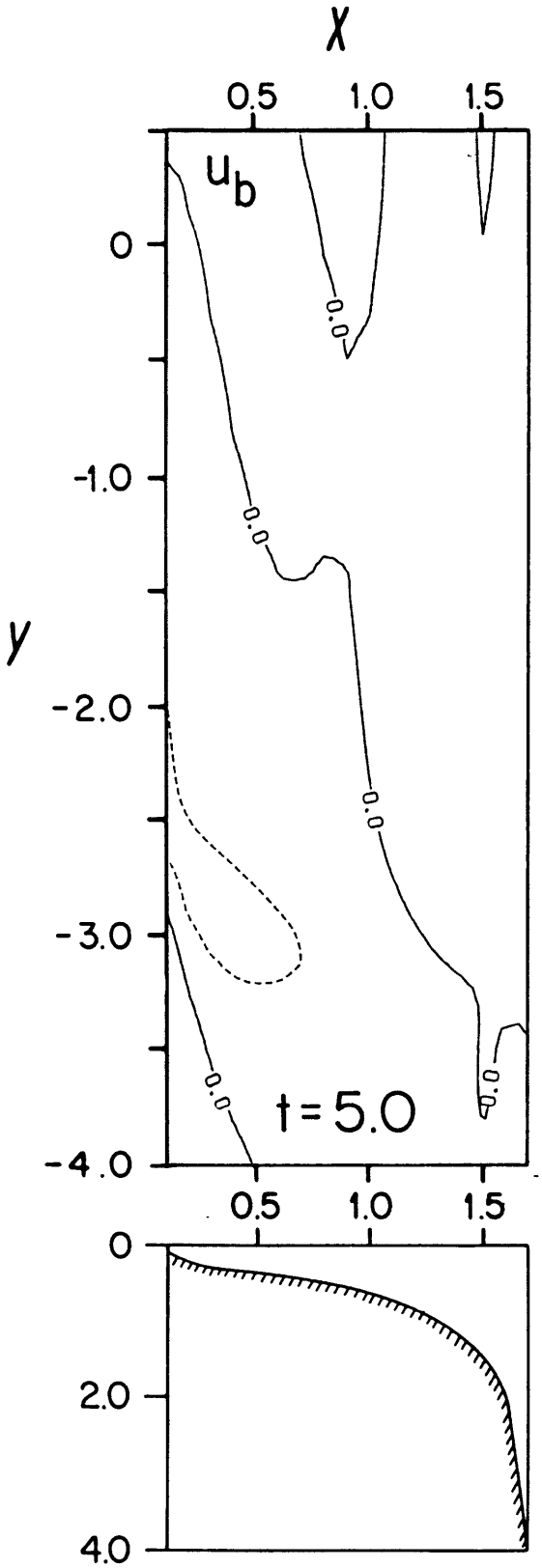

X
0.5
1.0
1.5
$u_b$
0
-1.0
-2.0
-3.0
-4.0
y
0.0
0.0
0.0
0.0
t=5.0
0.5
1.0
1.5
0
2.0
4.0

Figure 4.13 Distribution of density along the $x = 1.0$ isobath for cooling with parameters $T = 2$, $L_y = 1$, and $\gamma = 0.05$.

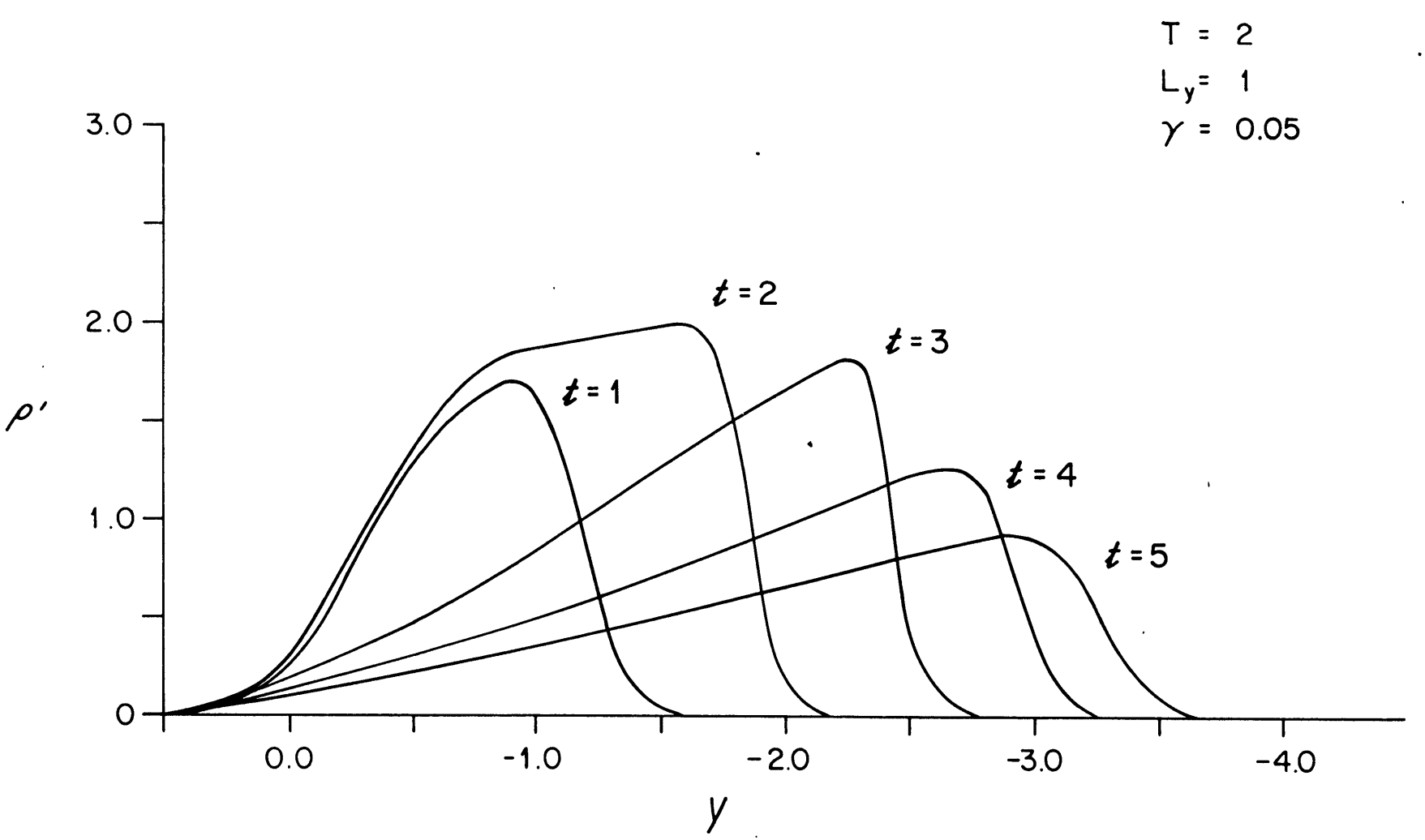

T = 2
$L_y$ = 1
$\gamma$ = 0.05
3.0
2.0
1.0
0
$\rho'$
$t$ = 2
$t$ = 3
$t$ = 1
$t$ = 4
$t$ = 5
0.0
-1.0
-2.0
-3.0
-4.0
$y$

Figure 4.14 Contour plot of longshore density distribution along the $x = 1.0$ isobath on the y-t plane. Surface cooling is applied between $y = -1$ and 0 from $t = 0$ to 2. The parameter $\gamma$ is 0.1. Dashed line shows the location of temperature minimum along this isobath.

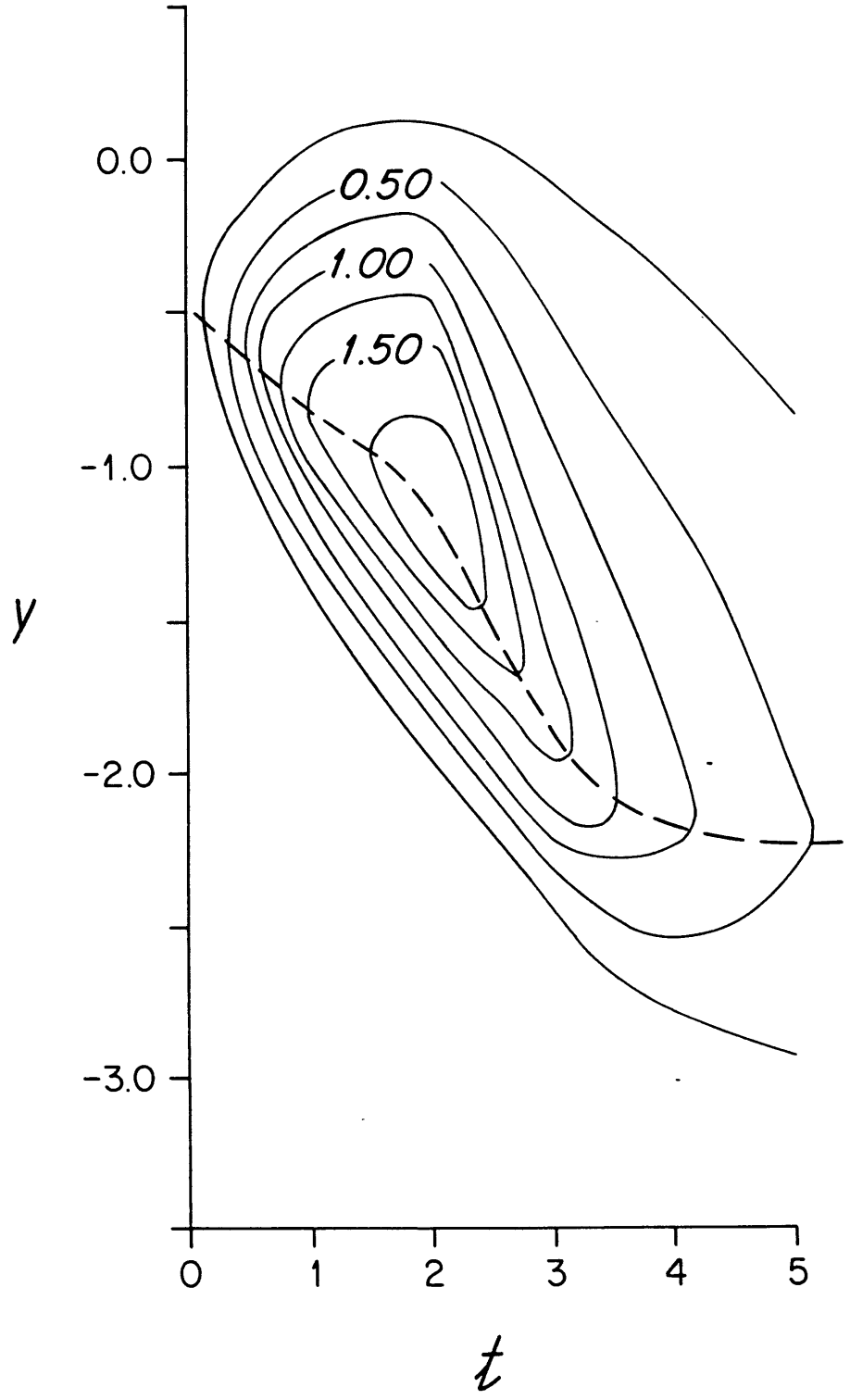

0.0
-1.0
-2.0
-3.0
y
0.50
1.00
1.50
0
1
2
3
4
5
t

Figure 4.15 Longhsore density distribution along the $x = 1.0$ isobath for cooling with parameters $T = 2$, $L_y = 1$, and $\gamma = 0.1$.

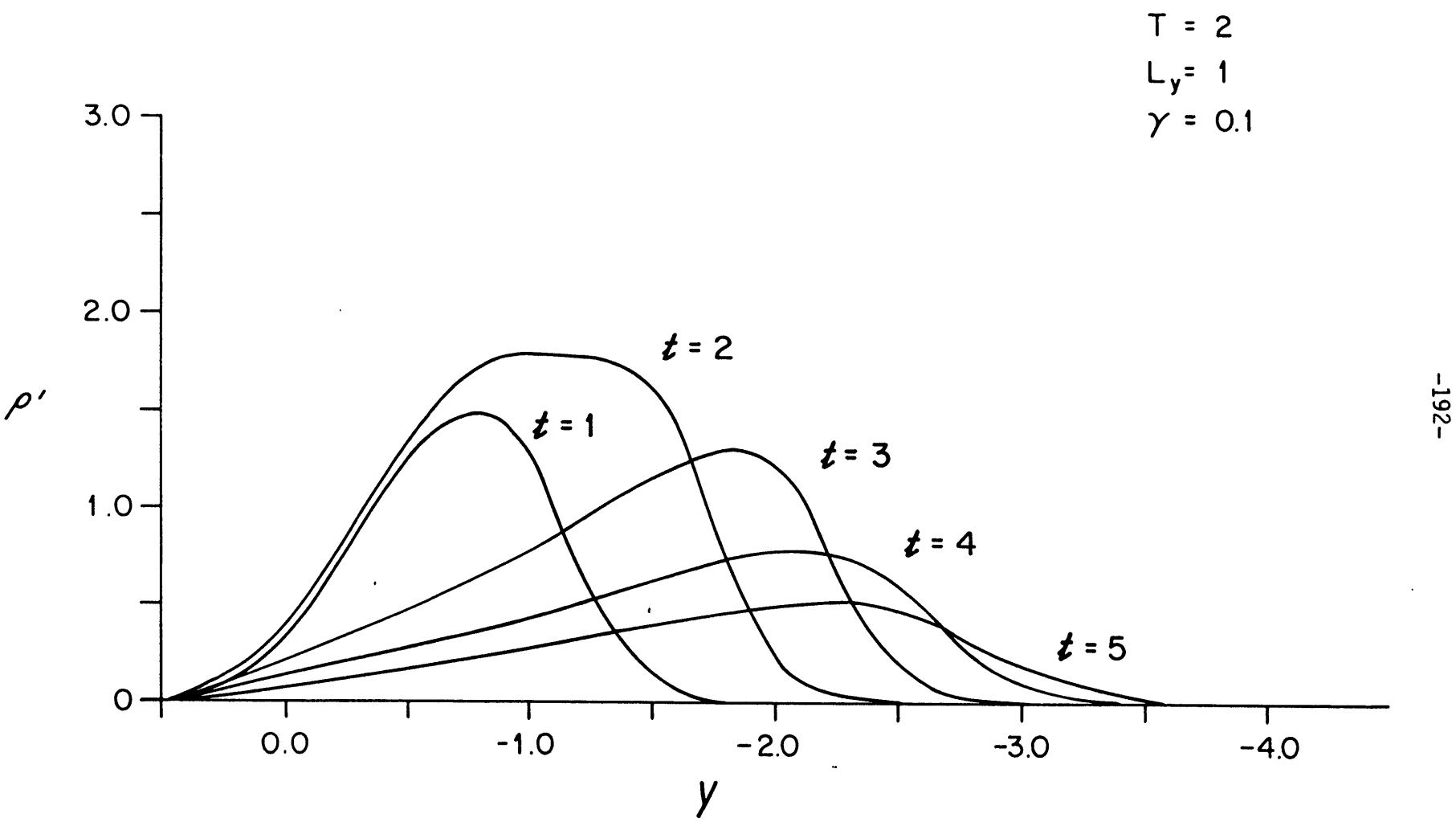

T = 2
$L_y$ = 1
$\gamma$ = 0.1
3.0
2.0
1.0
0
$\rho'$
$t$ = 2
$t$ = 1
$t$ = 3
$t$ = 4
$t$ = 5
0.0
-1.0
-2.0
-3.0
-4.0
$y$

Figure 4.16 Longhsore density distribution along the $x = 1.0$ isobath for cooling with parameters $T = 3$, $L_y = 1$, and $\gamma = 0.05$.

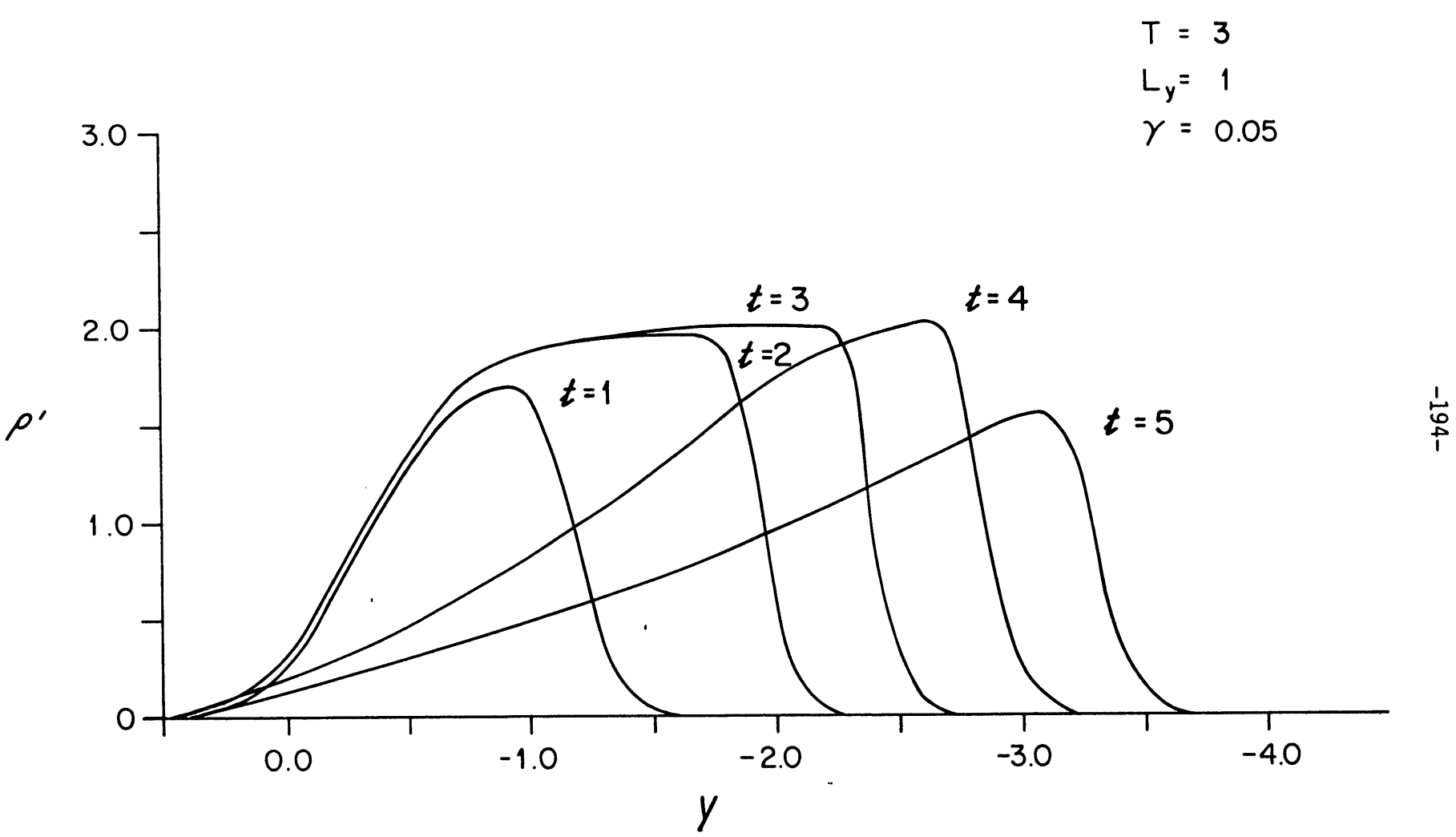

T = 3
$L_y$ = 1
$\gamma$ = 0.05
3.0
2.0
1.0
0
$\rho'$
$t$ = 3
$t$ = 4
$t$ = 2
$t$ = 1
$t$ = 5
0.0
-1.0
-2.0
-3.0
-4.0
$y$

Figure 4.17 Longhsore density distribution along the $x = 1.0$ isobath for cooling with parameters $T = 2$, $L_y = 2$, and $\gamma = 0.05$.

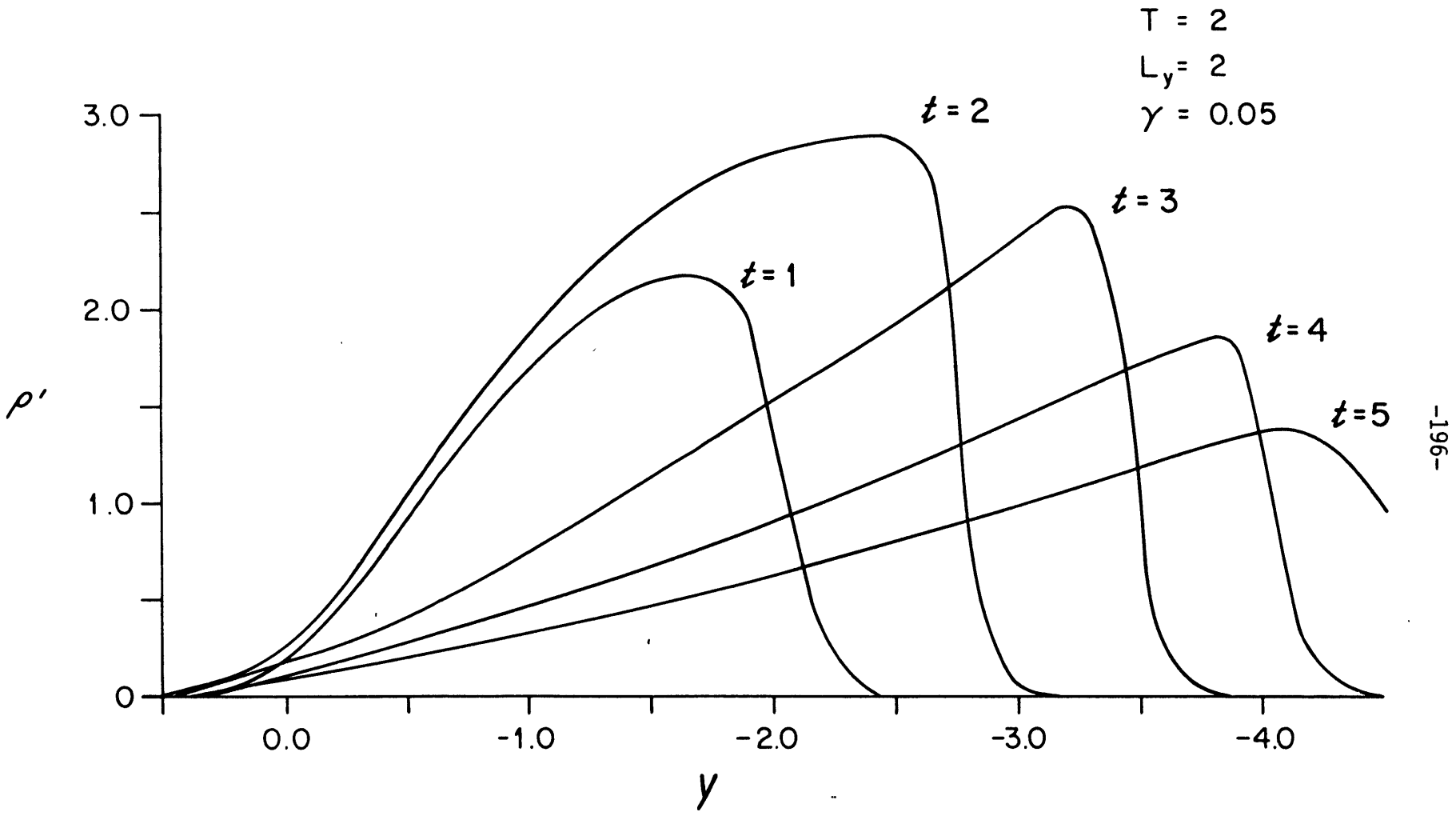

T = 2
$L_y$ = 2
$\gamma$ = 0.05
t = 2
t = 3
t = 1
t = 4
t = 5
3.0
2.0
1.0
0
$\rho'$
0.0
-1.0
-2.0
-3.0
-4.0
y

Figure 4.18a Distribution of bottom temperature in the Middle Atlantic Bight in February 1929 (from Bigelow, 1933).

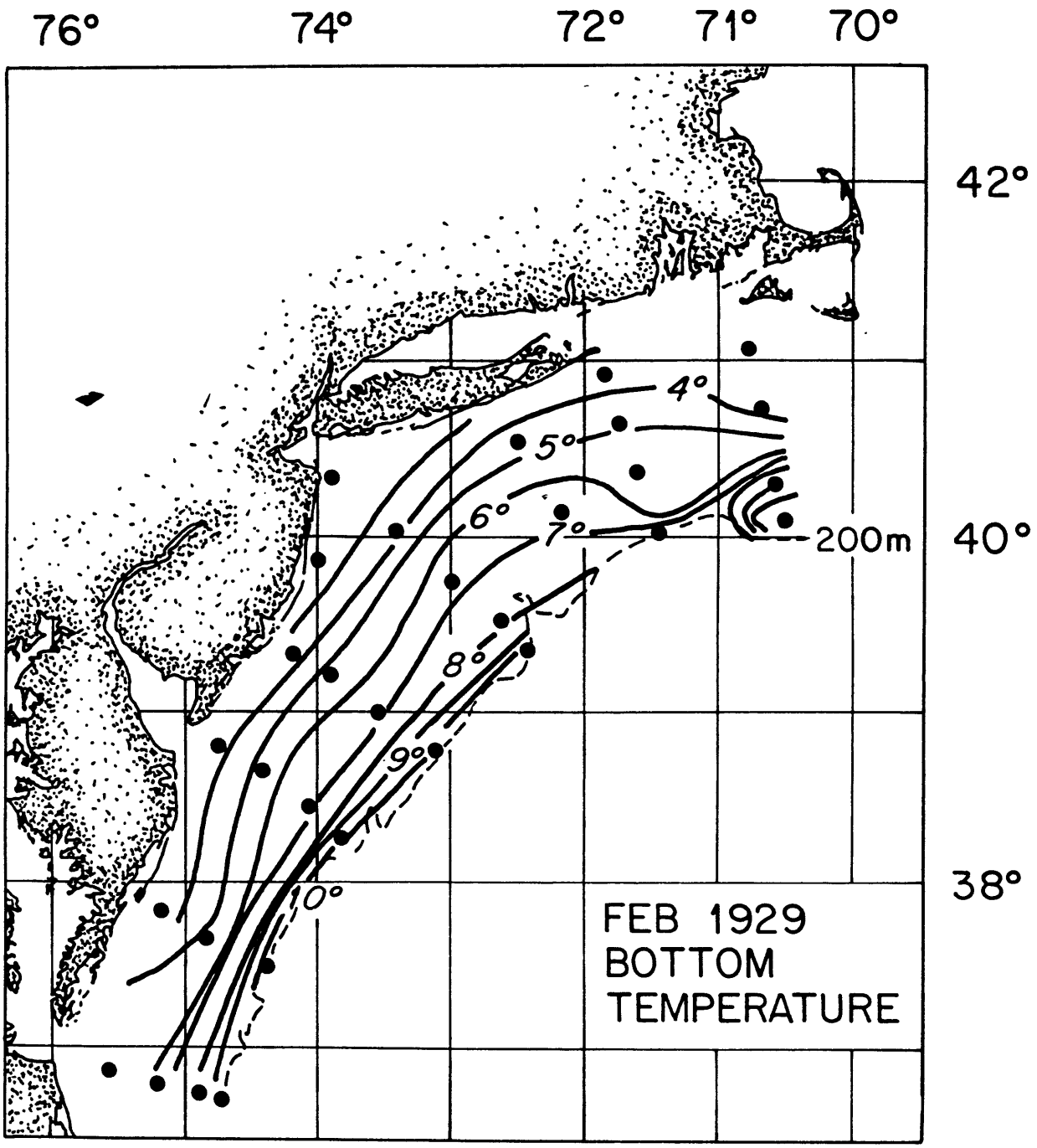

76°
74°
72°
71°
70°
42°
40°
38°
4°
5°
6°
7°
8°
9°
10°
200m
FEB 1929
BOTTOM
TEMPERATURE

Figure 4.18b Distribution of bottom temperature in the Middle Atlantic Bight in April 1929 (from Bigelow, 1933).

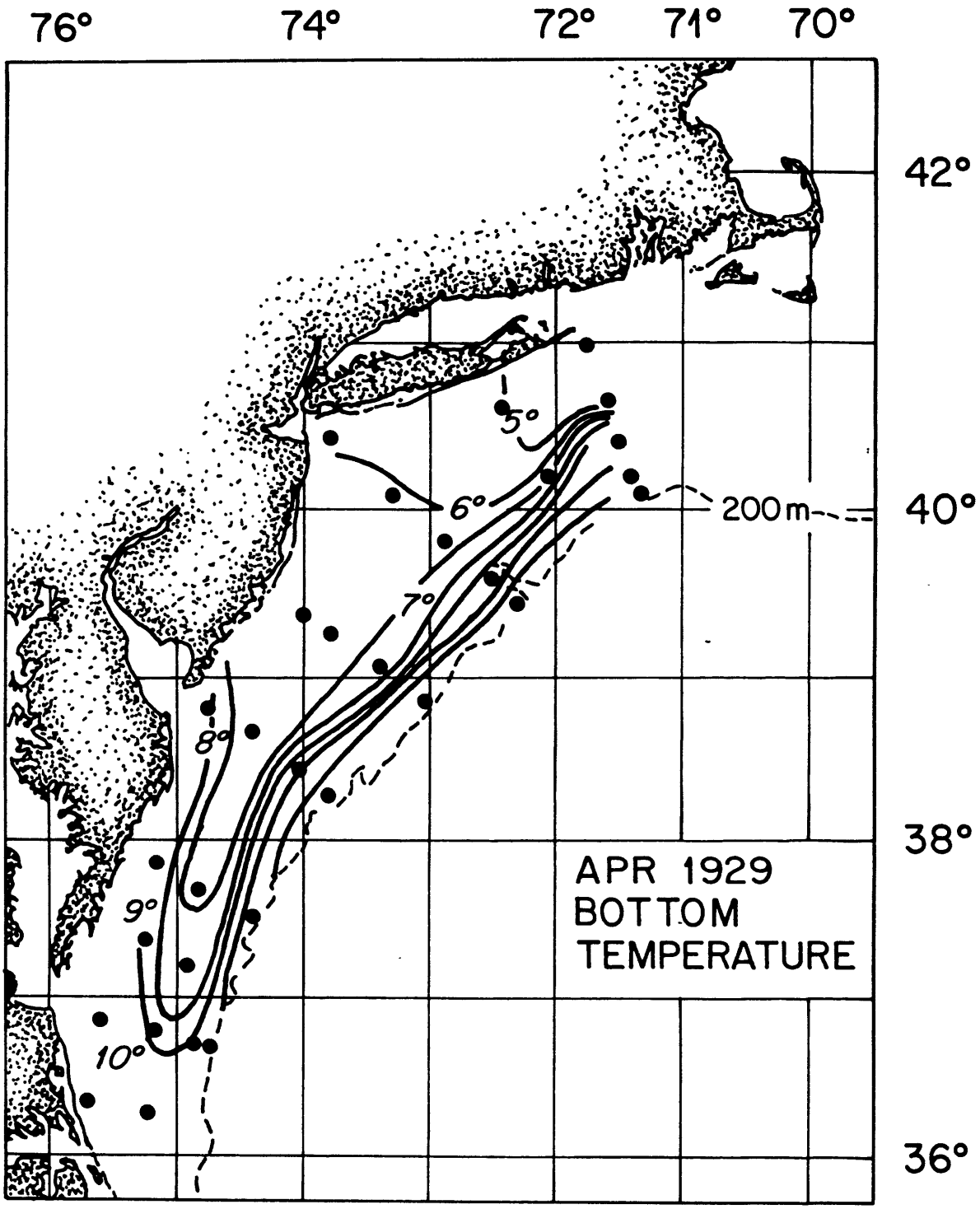

76°
74°
72°
71°
70°
42°
40°
38°
36°
5°
6°
7°
8°
9°
10°
200m
APR 1929
BOTTOM
TEMPERATURE

Figure 4.18c Distribution of bottom temperature in the Middle Atlantic Bight in July 1929 (from Bigelow, 1933).

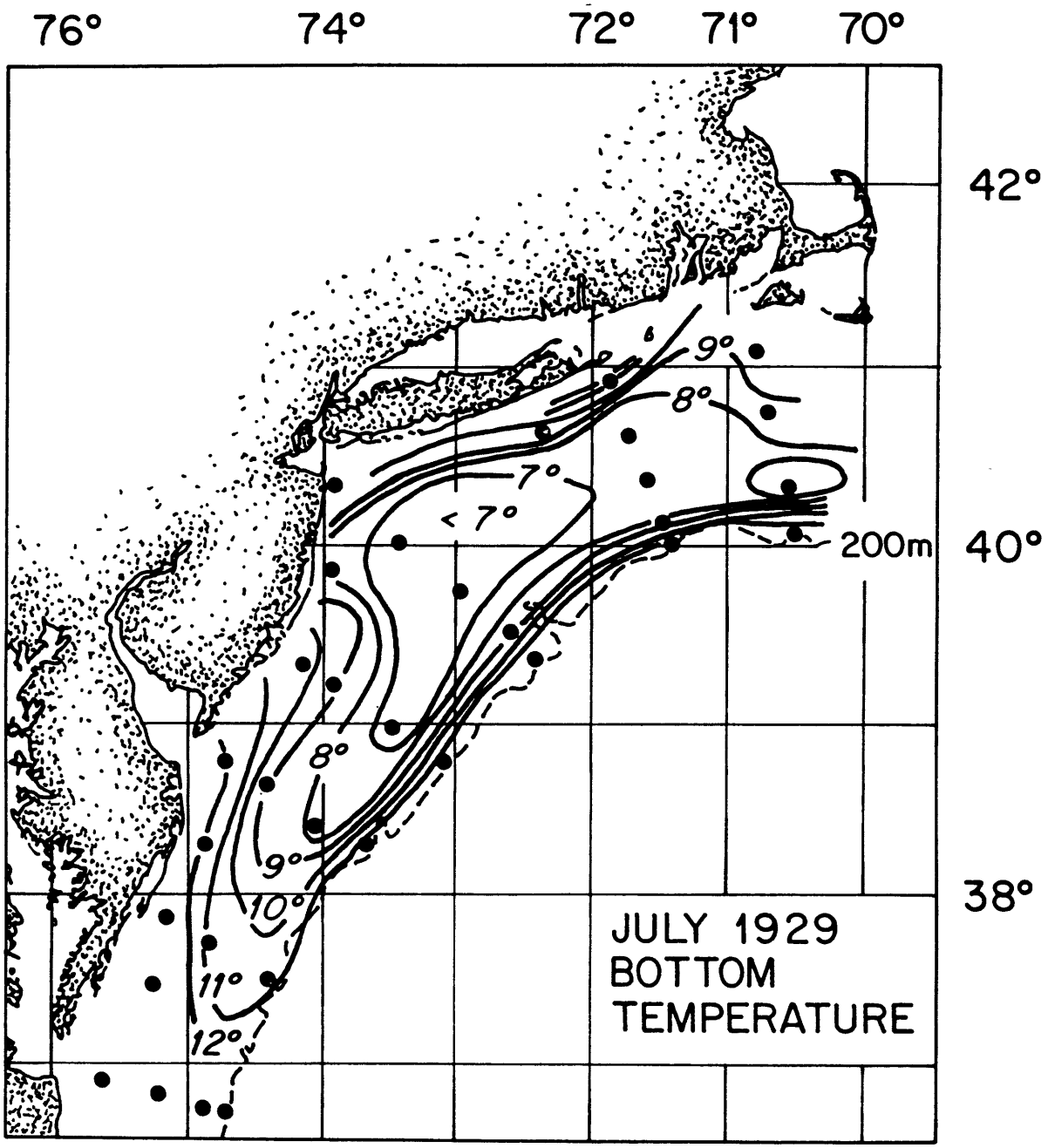

76°
74°
72°
71°
70°
42°
40°
38°
9°
8°
7°
< 7°
200m
8°
9°
10°
11°
12°
JULY 1929
BOTTOM
TEMPERATURE

Figure 4.19 Evolution of bottom temperature between the coast and the shelf break along 71°W, from Chamberlin (1978) and Crist and Chamberlin (1979).

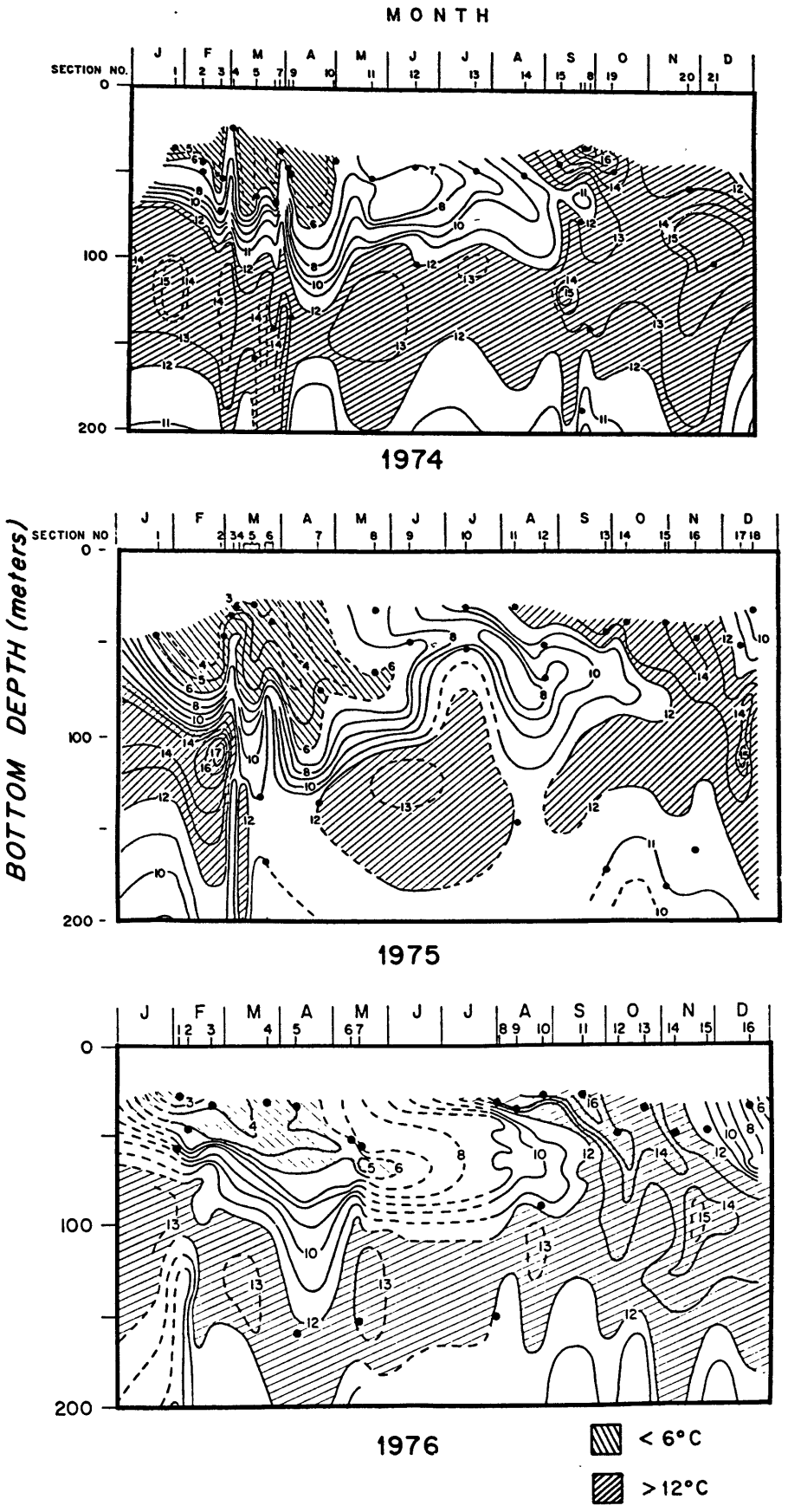
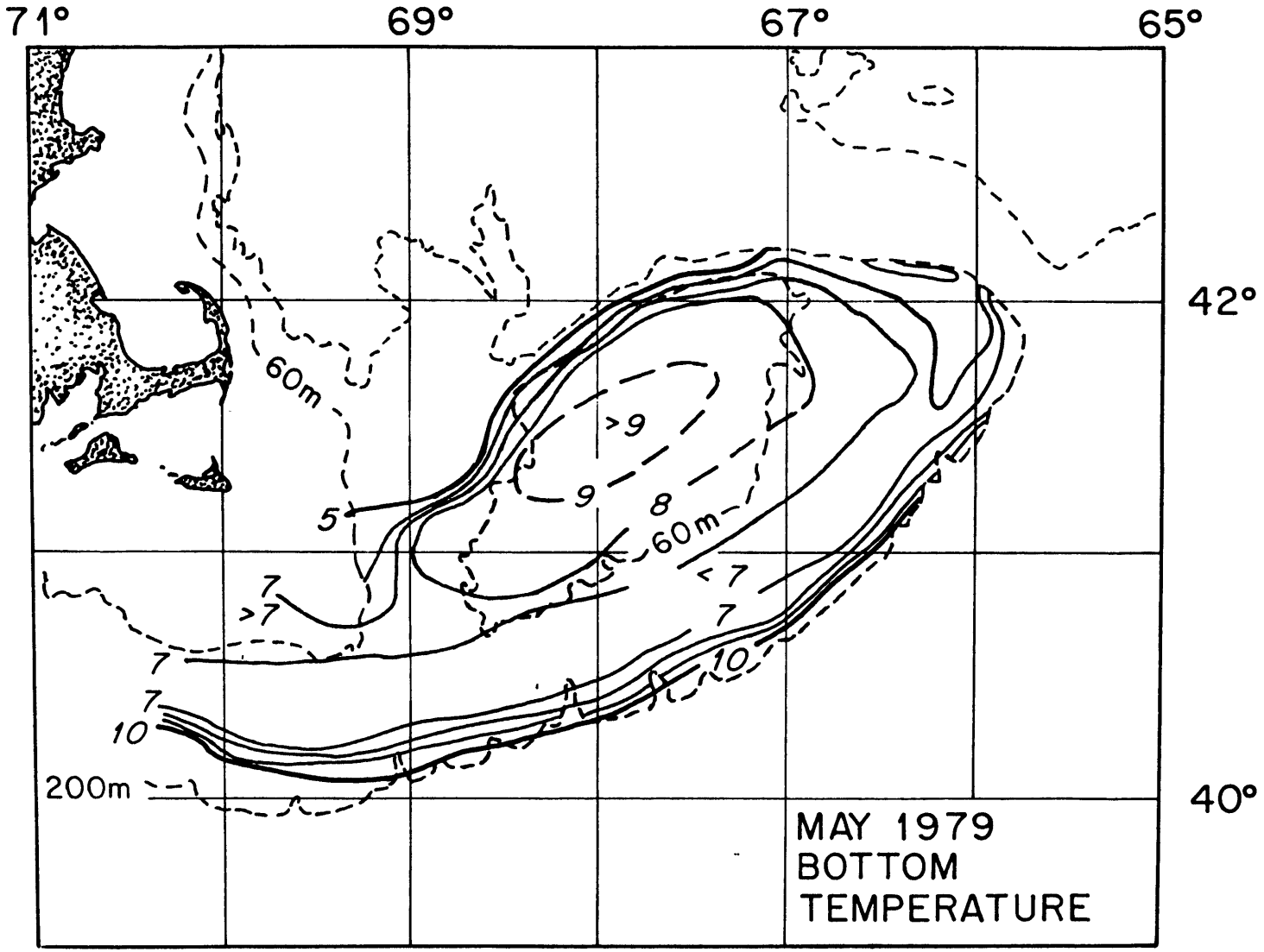

MONTH
SECTION NO.
BOTTOM DEPTH (meters)
1974
1975
1976
< 6°C
> 12°C

Figure 4.20 Distribution of bottom temperature on Georges Bank in May 1979. Data from EG & G (1979).


71°
69°
67°
65°
42°
40°
60m
>9
9
8
5
60m
<7
7
>7
7
7
10
7
10
200m
MAY 1979
BOTTOM
TEMPERATURE

# CHAPTER 5

# MEAN CIRCULATION ON THE WESTERN NORTH ATLANTIC SHELF

Mean southwestward flow of the order 5 cm/sec has been observed both in the Middle Atlantic Bight (Beardsley and Boicourt, 1981) and on the south side of Georges Bank (Butman et al., 1981). It is likely that this mean drift is a consistent feature from Northeast Channel to Cape Hatteras. In Chapter 1, we summarized some properties of this mean flow and reviewed possible driving forces. It has been shown in Section 3.4 that deep ocean "barotropic" and "baroclinic" currents are not very effective in generating mean flow on the shelf. Therefore, the unknown pressure gradient of earlier models (e.g. Csanady, 1976) is probably a representation of forcing acting somewhere over the shelf. In this chapter we will compare the model predictions in Chapters 3 and 4 with the observed mean flow in the Middle Atlantic Bight to examine whether it is necessary to invoke an unknown pressure gradient to drive the southwestward flow.

Wind forcing includes longshore wind stress, offshore wind stress, wind stress curl and the divergence of wind. The formulation in Section 2.2 shows that flow is generated mainly by longshore wind stress and wind stress curl. A similar conclusion was reached by Birchfield (1967). Therefore, we will concentrate the study on the last two types of wind forcing. For the density driven-flow, effects of river buoyancy flux, inflow of dense water, and surface cooling will be examined, using the numerical solutions in Chapter 4.

5.1 Wind-Driven Mean Circulation

Seasonal mean wind stress over the western North Atlantic shelf averaged in one-degree squares over 32 years was computed by Saunders (1977). In winter, the wind stress is mostly offshore from Chesapeake Bay to the Gulf of Maine with magnitude from 0.75 dyne/cm$^2$ near shore to 1.0 dyne/cm$^2$ at the shelf break. The longshore component is small. Between Cape Hatteras and Chesapeake Bay, there is a small southward longshore component (< 0.5 dyne/cm$^2$) caused by a change in the orientation of the coast. North of the Gulf of Maine, the magnitude of wind stress increases and the direction is toward the northeast in the longshore direction. The longshore component is +0.5 dyne/cm$^2$ on the Scotian shelf and +1.0 dyne/cm$^2$ south of Newfoundland. In spring and fall, the wind direction is much the same, but the magnitude of wind stress is smaller. Again, the longshore component in the Middle Atlantic Bight is negligible. Along the Scotian shelf and Newfoundland it is +0.1 and +0.5 dyne/cm$^2$ respectively. The summer wind stress is quite different: about +0.1 dyne/cm$^2$ in the longshore direction from Cape Hatteras to Newfoundland. These features are also demonstrated by the monthly mean wind stress compiled by Beardsley and Boicourt (1981) from time series observations made at several fixed locations in the Middle Atlantic Bight from late 1974 to early 1977. Saunders'(1977) mean wind stress data are used below.

The wind stress curl in this region can be inferred from the vertical velocity at the base of a hypothetical oceanic Ekman layer computed by Leetmaa and Bunker (1978). The computed distribution of annual mean

vertical velocity shows two maxima at the eastern boundary of North America. One is to the east of Newfoundland with a wind stress curl of $2 \times 10^{-8}$ cm/sec$^2$. The other has a value of $+1.5 \times 10^{-8}$ cm/sec$^2$ off Georges Bank. These two maxima vary seasonally. The northern one ranges from $10^{-8}$ cm/sec$^2$ in summer and fall to $+4 \times 10^{-8}$ cm/sec$^2$ in winter. The southern one ranges from $+5 \times 10^{-9}$ cm/sec$^2$ in summer to $+2 \times 10^{-8}$ cm/sec$^2$ in winter. The positive wind stress curl maximum in the north drives a subpolar oceanic gyre that has a maximum transport of 40 Sverdrups (Leetmaa and Bunker, 1978). The southern maximum is close to the continent and is located to the north of the latitude where the Gulf Stream meanders away from the coast. The southern one comes from winter storms which are formed near Cape Hatteras and move to the northeast in the Middle Atlantic Bight (Mooers et al., 1976). This maximum in wind stress curl has direct influence on the winter circulation in the Middle Atlantic Bight.

Those values of wind stress curl are very likely underestimated. In Leetmaa and Bunker's (1978) calculation, the strong winter cyclones, which are important sources of wind stress curl, could be smoothed out by averaging over 2° by 5° grids . Nevertheless, using above values of wind stress curl, it is possible to make an order of magnitude estimate of the wind-driven flow on the shelf.

Using Equations (3.7a-c), the magnitude of the flow driven by longshore wind stress can be calculated using values listed in Table 3.2. In winter, the wind stress in the Middle Atlantic Bight is mainly in the offshore direction. It also has significant divergence because of

the offshore increase in the magnitude of wind stress. However, these two factors are not effective in driving the mean flow. Over the Scotian shelf in winter, there is a longshore stress to the northest with a magnitude of 0.5 dyne/cm$^2$ over a longshore range of 500 km. The boundary layer width is calculated to be 45 km at the southwest side of the Scotian shelf, where the sea surface depression reaches a maximum of 6.5 cm. The maximum longshore velocity is 15.8 cm/sec. A total longshore transport of $1.8 \times 10^5$ m$^3$/sec, flowing from the south side of Georges Bank onto the Scotian shelf, can be generated by the wind stress. Forward influence of this flow may extend to Georges Bank and the Middle Atlantic Bight.

In summer, the wind stress is weak, and its direction is toward the northeast over the shelf between Cape Hatteras and Nova Scotia. For a wind stress of 0.1 dyne/cm$^2$ over a 1000 km longshore distance, the boundary layer thickness is 64 km in the southern part of the Middle Atlantic Bight, which is about the width of the shelf. The maximum longshore flow is to the northeast with a magnitude of 3.2 cm/sec. The maximum depression of sea surface is 1.8 cm. The total transport is also to the northeast with a magnitude of $0.5 \times 10^5$ m$^3$/sec. The flow is weaker in the set-up regions of the Scotian shelf and Georges Bank.

Beardsley et al. (1976) obtained a transport of 8000 km$^3$/year ($2.5 \times 10^5$ m$^3$/sec) from observations made in the Middle Atlantic Bight. The transport is nearly constant from Cape Cod to Cape Hatteras. The magnitude of transport calculated from the model is comparable to the observed magnitude in winter, although the direction is reversed. The

flow driven by mean wind stress is significant in contributing to the mean flow, especially in the near-shore region. In summer, the wind stress induced flow is small except perhaps at the southern part of the Middle Atlantic Bight.

The strength of flow under forcing by wind stress curl can be calculated from Table 3.3, using the asymptotic relations (3.14) for different longshore ranges of wind forcing. Because the longshore transport is concentrated at the shelf break (Figure 3.8), it is ambiguous to define an offshore limit in calculating the transport on the shelf. Therefore, only the magnitude of velocity will be used for comparsion. The curl of wind stress is stronger in winter than in other seasons. For a wind stress curl of $2 \times 10^{-8}$ cm/sec$^2$ acting over a 1000 km longshore distance from Georges Bank to Newfoundland, the maximum sea surface depression is 2.9 cm with an onshore flow of 0.5 cm/sec. The maximum longshore velocity is 3.4 cm/sec to the northeast. This value again has a comparable strength but is opposite in direction to the mean flow on the outer shelf. Its forward influence may reach the Middle Atlantic Bight. In summer, the flow produced by wind stress curl is much weaker.

The values given above demonstrate that the flow driven by wind stress curl is important to the mean shelf circulation. Besides the flow strength, the circulation generated by the curl of wind stress have some properties, which are significant to the mean circulation. Under longshore stress forcing, both sea level and longshore velocity decrease rapidly away from the shore. On the other hand, the flow generated by

wind stress curl is mainly in the outer shelf region, being stronger at the shelf break. This difference is significant over a wide continental shelf such as the Middle Atlantic Bight.

This property is important, when complex coastal geometry exists, e.g. the Laurentian Channel and the Gulf of Maine. Because the flow under wind stress forcing is strongest near shore, topographic features and the orientation of coastline will effectively interrupt the forward influence of the flow. Under wind stress curl forcing, longshore flow is generated by cross-isobath vortex stretching on the outer shelf, where topography is more uniform than that at the coast. The flow on the shelf may reach a longer distance in the forward direction than the flow forced by longshore wind stress.

Although flow driven by wind cannot be the cause of the mean southwestward drift in the Middle Atlantic Bight, it can be observed under strong and persistent wind conditions. The anomalous flow during the spring and summer of 1976 and the winter of 1976-1977 in the Middle Atlantic Bight were related to the strong and persistent wind conditions by Beardsley and Boicourt (1981). The observed strong wind-induced flow on the outer shelf is likely to be driven by the wind stress curl. However, more observational evidence is needed to understand the importance of wind stress curl in the shelf circulation.

5.2 Dispersion of River Water

The stream flux from rivers in the Middle Atlantic Bight has been summarized by Beardsley and Boicourt (1981). The largest one is the Chesapeake Bay estuary, which has a stream flux of 2000 $m^3$/sec. The

outflows of the Hudson River and the Connecticut River are of the order of 1000 $m^3$/sec. These values are comparable to the example given in Table 4.1. We will use the numerical solution in Section 4.4.2 to estimate the physical quantities associated with the river flow. According to the numerical solution, the river water from the Hudson River and the Conneticut River may move along the coast of New York and New Jersey. The water from the Chesapeake Bay may appear near the coast south of it. The speed of fresh water movement south of New York derived from Figure 4.5 is about 3.5 cm/sec or 2.6 km/day. The maximum longshore velocity inside the plume reaches 6 cm/sec (Figure 4.3). The river plume may move 400 km to the southwest in 5 months.

The largest river system on the eastern seaboard of North America is the St. Lawrence River. The stream flux is of the order 10,000 $m^3$/sec, which is about ten times greater than that of the Hudson estuary (Sutcliffe et al., 1976). To estimate its effect on the shelf circulation, we will use the solution derived in Section 4.4.2 with proper scaling of the density field. The numerical solution shows that $R_0/\gamma$ is an important parameter in determining the density distribution. For a large river flux, we increase the density scale accordingly so that $R_0/\gamma$ remains constant. This new density scale will give a larger velocity scale than the one listed in Table 4.1, while the nondimensional solution is not significantly affected. If all the water from the St. Lawrence River is completely mixed to the bottom, the propagation speed of river disturbations would be ten times larger than the one listed in Table 4.1, or about 35 cm/sec. However, for such a large river system, most of the

river water will flow out on the surface layer without reaching the bottom, and the velocity of southward longshore movement of river water will be greatly reduced.

Downstream influence of the St. Lawrence River discharge was studied by Sutcliffe et al. (1976). The southward propagation of river water along the coast was clearly demonstrated by their correlation analyses of temperature and salinity distribution in both surface and subsurface layers. According to their calculation, the river water reached Boston, which is 2300 km downstream, in 9 months. The mean propagation speed is 7 km/day (8.1 cm/sec). A quarter of the total river flux from the St. Lawrence River has to be mixed to the bottom to give a self-advection speed of this magnitude. Southwestward river dispersion was also observed in the Middle Atlantic Bight. Based on Bigelow's (1933) data, the southwestward increase in salinity between the shore and the 40 m isobath was shown by Ketchum and Keen (1955). They pointed out that this increase was mainly caused by the subsurface salinity distribution. These results agree with the density distribution predicted from our numerical solutions.

The model of river inflow in Chapter 4 explains the density distribtuion as well as the mean drift without postulating another external cause for the mean drift. The explanation of mean drift by the self-advection of density field is simple and certainly dynamically sound. The density forcing from a river inflow could be the main driven mechanism in the near-shore region on the wester North Atlantic shelf.

5.3 The Movement of Winter Water in the Middle Atlantic Bight

The Gulf of Maine and the Middle Atlantic Bight are both subjected to strong cooling in winter. In the early cooling season, the effect is restricted to the surface layer and the bottom density change is small. After the water is well mixed, the surface density flux is distributed uniformly throughout the water column. The seasonal heat flux in the Middle Atlantic Bight has been described by Bunker (1976). Cooling starts in October, reaches a maximum rate of -250 Watts/$m^2$ in December and decreases to nearly zero by March. The mean heat loss during this period is -125 Watts/$m^2$. The mean coolng rate in the Gulf of Maine from December 1964 to March 1965 was estimated by Hopkins and Garfield (1979) to be -135 Watts/$m^2$. These two figures are reasonably close.

We have shown in Section 4.5.3 that the winter density flux in the Middle Atlantic Bight is large enough for density fronts to form under winter cooling. The numerical solution in Section 4.4.3 can be used to examine the properties of the flow and density fields. Figure 4.10 shows that the fastest longshore propagation of density perturbations occurs at about x = 1.0, where the water depth is 67 m. For a longshore cooling range of 100 km, Figure 4.14 shows that the location of minimum longshore temperature moves with a mean speed of 0.62 (1.5 cm/sec) for the first 3 months after the cooling ends. The maximum density value is about $0.4 \times 10^{-3}$ gm/$cm^3$, which gives a maximum velocity of 4.8 cm/sec for the water parcel behind the front by Equation (4.3). The flow response depends strongly on the longshore range of cooling (Figure 4.17). If the cooling is over a longshore range of 200 km, the maximum flow may reach 7 cm/sec, and the density front propagates at a speed of

3.6 cm/sec.

In February, the uniform temperature distribution along isobaths in Figure 18a indicates that local cooling extends over the whole Middle Atlantic Bight. The velocity of the flow produced by cooling would be high enough to account for the observed near-bottom mean flow of 5 cm/sec in winter and early spring in the northern part and in summer in the southern part of the Middle Atlantic Bight. The other contribution of density-driven flow comes from the outflow of the Gulf of Maine Intermediate Water. An accurate calculation of the density flux from the Gulf of Maine is not possible; nevertheless, we will make an order of magnitude estimation. Hopkins and Garfield (1979) calculated the water mass budget in the Gulf of Maine and concluded that a volumn about 5100 $km^3/yr$ ($1.6 \times 10^5$ $m^3/sec$) of Gulf of Maine Intermediate Water would export from the Great South Channel and the Northeast-Channel. Using a thermal expansion coefficient of $10^{-4}$ $cm^3/°C$, and a temperature difference of 2°C between this water mass and the water outside the gulf in late spring, an equivalent density flux of $3.2 \times 10^7$ gm/sec is obtained. Assuming that this flux spreads over a coastline of 100 km, the resulting density flux is of the same order as that in Table 4.1. The numerical solution in Section 4.4.2 for heavy density flux from the coast can be used to estimated the corresponding physical quantities. Figure 4.9 shows that the cold water front moves southwestward with a speed of 1 cm/sec, which is much slower that in the cooling case. The maximum flow behind the front can reach as high as 10 cm/sec after 5 months (Figure 4.8d). This value is comparable to the velocity observed

on the south side of Georges Bank and south of New England in spring and summer.

Because of the agreement between the predicted cold water movement and the observations, we can describe the evolution of density field in the Middle Atlantic Bight based on the theory of density-driven flow in the previous chapter. Annual temperature variations in the area south of Long Island, observed repeatedly for three years by Ketchum and Corwin (1964), give a fairly good representation of the water structure in the Middle Atlantic Bight. The cooling starts in late October and early November each year. The water becomes vertically homogeneous from December to April or May. The vernal warming in spring and summer affects the nearshore water as well as the water in the surface layer. The bottom water in the mid-shelf region remains cold throughout the year. It is represented by a temperature minimum in the T-S diagram and constitutes the "cold pool" observed by Bigelow (1933). The cold pool is limited inshore by warm low salinity water and offshore by the shelf break front. In the longshore direction, it has been observed as far south as Cape Hatteras in August (Ford et al., 1952).

This cold water mass in spring and summer may have several constituents, depending on the time and location of observations, and the condition of previous winter. The first constituent is the water cooled in winter in the Middle Atlantic Bight and on the south side of Georges Bank. The second one is the cold water flowing out of the Gulf of Maine through the Great South Channel. This is the Gulf of Maine Intermediate Water, possibly modified slightly by river inflow. The last one is the

outflow of the Gulf of Maine Intermediate Water through the Northeast Channel.

The observed local winter water is characterized by a tight curve in the T-S diagram. One example was given by Beardsley and Flagg (1977). It is the result of the overturning of entire water column caused by strong surface cooling. The water temperature is quite uniform along isobaths (Figure 4.18a). Long-isobath flow is generated by the interaction between density perturbation and bottom topography and has a speed comparable to the observed one during this period. The local winter water is advected southward by such a density-dependent flow. The spring heating starts in March and warms up the near-shore water as well as the water at the southern portion of the Middle Atlantic Bight. The arrival of cold water from the northern portion of the Middle Atlantic Bight then creates a strong longshore temperature gradient off the Chesapeake Bay area through nonlinear advection (Figure 4.18b). South of New England, the local winter water is replaced by successive cold water pools in March-April, which leave the source region, e.g. the Nantucket Shoals, Georges Bank, or the Gulf of Maine, as a result of previous cold outbreaks in January and February (Figure 4.19).

During cold years, the Gulf of Maine Intermediate Water flows out of the gulf through the Great South Channel (Bigelow, 1915; Hopkins and Garfield, 1979). Hopkins and Garfield (1979) traced the direct outflow of the Gulf of Maine Intermediate Water through the Great South Channel to the shelf south of New England. They found that the Intermediate Water, which was defined by a temperature range of 2.2-4.2°C and a

salinity range of 31.97-32.91 o/oo, flowed through the Great South Channel in the late winter and early spring of 1965 and arrived at the shelf south of Long Island in May. This process can be viewed as a density flux from the Great South Channel, followed by a long-isobath dense water movement. By September, it disappeared presumably due to the decay of density fronts and the subsequent mixing with the surrouding water masses.

Hopkins and Garfield (1979) also showed that the Gulf of Maine Intermediate Water may leave the Gulf of Maine though the Northeast Channel. It is shown in Figure 4.20 as the bottom water with a temperature minimum of 7°C. This water spreads uniformly in a narrow band along isobaths from the Northeast Channel to the shelf south of Cape Cod. The Gulf of Maine origin of this water mass is suggested by a tongue of cold water at the northeast corner of Georges Bank. The southwestward movement of this water mass is shown in the progressive diagram of EG & G (1979), which gives a near-bottom mean flow of about 4 km/day along the 80 m isobath from March to August 1979. This outflow of cold water can also be interpreted as the dense water from coastal density flux and the subsequent long-isobath propagation of density perturbations.

In summary, one concludes that the density-driven flow can interpret both qualitatively and quantitatively the bottom temperature distribution in the Middle Atlantic Bight. Obviously, the propagation of thermal fronts is an important phenomenon on the outer shelf region from winter to late summer. The long-isobath flow associated with the density

perturbation of cold water mass must contribute significantly to the mean circulation on the continental shelf from Georges Bank to Cape Hatteras.

## 5.4 Conclusion

The different driving forces mentioned earlier in this chapter contribute significantly to the Middle Atlantic Bight mean circulation. In the near-shore zone, the longshore wind stress drives a flow to the northeast in winter. Southwestward flow of light river water occurs in winter and spring inside a coastal boundary layer. This longshore movement of river water is a self-advective process independent of the mean flow on the outer shelf.

Over the outer shelf in winter, the flow driven by the mean wind stress curl has comparable speed but is opposite in direction to the observed mean flow. Under strong and persistent wind conditions, this flow may stand out in the monthly mean velocity. On the other hand, the winter cooling in the Middle Atlantic Bight and south of Georges Bank produces longshore flow as strong as the observed mean southwestward flow from Georges Bank to Cape Hatteras. The export of the Gulf of Maine Intermediate Water though the Great South Channel and the Northeast Channel is in the form of propagating density fronts. It is concluded that density-driven currents adequately account for the southwestward movement of the cold winter water in the Middle Atlantic Bight from winter to late summer without invoking any other external causes. The southwestward flow associated with the cold water passage may account for a significant amount of the mean southwestward drift during this period.

# REFERENCES

Barcilon, V., 1966: On the influence of the peripheral Antarctic water discharge on the dynamics of the Circumpolar Current. J. Mar. Res., 24, 269-275.

Beardsley, R. C. and W. C. Boicourt, 1981: On estuarine and continental shelf circulation in the Middle Atlantic Bight. In Evolution of Physical Oceanography, B. A. Warren and C. Wunsch, eds., MIT Press, Cambridge, Ma., 198-233.

____, and C. N. Flagg, 1977: The water structure and shelf-water/slope-water front on the New England continental shelf. Memoires de la Societe Royale des Sciences de Liege, 6e serie, 10, 209-225.

____, and J. Hart, 1978: A simple theoretical model for the flow of an estuary onto a continental shelf. J. Geophys. Res., 83, 873-883.

____, and C. D. Winant, 1979: On the mean circulation in the Mid-Atlantic Bight. J. Phys. Oceanogr., 9, 612-619.

____, W. C. Boicourt and D. V. Hansen, 1976: Physical Oceanography of the Middle Atlantic Bight. Special Symposia Vol. 2, 20-34, Amer. Soc. Limn. Oceanogr.

Biglow, H. B., 1915: Exploration of the coastal water between Nova Scotia. and Chesapeake Bay, July and August 1913 by the U. S. Fisheries Schooner Grampus. Bull. Mus. Comp. Zool., 59, 151-359.

____, 1933: Studies of the waters on the continental shelf, Cape Cod to Chesapeake Bay, I: The cycle of temperature. Papers in Phys. Oceanogr. and Meteor., 2, 1-135.

Birchfield, G. E., 1967: Horizontal transport in a rotating basin of parabolic depth profile. J. Geophys. Res., 72, 6155-6163.

____, 1972: Theoretical aspects of wind-driven currents in a sea or lake of variable depth with no horizontal mixing. J. Phys. Oceanogr., 2, 355-362.

Biscaye, P. E., C. R. Olsen and G. Mathieu, 1978: Suspended particles and natural radionuclides as tracers of pollutant transports in continental shelf waters of the eastern USA. First American-Soviet Symposium on the Chemical Pollution of the Marine Environment, May 1977, Odessa, USSR. pp 125-147.

Brown, W. S., and R. C. Beardsley, 1978: Winter circulation in the

Western Gulf of Maine, Part I: Cooling and water mass formation. J. Phys. Oceanogr., 8, 265-277.

Bumpus, D. F., 1973: A description of the circulation on the continental shelf of the east coast of the United States. Prog. Oceanogr., 6, 111-157.

Bunker, A. F., 1976: Computations of surface energy flux and annual air-sea interation cycles of the North Atlantic Ocean. Mon. Weather Rev., 104, 1122-1140.

Butman, B., R. C. Beardsley, B. Magnell, J. A. Vermersch, R. Schlitz, R. Limeburner, W. R. Wright and M. A. Noble, 1981: The mean circulation on Georges Bank. (Submitted to J. Phys. Oceanogr.).

Chamberlin, J. L., 1978: Temperature structure on the continental shelf and slope south of New England during 1975. In Ocean Variability: Effects on U.S. Marine Fishery Resources - 1975, J. R. Goulet Jr. and E. D. Haynes, eds., NOAA Tech. Rep. NMFS Circ. 416, 271-292.

Crist, R. W., and J. L. Chamberlin, 1979: Temperature structure on the continental shelf and slope south of New England during 1976. In Ocean Variability in the U. S. Fishery Conservation Zone, 1976, J. R. Goulet Jr. and E. D. Haynes, eds., NOAA Tech. Rep. NMFS Circ. 427, 315-335.

Csanady, G. T., 1976: Mean circulation in shallow seas. J. Geophys. Res., 81, 5389-5399.

____, 1978: The arrested topographic wave. J. Phys. Oceanogr., 8, 47-62.

____, 1979: The pressure field along the western margin of the North Atlantic. J. Geophys. Res., 84, 4905-4915.

____, 1980: Longshore pressure gradients caused by offshore wind. J. Geophys. Res., 85, 1076-1084.

____, 1981: Shelf circulation cells. Phil. Trans. Roy. Soc., in press.

EG & G Enviromental Consultants, 1979: Data Report, Eulerian Studies March - August, 1979. In Appendix B of Twelfth Ouarterly Progress Report, EG G Enviromental Consultants, Waltham, Ma..

Ekman, V. W., 1905: On the influence of the earth's rotation on ocean currents. Ark. Nat. Astron. Fys., 2, 1-52.

Fofonoff, N. P., 1962: Dynamics of ocean currents. In The Sea, Vol. 1, M. N. Hill, ed., Interscience Publishers, New York, 323-395.

Foldvik, A., and T. Kvinge, 1974: Bottom currents in the Weddell Sea. Report No. 37, Geophysical Institute, University of Bergen, 43 pp.

Ford, W. L., J. R. Longard and R. E. Banks, 1952: On the nature, occurence and origion of cold low salinity water along the edge of the Gulf Stream. J. Mar. Res., 11, 281-293.

Forster, T. D., and E. C. Carmack, 1976: Frontal zone mixing and Antartic bottom water formation in the southern Weddell Sea. Deep-Sea Res., 23, 301-317.

Gill, A. E., 1973: Circulation and bottom water production in the Weddell Sea. Deep-Sea Res., 20, 111-140.

Hendershott, M. C., and P. Rizzoli, 1976: The winter circulation of the Adriatic Sea. Deep-Sea Res., 23, 353-370.

Holland, W. R., 1973: Baroclinic and topographic influences on the transport in western boundary currents. Geophys. Fluid Dyn., 4, 187-210.

Hopkins, T. S., and N. Garfield, 1979: Gulf of Maine Intermidiate Water. J. Mar. Res., 37, 103-139.

Houghton, R. W., R. Schlitz, J. L. Chamberlin, R. C. Beardsley and B. Butman, 1981: The Middle Atlantic cold pool. (in preparation).

Iselin, C. O. D., 1955: Coastal currents and the fisheries. Deep-Sea Res., Suppl. to Vol. 3, 474-478.

Jacobs, S. S., A. F. Amos and P. M. Bruchausen, 1970: Ross Sea oceanography and Antarctic Bottom Water formation. Deep-Sea Res., 17, 935-962.

Jeffreys, H., 1923: The effect of a steady wind on the sea level near a straight shore. Phil. Mag., 45, 114-125.

Ketchum, B. H., and N. Corwin, 1964: The persistence of "winter water" on the continental shelf south of Long Island, New York. Limnol. Oceanogr., 9, 467-475.

____, and D. J. Keen, 1955: The accumulation of river water over the continental shelf between Cape Cod and Chesapeake Bay. Deep-Sea Res., Suppl to Vol. 3, 346-357.

Killworth, P. D., 1973a: A two-dimensional model for the formation of Antarctic Bottom Water. Deep-Sea Res., 20, 941-971.

____, 1973b: On the circulation of a homogeneous ocean induced by the

presence of continental slopes. J. Phys. Oceanogr., 3, 3-15.

____, 1974: A baroclinic model of motions on Antarctic continental shelves. Deep-Sea Res., 21, 815-837.

Leetmaa, A., and A. F. Bunker, 1978: Updated charts of the mean annual wind stress, convergences in the Ekman layers, and Sverdrup transports in the North Atlantic. J. Mar. Res., 36, 311-322.

____, P. Niiler and H. Stommel, 1977: Does the Sverdrup relation account for the Mid-Atlantic circulation. J. Mar. Res., 35, 1-10.

Luyten, J. R., 1977: Scales of motion in the deep Gulf Stream and across the continental rise. J. Mar. Res., 35, 49-74.

Montgomery, R. B., 1941: Transport of the Florida Current off Havana. J. Mar. Res., 4, 198-219.

____, 1969: Comments on ocean leveling. Deep-Sea Res., Suppl. to Vol. 16, 147-152.

Mooers, C. N. K., J. Fernandez-Partagas and J. F. Price, 1976: Meteorological forcing fields of the New York Bight, First year's progress report. Technical Report, Rosenstiel School of Marine and Atmospheric Science, University of Miami, 151 pp.

Pedlosky, J., 1974: Longshore currents, upwelling and bottom topography. J. Phys. Oceanogr., 4, 214-226.

____, 1979: Geophysical Fluid Dynamics. Springer-Verlag, New York, 624 pp.

Pettigrew, N. R., 1981: The dynamics and kinematics of the coastal boundary layer off Long Island. Ph. D. thesis, MIT-WHOI, 261 pp.

Roache, P. J., 1976: Computational Fluid Dynamics. Hermosa Publishers, Albuguerque, N.M., 446 pp.

Sarkisyan, A. S., 1977: The diagnostic calculations of a large-scale oceanic circulation. In The Sea, Vol. 6, E. D. Goldburg, I. N. McCave, J. J. O'Brien and J. H. Steele, eds., John Wiley, New York, 363-458.

Saunders, P. M., 1977: Wind stress on the ocean over the eastern continental shelf of North America. J. Phys. Oceanogr., 7, 555-566.

Schmitz, W. J., 1974: Observation of low-frequency current fluctuations on the continental slope and rise near site D. J. Mar. Res., 32, 233-251.

Schulman, E. E., and P. P. Niiler, 1970: Topographic effects on the wind-driven ocean circulation. Geophys. Fluid Dyn., 1, 439-462.

Scott, J. T., and G. T. Csanady, 1976: Nearshore currents off Long Island J. Geophys. Res., 81, 5401-5409.

Semtner, A. J., and Y. Mintz, 1977: Numerical simulation of the Gulf Stream and Mid-Ocean eddies. J. Phys. Oceanogr., 7, 208-230.

Stommel, H., 1948: The western intensification of wind-driven ocean currents. Trans. Amer. Geophys. Un., 29, 202-206.

____, and A. Leetmaa, 1972: The circulation on the continental shelf Proc. Nat. Acad. Sci., U.S., 69, 3380-3384.

Sturges, W., 1968: Sea-surface topography near the Gulf Stream. Deep-Sea Res., 15, 149-156.

Sutcliffe, W. H., R. H. Loucks and K. F. Drinkwater, 1976: Coastal circulation and physical oceanography of the Scotian Shelf and the Gulf of Maine. J. Fish. Res. Board Can., 33, 98-115.

Sverdrup, H. U., M. W. Johnson and R. H. Fleming, 1942: The Oceans. Prentice-Hall, Englewood Cliffs, N.J., 1087 pp.

Warren, B. A., 1981: Deep Circulation of the world ocean. In Evolution of Physical Oceanography, B. A. Warren and C. Wunsch, eds., MIT Press, Cambridge, Ma., 6-41.

Whitham, G. B., 1974: Linear and Nonlinear Waves. Wiley and Sons, New York., 636 pp.

Winant, C. D., and R. C. Beardsley, 1979: A comparison of some shallow wind-driven currents. J. Phys. Oceanogr., 9, 218-220.

## BIOGRAPHICAL NOTE

Ping-Tung Peter Shaw was born on November 15, 1950 in Pingtung, Taiwan, the Republic of China. He attended the Elementary School for the Youths of Air Forces and the Taiwan Provincial Pingtung High School. He earned his B.S. degree in physics from National Taiwan University in June, 1972. Then, as a R.O.T.C. officer, he served in the Republic of China Army for two years. He came to the United States and started his graduate work in September 1974. After finishing two years of study leading to a M.S. degree in physical oceanography at the Graduate School of Oceangraphy, the University of Rhode Island, he was admitted to the Joint Program in Oceanography of M.I.T/W.H.O.I.. He was married to Ching-ju Chen on June 18, 1976.

Publications

P.T. Shaw, D.R. Watts and H.T. Rossby, 1978: On the estimation of oceanic wind speed and stress from ambient noise measurements. Deep-Sea Res., 25, 1225-1233.

G.T. Csanady and P.T. Shaw, 1980: The evolution of a turbulent Ekman layer. J. Geophys. Res., 85, 1537-1547.